LA-UR-12-26963
Approved for public release; distribution is unlimited.

Title: Characterization of Depleted-Uranium Strength and Damage Behavior

Author(s):
Gray, George T. III
Chen, Shuh-Rong
Bronkhorst, Curt A.
Dennis-Koller, Darcie
Cerreta, Ellen K.
Cady, Carl M.
McCabe, Rodney J.
Addessio, Francis L.
Schraad, Mark W.
Thoma, Dan J.
Lopez, Mike F.
Mason, Thomas A.
Papin, Pallas A.
Trujillo, Carl P.
Korzekwa, Deniece R.
Luscher, Darby J.
Hixson, Robert S.
Maudlin, Paul J.
Kelly, A.M.

Intended for: Campaign 2 - Level 2 Milestone Report -- MRT#4520 Report

CHARACTERIZATION OF DEPLETED-URANIUM STRENGTH AND DAMAGE BEHAVIOR

Campaign 2 - Level 2 Milestone Report
MRT# 4520

Provide a summary of DU characterization, strength and damage data for ASC theory, model development and validation, collaboration with PEM, JMP and C4

December 20, 2012

Los Alamos National Laboratory
Los Alamos, New Mexico

Contributing authors: George T. Gray III, Shuh-Rong Chen, Curt A. Bronkhorst, Darcie Dennis-Koller, Ellen K. Cerreta, Carl M. Cady, Rod McCabe, A.M. Kelly(MST-6 retired), F. L. Addessio, M. W. Schraad, D.J. Luscher, Dan Thoma, M.F. Lopez, P.J. Maudlin (T-3; retired), T.A. Mason, P.A. Papin, C.P. Trujillo, Rob S. Hixson(retired, DX-9), D.R. Korzekwa

Table of Contents

Abstract

The intent of this report is to document the status of our knowledge of the mechanical and damage behavior of Depleted Uranium(DU hereafter). This report briefly summaries the motivation of the experimental and modeling research conducted at Los Alamos National Laboratory(LANL) on DU since the early 1980's and thereafter the current experimental data quantifying the strength and damage behavior of DU as a function of a number of experimental variables including processing, strain rate, temperature, stress state, and shock prestraining. The effect of shock prestraining on the structure-property response of DU is described and the effect on post-shock mechanical behavior of DU is discussed. The constitutive experimental data utilized to support the derivation of two constitutive strength (plasticity) models, the Preston-Tonks-Wallace (PTW) and Mechanical Threshold Stress (MTS) models, for both annealed and shock prestrained DU are detailed and the Taylor cylinder validation tests and finite-element-modeling (FEM) utilized to validate these strength models is discussed. The similarities and differences in the PTW and MTS model descriptions for DU are discussed for both the annealed and shock prestrained conditions. Quasi-static tensile data as a function of triaxial constraint and spallation test data are described. An appendix additionally briefly describes low-pressure equation-of-state data for DU utilized to support the spallation experiments. The constitutive behavior of DU screw/bolt material is presented. The response of DU subjected to dynamic tensile extrusion testing as a function of temperature is also described. This integrated experimental technique is planned to provide an additional validation test in the future. The damage data as a function of triaxiality, tensile and spallation data, is thereafter utilized to support derivation of the Tensile Plasticity (TEPLA) damage model and simulations for comparison to the DU spallation data are presented. Finally, a discussion of future needs in the area of needed DU strength and damage research at LANL is presented to support the development of physically-based predictive strength and damage modeling capability.

Section 1: Introduction and Historical Perspective

The mechanical properties, microstructure development, constitutive behavior, and damage and failure response of depleted-uranium (hereafter DU), as a function of processing, have been the subject of long-term research at Los Alamos National Laboratory. While it is neither readily feasible nor the intent and focus of this Level-2 milestone report to summarize the total state of knowledge of the mechanical and damage response of DU, some brief review of the important experimental variables examined within LANL prior to the specific content of this report is germane. Interested readers are encouraged to seek background materials on the state of knowledge concerning the structure, constitutive behavior, and transformations in uranium and uranium alloys in some of the seminal reviews on this topic[1-5]. The basis of the archival understanding and modeling of the constitutive behavior of DU within LANL is based in part upon the body of research conducted by Phillip E. Armstrong during the 1960-1990's time frame[6-9] and in the 1980-1990's through the additional research conducted by a number of researchers within the Laboratory. The state-variable-based constitutive MTS model for DU developed by this long-term laboratory effort was summarized in 1989[10]. Based upon specially-processed fine-grained isotropic DU rod material data of Phil Armstrong and Walter Wright[11], a constitutive description of DU, using the PTW model[12] was derived and published in 2003.

Additional testing of fine-grained DU plate from Y12, termed SPY007, continued during the early and mid-1990's, both to support programmatic needs to describe Y12 materials in detail, but also in response to the wide and poorly understood variability in mechanical behavior observed in the Y12 plate materials. Questions surrounding the influence of processing, cast versus wrought, and chemistry, specifically carbon content, dominated these studies. Figure 1 illustrates the driving motivation in understanding the variability in Y12 wrought plate material showing the extensive spectrum of response in Y12 wrought plate as a function of processing and compressive loading direction. The absolute differences in the mechanical behavior, let along the anisotropic behavior, of these three lots of wrought plate are so significant so as to make the derivation of a single constitutive model for DU impossible. This wide variability in mechanical response during the mid-1990's to 2003 drove refinement and selection of processing specifications for wrought DU plate to yield both "more" isotropic and reproducible absolute mechanical response, ie., yield strength and texture as part of the ADAPT program. During the mid to late-1990's additional interest in the effects of carbon content and the effect of processing, wrought versus cast, resulted in the inception of several studies aimed at quantifying the effects of both variables on DU mechanical behavior. Figure 2 presents a summary of the differences in the mechanical behavior of DU as a function of processing route and carbon variations of ~<20 ppm C, ~100 ppm C, and nominally 500 ppm C.

The resurgence in research effort and mechanical property characterization was also in part initiated in the later-1990's as questions were raised concerning the applicability of the Armstrong DU data, and its commensurate PTW model coefficients to the updated SPY007 plate stock being utilized at LANL to support programmatic efforts. Figure 3 illustrates the significant difference between the isotropic Armstrong and Wright[11] rod material and the SPY007 plate stock of relevance to programmatic activities. The large difference in the mechanical behavior noted led to increased microstructural and mechanical property

characterization leading to the genesis of the volume of DU property data summarized in this report.

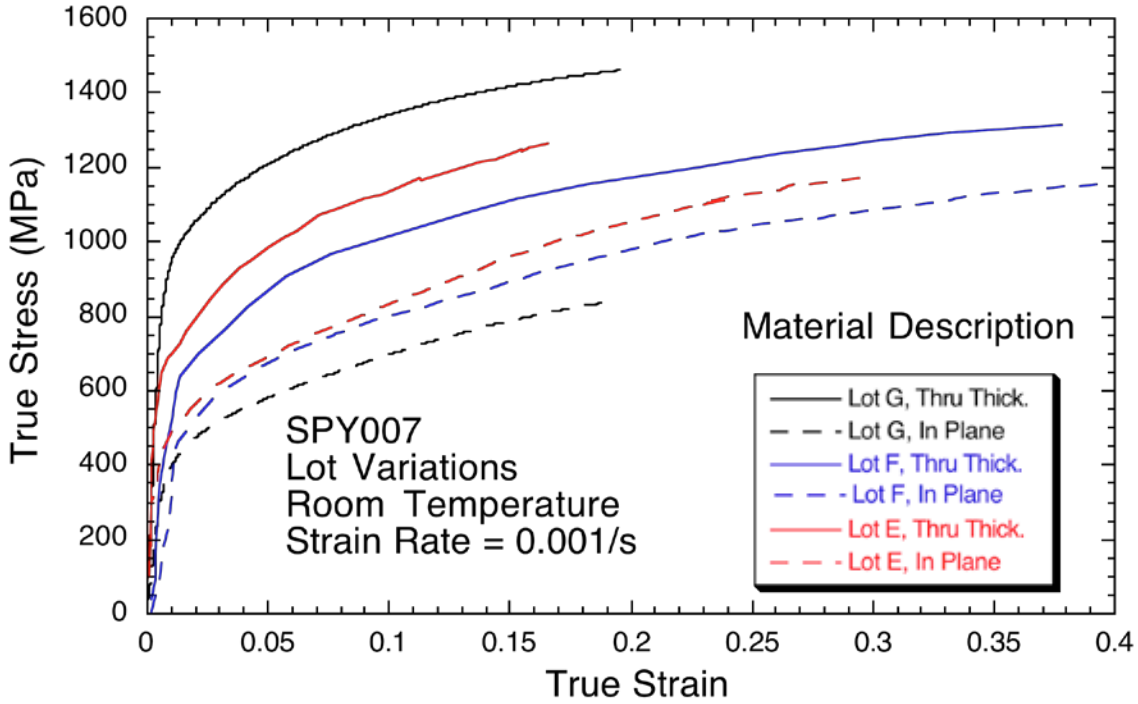

Figure 1: Compressive true-stress true-strain mechanical response of three lots of wrought DU plate showing the wide variability in mechanical behavior between the three lots and the difference in the mechanical behavior between the through thickness (TT) and in-plane (IP) loading directions in these wrought plates.

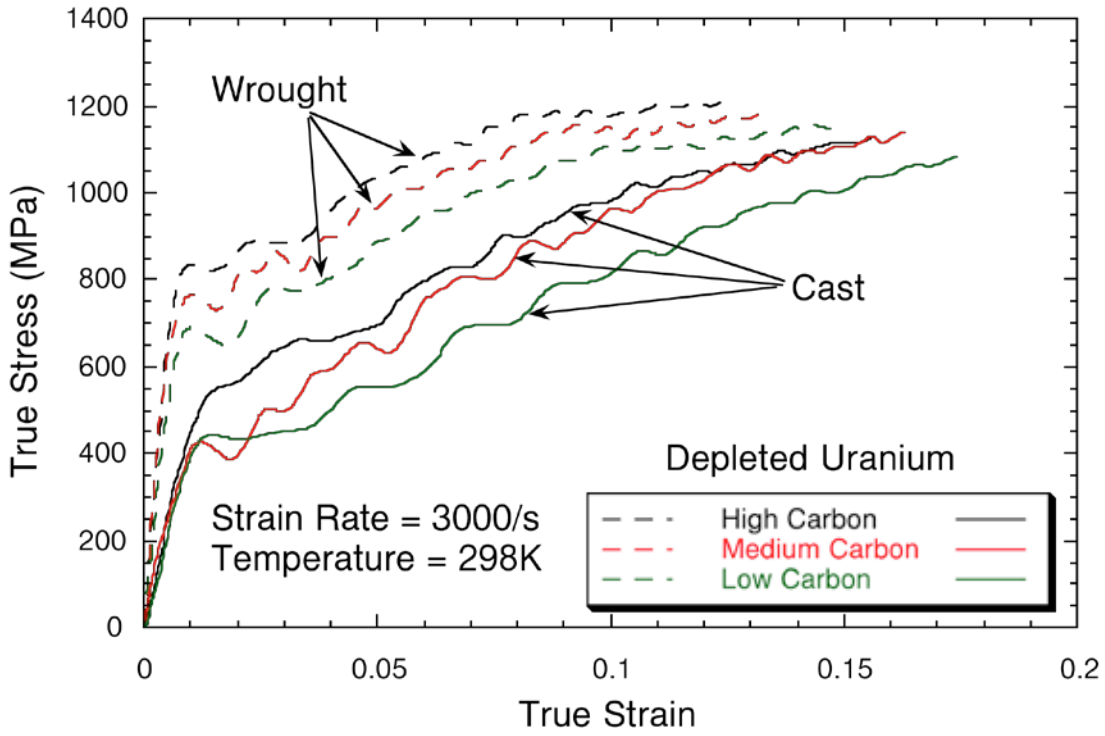

Figure 2: High-strain-rate mechanical behavior of DU as a function of carbon content for both wrought and cast material.

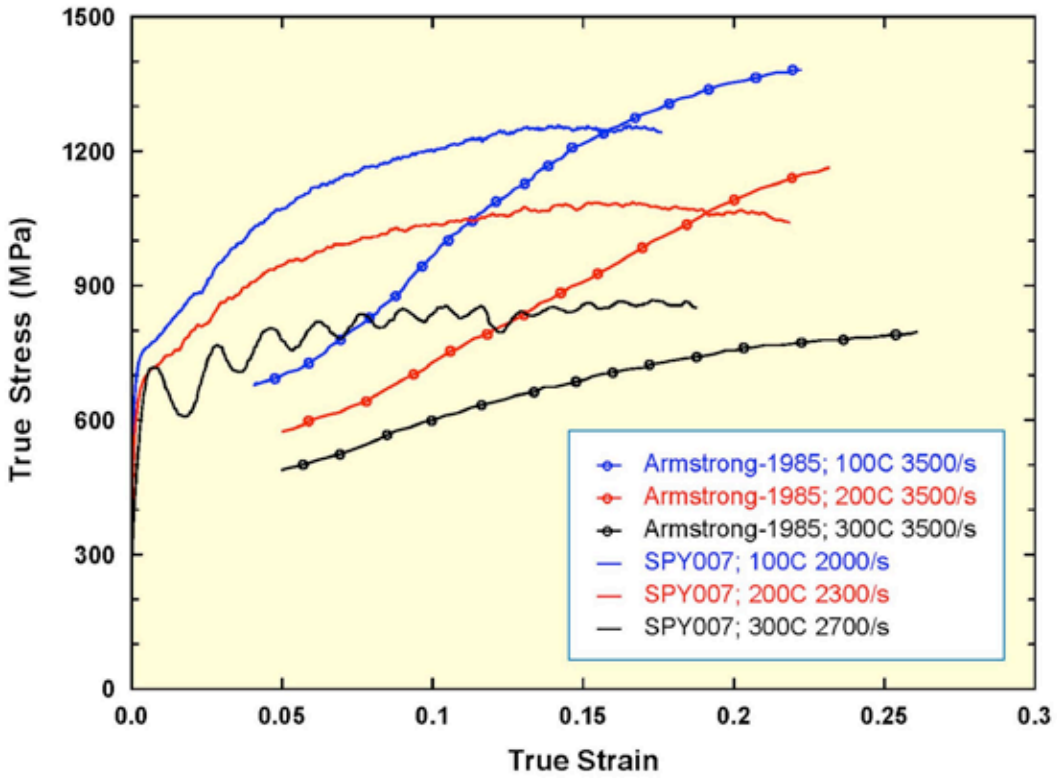

Figure 3: Comparison of DU data from Armstrong and Wright[11] – from isotropic bar stock material versus annealed rolled SPY007 plate material from Y12.

References:

1. A.N. Holden, Physical Metallurgy of Uranium, Addison-Wesley, (1958).

2. W.D. Wilkinson, Uranium Metallurgy, Volume 1, Interscience Press (1962).

3. Metallurgical Technology of Uranium and Uranium Alloys; Volume 1: Physical Metallurgy of Uranium and Uranium Alloys; American Society for Metals, Cleveland, Ohio(1982), pp. 1-343.

4. G.H. Lander, E.S. Fisher, and S.D. Bader; Advances in Physics, (1994), vol. 43, pp. 1-111. "The Solid-State Properties of Uranium; A Historical Perspective and Review"

5. K.H. Eckelmeyer, Metals Handbook, volume 2; 10th Edition: Properties and Selection; (1991) ASM International, Materials Park, OH; "Uranium and Uranium Alloys"

6. S.L. Robinson, O.D. Sherby, P.E. Armstrong; Journal of Nuclear Materials, v. 46, no. 3, pp. 293-302 (1973-04-01). "Elevated-temperature plastic flow of high-purity uranium in the alpha, beta, and gamma phases"

7. P.E. Armstrong, R.W. Ellis, P.S. Follansbee, D.C. Garcia, M.F. Lopez; Report no. LA-11746-MS, 1990-04-01. "Mechanical behavior of aged uranium-3/4 weight percent titanium alloy"

8. P.E. Armstrong, D.T. Eash, J.E. Hockett; Journal of Nuclear Materials (Dec. 1972) vol.45, no.3, p.211-16. "Elastic moduli of alpha, beta and gamma polycrystalline uranium"

9. P.E. Armstrong, "High Strain Rate Mechanical Behavior," in Metallurgical Technology of Uranium and Uranium Alloys, (ASM, Metals Park, Ohio, 1982) pp. 295-342.

10. P.E. Armstrong, P.S. Follansbee, T. Zocco; Mechanical Properties of Materials at High Rates of Strain 1989; Proceedings of Fourth International Conference (1989), pp.237-44. "A constitutive description of the deformation of alpha uranium based on the use of the mechanical threshold stress as a state variable"

11. P.E. Armstrong and W.J. Wright; (1985); LA Report, LA-CP-85-353.

12. D.L. Preston, D.L. Tonks, and D.C. Wallace; Journal of Applied Physics, (2003), vol. 93, pp. 211-220.

Section 2: Material Studied

Depleted Uranium (SPY 007):

The material used for this investigation was a depleted-uranium plate material (DU) obtained in 6.25 mm-thick plate form. The annealed DU possessed an equiaxed grain structure with an average grain size of 18 microns as seen in the electron-backscatter micrograph shown in Figure 1a. The analyzed chemical composition of this depleted uranium (wt. pct.) was: 14 ppm Al, 40 ppm C, <10 ppm Ca, <10 ppm Fe, <2 ppm Mg, 4 ppm Mn, 11 ppm Ni, <10 ppm Si, and bal. U . The initial plate texture, quantified using orientation imaging microscopy (OIM), consisted of a strong [001] component in the plate through-thickness (TT) direction (max. 3.8 times random) with moderate texture asymmetries within the plane of the plate as seen in Figure 1b.

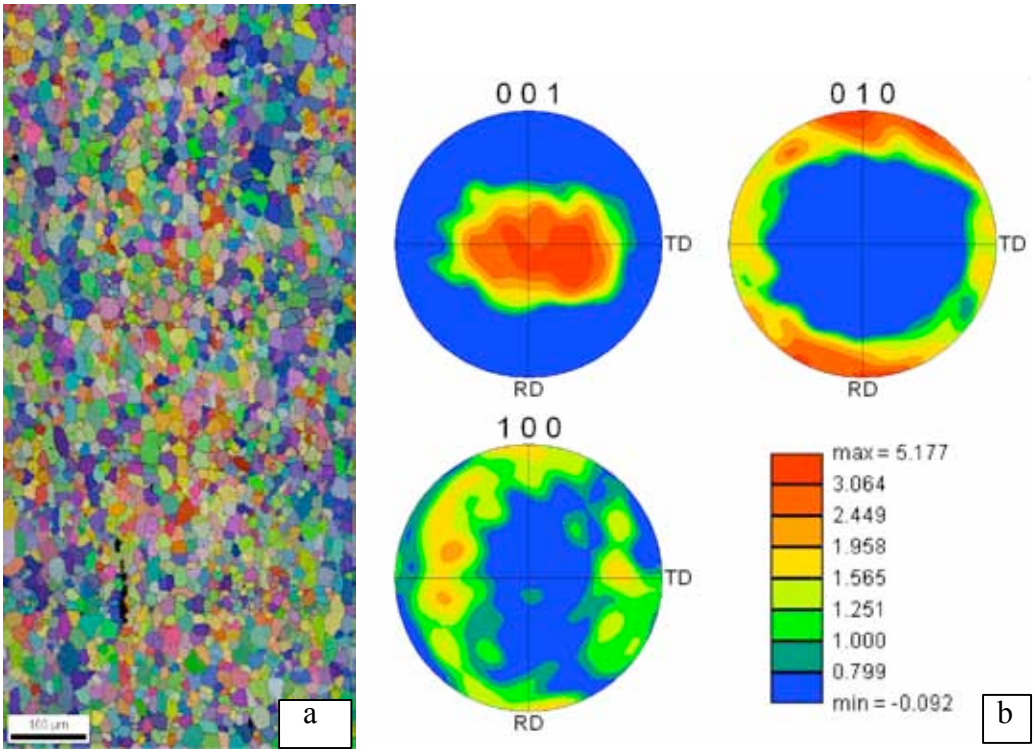

Figure 1: a) EBSD micrograph of the annealed DU material, and b) annealed texture.

Section 3: Mechanical Behavior of DU as a function of Strain Rate and Temperature

Shuh Rong Chen and G. T. (Rusty) Gray III

In the past two decades, the Dynamic Property Team in Materials Science and Technology Division has investigated the mechanical properties of various materials of interest to many DOE and DoD defense programs at Los Alamos National Laboratory. We have measured the constitutive responses of these materials to quantify the strain-rate and temperature dependencies that are relevant to various applications. We analyzed data to probe the deformation mechanisms and derived the material parameters to support several constitutive models that were developed based on physical understanding of the deformation processes. We also conducted small-scale integrated experiments to validate the applicability of these models and the accuracy of the set of parameters utilizing Taylor cylinder impact tests. The Taylor test extended the strain rate accessed by one order of magnitude, $10^5 s^{-1}$, beyond what our usually test matrix and experimental apparatus, i.e. the split-Hopkinson Pressure Bar, could provide. The Taylor test also encompasses a wide range and gradient of plastic strains and stresses during impact, up to several 100's of percent, as well as reaches higher temperature due to adiabatic heating at the high strain rates imposed.

This document represents a compilation of what we currently know in terms of the mechanical properties for depleted uranium and the corresponding parameters for the PTW and the MTS constitutive models. It represents our general understanding of the DU studied and what we believe is appropriate to represent the measured mechanical responses in the constitutive model based on the most complete set of mechanical property data and validation tests. As can be seen from the figures that follow in this report, there remain many areas where our understandings of the mechanical responses of some aspects of DU constitutive behavior are limited and as such further study is necessary. Depleted uranium exhibited significant difference in its mechanical response between the through-thickness and in-plane direction of plate material. Currently we treat them independently and provide data and parameters for each direction. Until complex defense application simulations embrace fully 3-D descriptions of the constitutive behavior of materials this appear likely to remain as such.

The other important subject we are quantifying through research is the influence of explosive shock prestraining on the mechanical properties of DU and how we should model its effects on constitutive behavior. The initial shock from HE changes the substructure of a material via defect generation and storage. We have observed enhanced shock hardening, no enhanced shock hardening, and in some cases shock softening in material strength depending on the crystal structure of the material; i.e. no blanket approach to shock prestraining is appropriate; it is material specific. It is planned that we will carefully design the experiments and investigate this issue in a systematic way as a function of a number of key materials and provide information to model the pre-shock effects in the future.

The authors would like to emphasize that the figures and tables that follow in this document only provide you with some initial inputs for your calculations. Since the PTW and the MTS models are far from perfect in capturing the complexities of the deformation response of DU for the range of possible starting microstructures, loading conditions, and the understanding of materials behavior continues to evolve, educated adjustment to the parameters are necessary and justified to address particular boundary conditions for many applications.

Mechanical properties

Depleted uranium in the form of a rolled plate was characterized in compression along the through-thickness direction and in-plane direction. Due to its less symmetric crystal structure, orthohombic, DU displays significant anisotropy as demonstraded in Fig. 1. The yield strenght and the flow stress compressed in the through-thickess direction was seen to be much stronger than that observed for the in-plane orientation. This difference persists at higher strain rate or/and at higher temperture as indicated in Fig. 2.

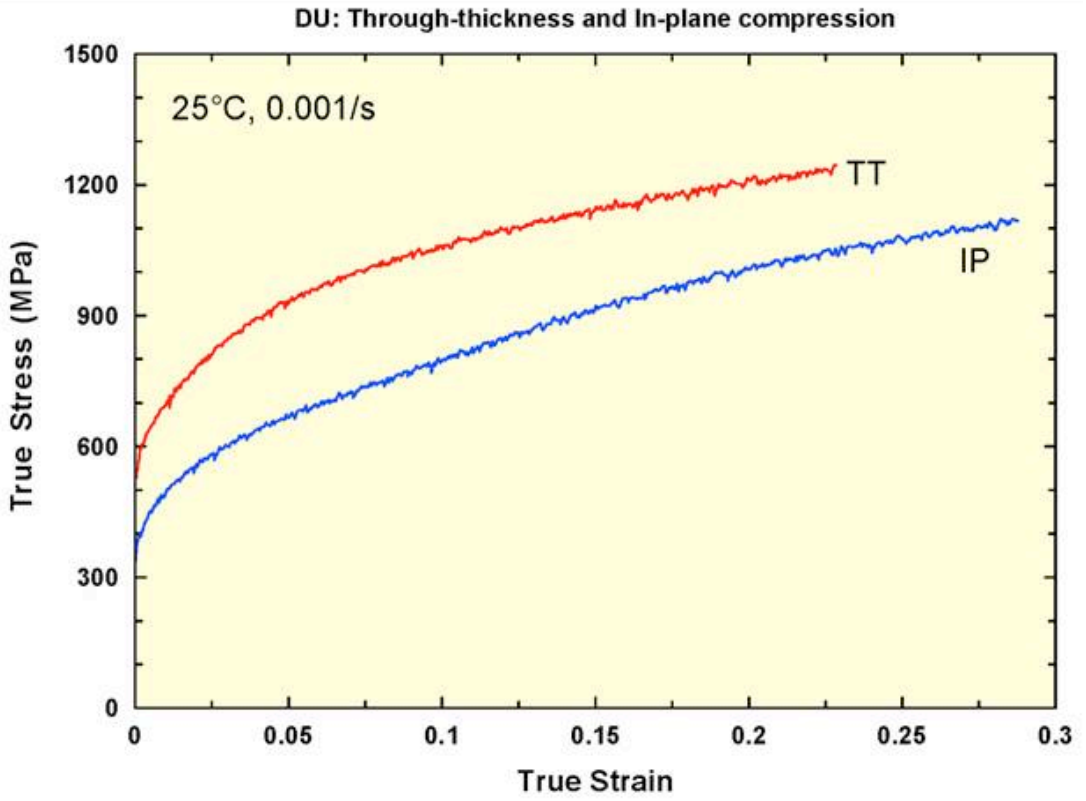

Fig. 1 Stress/strain responses of a depleted uranium plate in compression with respect to plate orientation. (TT: through-thickness and IP: in-plane direction in terms of the compression axis).

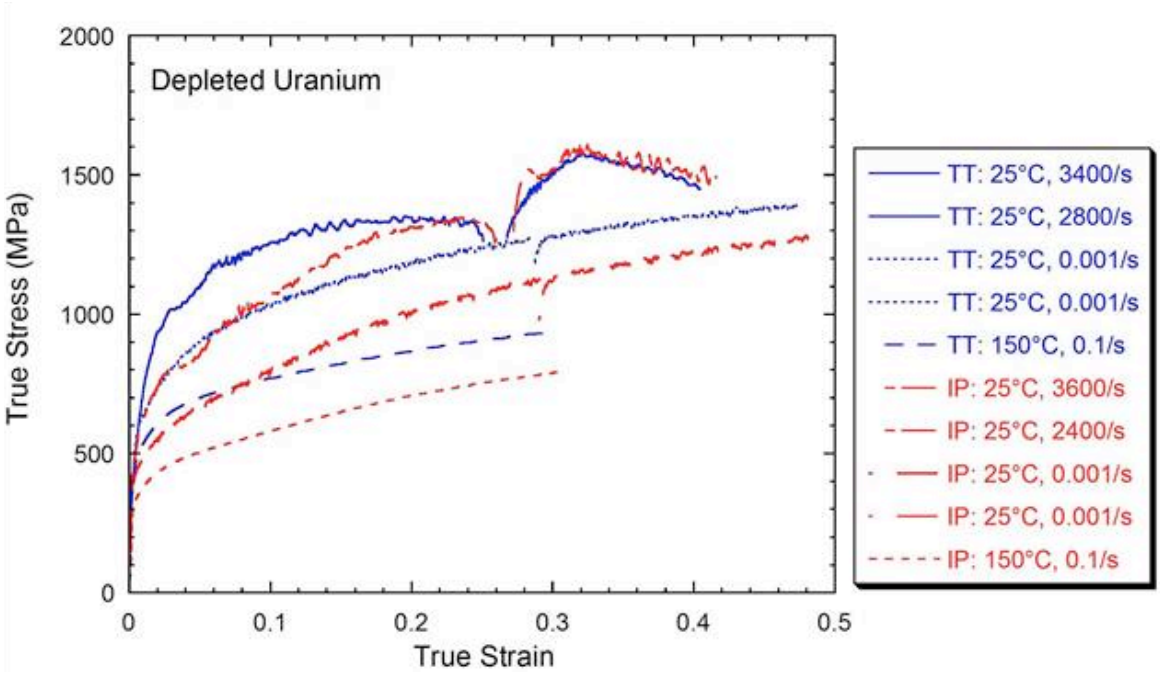

Fig. 2 Stress/strain responses as a function of strain rate and temperature of a depleted uranium plate in compression with respect to plate orientation. (TT: through-thickness and IP: in-plane direction in terms of the compression axis).

A test matrix was carefully chosen to investigate the strain-rate and temperature effects on the mechanical behavior of the annealed depleted uranium. The results are shown in Fig. 3 and Fig. 4 along through-thickness and in-plane directions, respectively. The material exhibits strong temperature and strain-rate dependence both in its yield and flow stresses. Compared to the through-thickness direction, the in-plane mechanical responses at lower temperatures yields at lower stress levels and continues to deform with a linear hardening slope that reveals deformation twinning is likely to occur based on previous experimental results of textured hafnium and zirconium. A DU sample was deformed to large strains by reloading to study the work hardening behavior in order to construct a better representation of the material response seen in some applications deformed to large plastic strains.

Uranium-depleted (through-thickness)

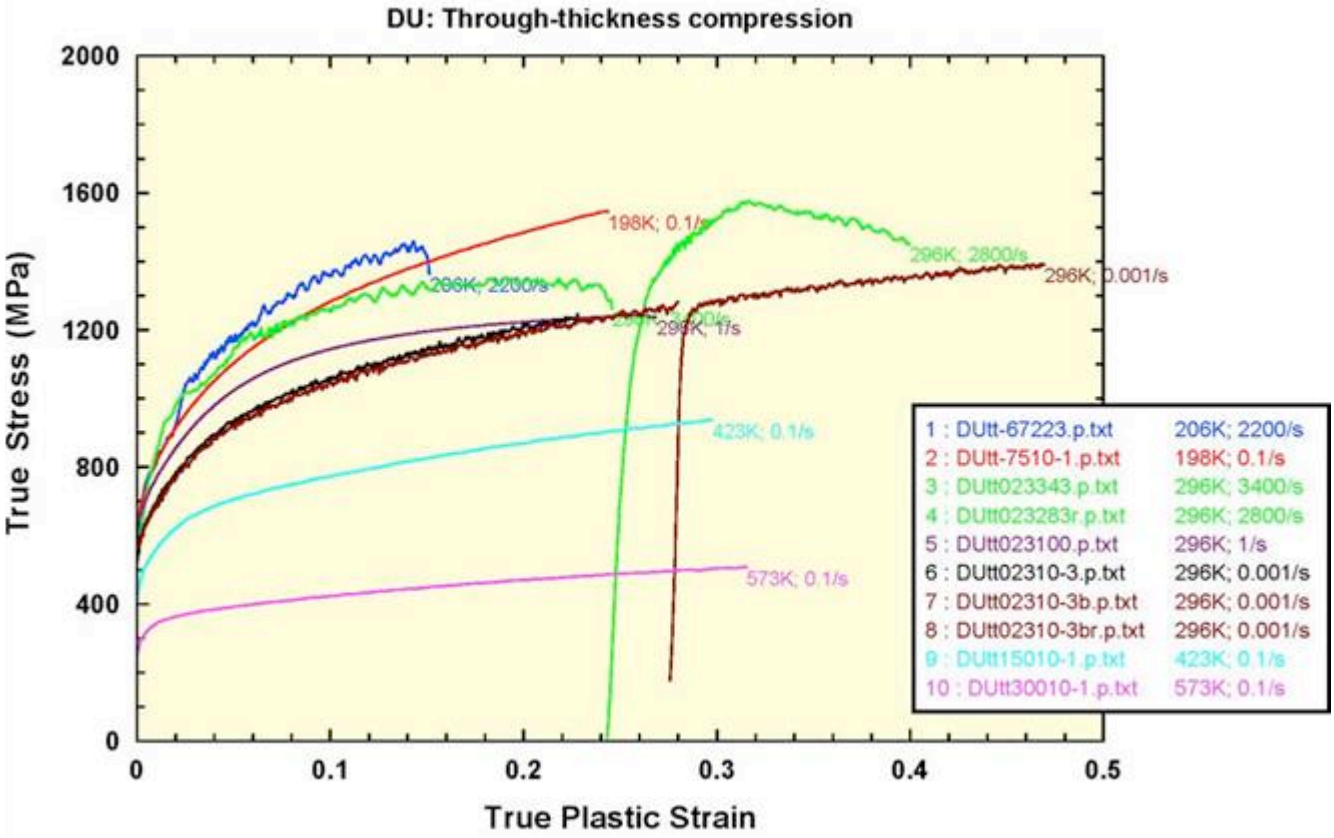

Fig. 3 Stress/strain responses as a function of strain rate and temperature of a depleted uranium plate in compression along through-thickness direction.

Uranium-depleted (in-plane)

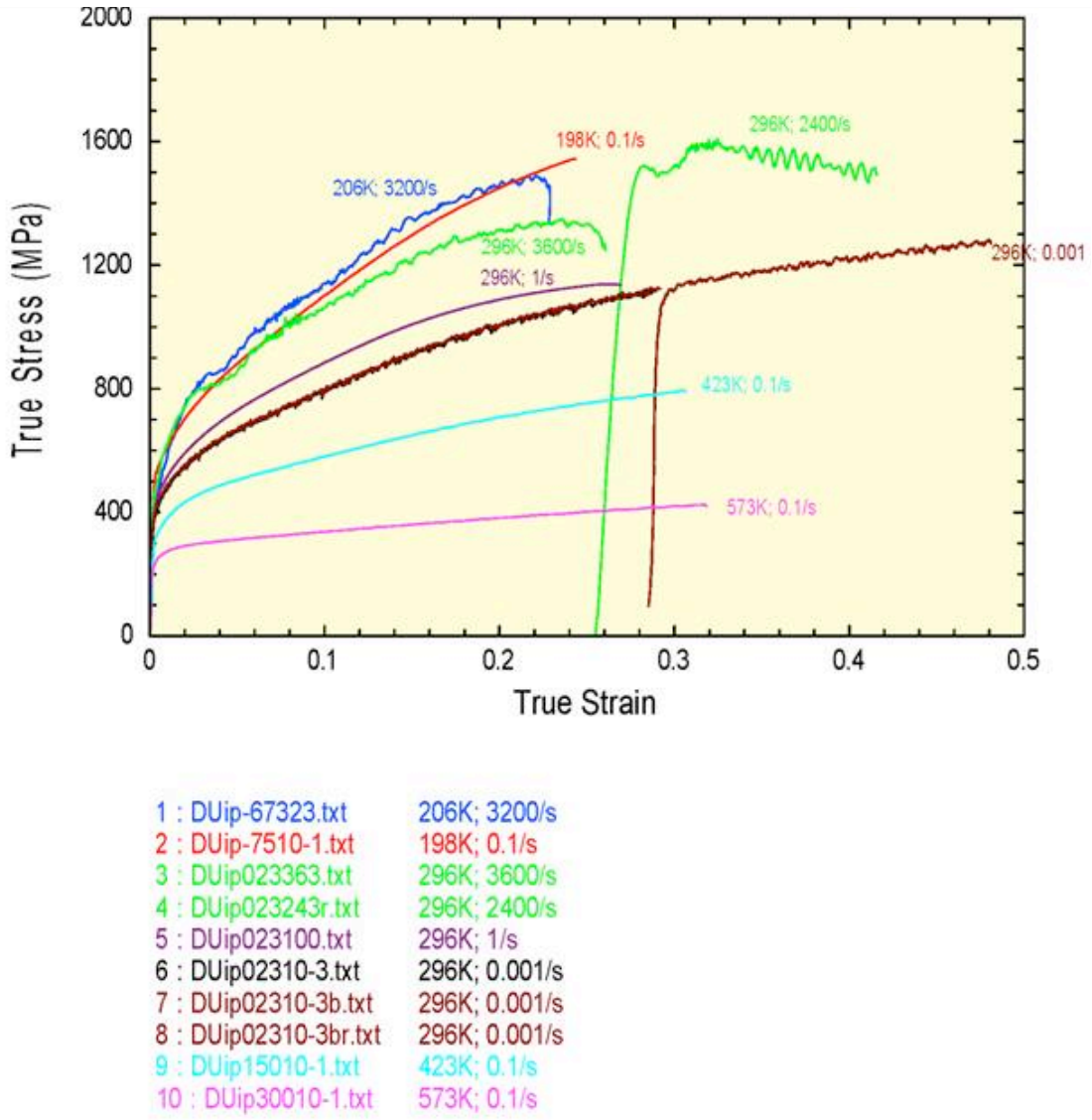

Fig. 4 Stress/strain responses as a function of strain rate and temperature of a depleted uranium plate in compression along in-plane direction.

Extensive studies on processing effects on depleted uranium plate, according to specifications, was undertaken using several possible combinations of parameters. Nine DU plates were cast, rolled, and then annealed for testing and comparison. The results are shown in Fig.5. The tenth plate shown as a red line to strains up to ~0.5 was the plate with complete data presented above. This study provides information on the variation of the mechanical properties of a given DU plate processed following a well-defined specification. However, a newer DU plate recently studied used in an integrated test clearly demonstrated that the range of variation in strength can be significantly different from what is specified to process this material (Fig. 6).

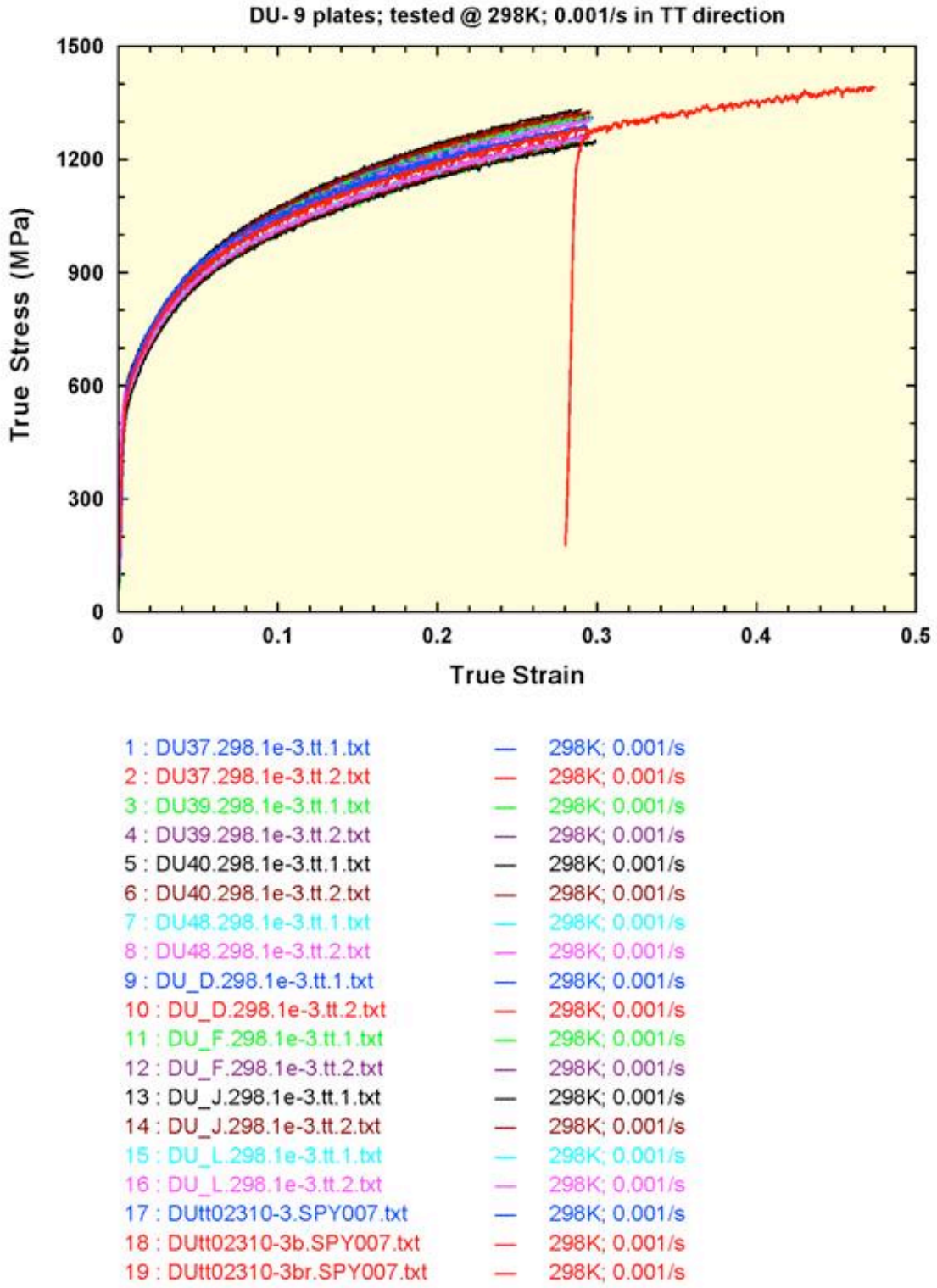

Fig. 5 Mechanical responses of ten DU plates processed within a tight range of parameters specified to meet requirement.

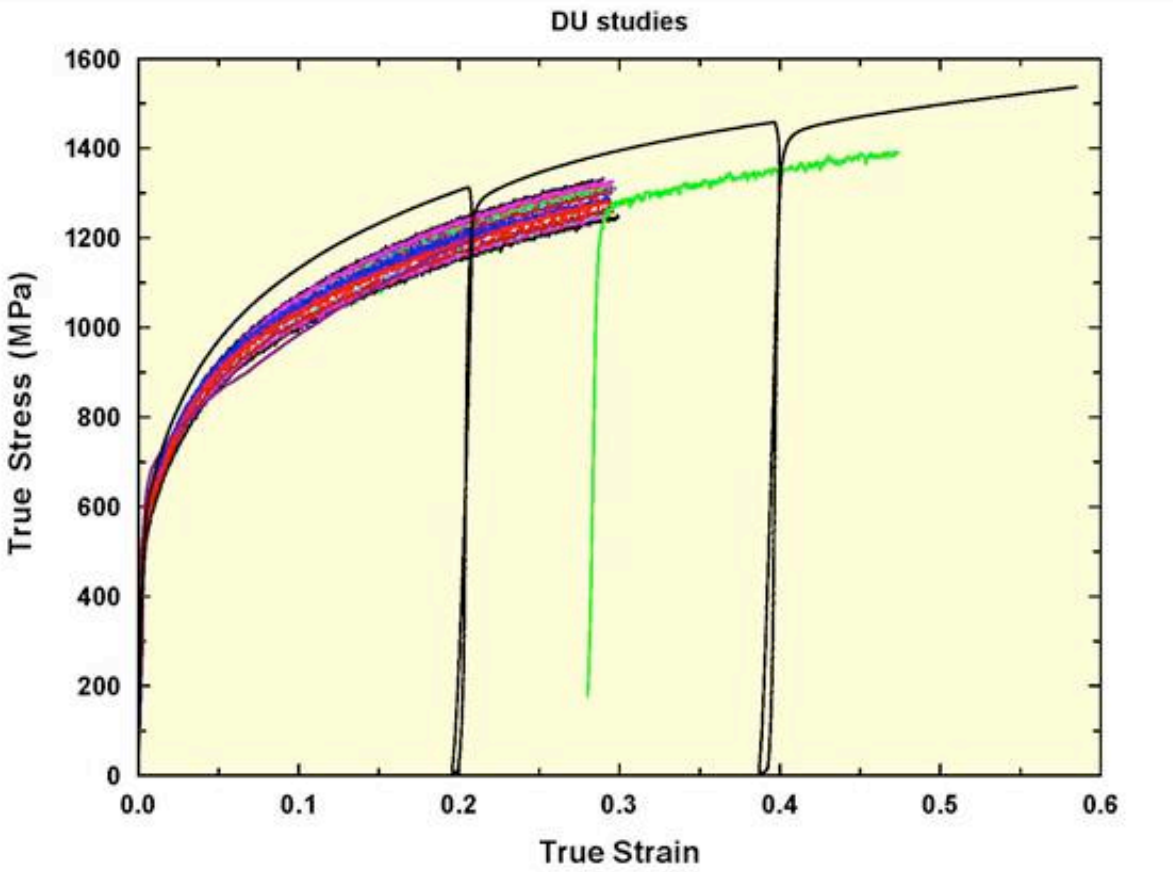

Fig. 6 Mechanical responses of a newer DU plate (top solid line) shows a stronger strength compared to ten DU plates processed within a specification.

Tensile samples were tested to obtain mechanical behavior and ductility of a DU plate. Samples were machined from the in-plane direction of the plate with a tensile axis in the 0, 45, and 90-degree orientations with respect to the plate (Fig. 7). It was clearly demonstrated that initial anisotropy plays a role in the strength of DU. For this well annealed starting material, the ductility is seen to be sufficiently high with an apparent fracture strains greater than 0.25. Samples deformed in tensile and compression along the same direction (Fig. 8) displayed little difference initially and thereafter diverged at higher strains due to the activation of different twinning systems identified in this material.

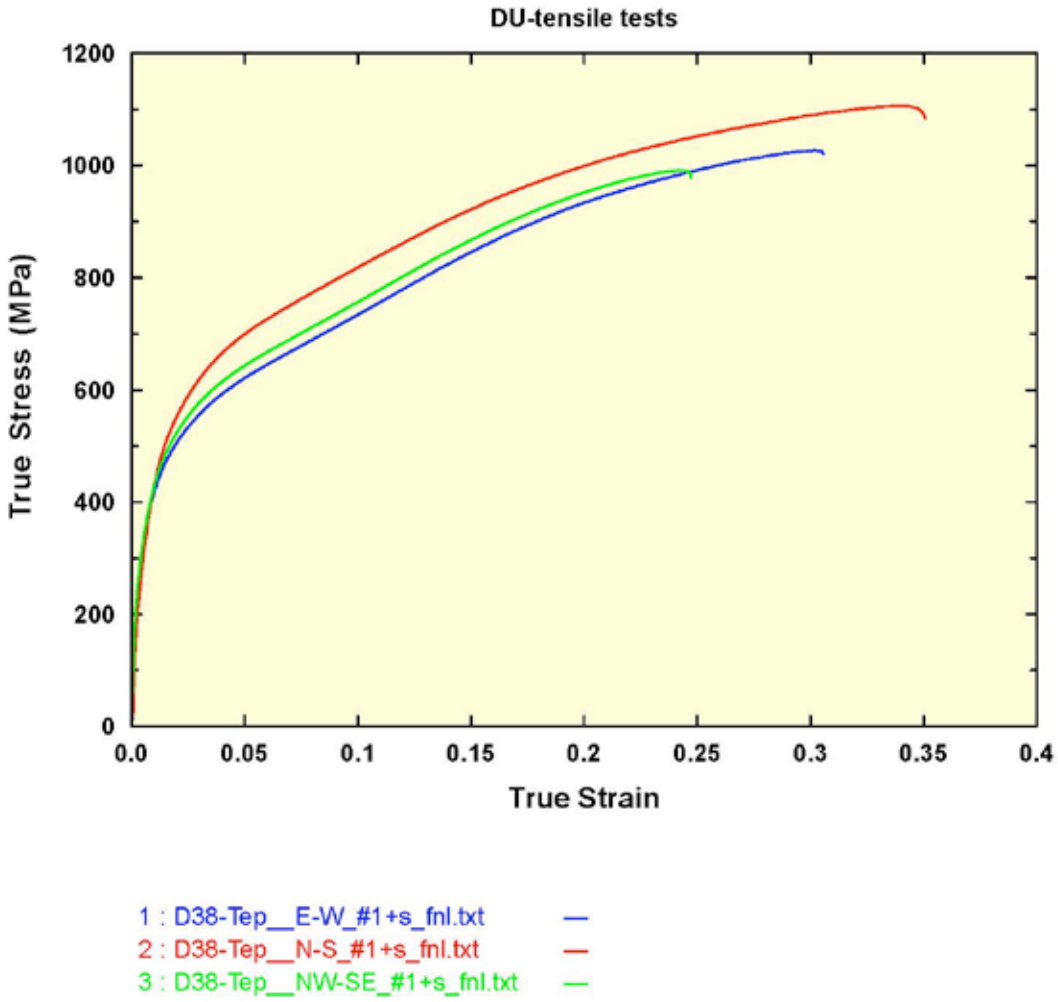

Fig. 7. Tensile property of a DU plate.

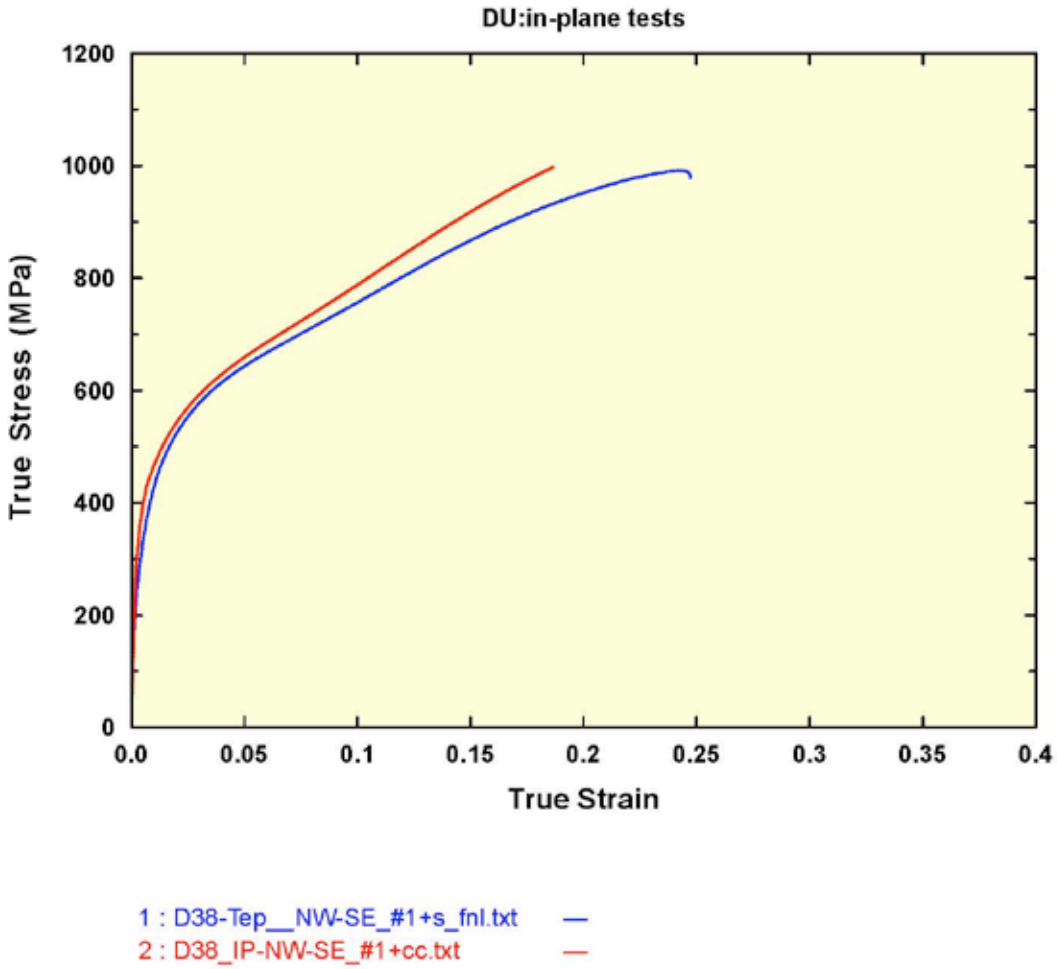

Fig. 8 Comparison of tensile and compression property of a DU plate.

HE-driven shock prestraining experiments were conducted to probe the effect of shock loading on the mechanical properties of pure depleted uranium in an annealed condition. The disk was recovered and samples were machined into regular 5mm by 5mm cylinders in the through-thickness direction for subsequent compression testing. A few strain rates and temperatures were chosen for testing to provide information for constitutive modeling.

Mechanical responses of the shock prestrained DU as a function of strain rate and temperature are shown in Fig. 9. Multiple reloadings were conducted to access the strain hardening behavior at large strains relevant in some applications. It is clearly seen in Fig. 10 that the yield stress increased from 550 MPa in the annealed condition to 850 MPa after shock prestraining to 45 GPa and then upon reloading at room temperature quasi-statically.

Even though the reloading yield stress increased after shock, it was not clear whether the level would be higher than the flow stress of a continuously deformed sample which would indicate enhanced shock hardening after compensating for the amount of plastic strain

received as a result of HE shock loading cycle. Also of interest was whether the stress level would follow the continuously deformed value that is an indication of no enhanced shock hardening. Further, it is also possible that the stress level may be lower indicating that a Bauschinger effect might be observed. The first exercise was to merely shift the stress/strain curves until the hardening behavior at higher strains from the shocked samples matched the ones from unshocked DU under the same testing conditions, respectively. This result is shown in Fig. 11 with the annealed data shown in solid lines, the shocked and reloaded data in solid symbols. The amount of strain needed to achieve a good match was found to be 0.105 and 0.13 for room temperature reloading and for reloading at 253K, respectively. A slightly higher value for 253K indicates path-dependent behavior since the shock was carried out starting at room temperature and it is accordingly the continuous mechanical response to which the comparison was made in this procedure. In both conditions, it is seen that there is a good match at around 28% plastic strain. This early analysis was done ***before*** estimation of the amount of strain imparted by the shock was calculated based on the equation-of-state (EOS) pressure-volume relation.

Following this initial assessment using small shift in the plastic strain, the reloaded yield stress was seen to be clearly lower than the flow stress at the same strain for the unshocked material (indicated by arrows in Fig. 12). From metallography it is seen that in shocked DU the microstructure displays extensive deformation twinning activation. From previous shock loading investigations on other materials, this observation leads to the possibility of shock softening as a result of a Bauschinger effect contribution.

A quick analysis based on the uranium EOS following the same procedure previously adopted for many other metals, the amount of plastic strains received as a result of the shock loading to 45 GPa was estimated to be 0.28 (coincident with the value showing good match in Fig. 13). Using this shift in plastic strain, Fig. 13 indicates significant softening and also lower flow stresses as deformation continues to a strain of 1 and beyond. Generally speaking, materials are path dependent, and the structure tends to evolve according to the new deformation path. Given a reasonable amount of deformation along the new deformation path (on the order of 10-20% straining), the structure tends to reach the similar arrangement to that of the one developed if deformation had rather followed the new path from the beginning of deformation. With this understanding, it is more plausible that the “effective” plastic strains due to the HE-driven shock loading for DU may be lower than the EOS suggests such that the analysis shown in Fig. 12 may be more appropriate based on what is available to date. One important factor may be that adiabatic heating in the DU is known to be significant at high strain rates due to its high flow stress and low thermal conductivity. This may accordingly play a role in the efficiency of forming and preserving the defect structure evolved during very high-rate shock loading and rarefaction release cycle prior to the “soft” shock recovery via firing the sample assembly into water for both deceleration and quenching the residual shock heat.

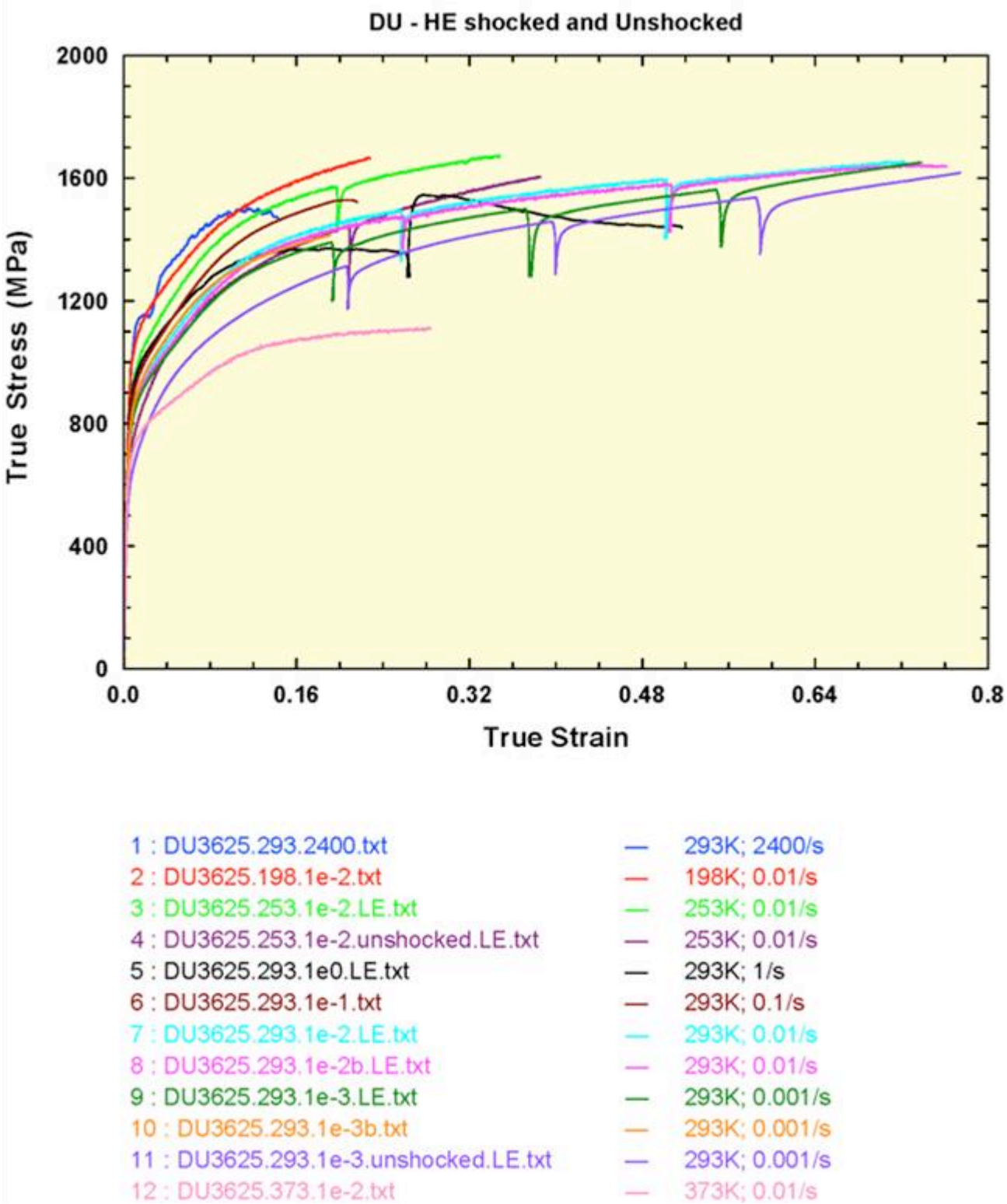

Fig. 9 Stress/strain responses of annealed DU and shocked DU without compensating plastic strains from shock.

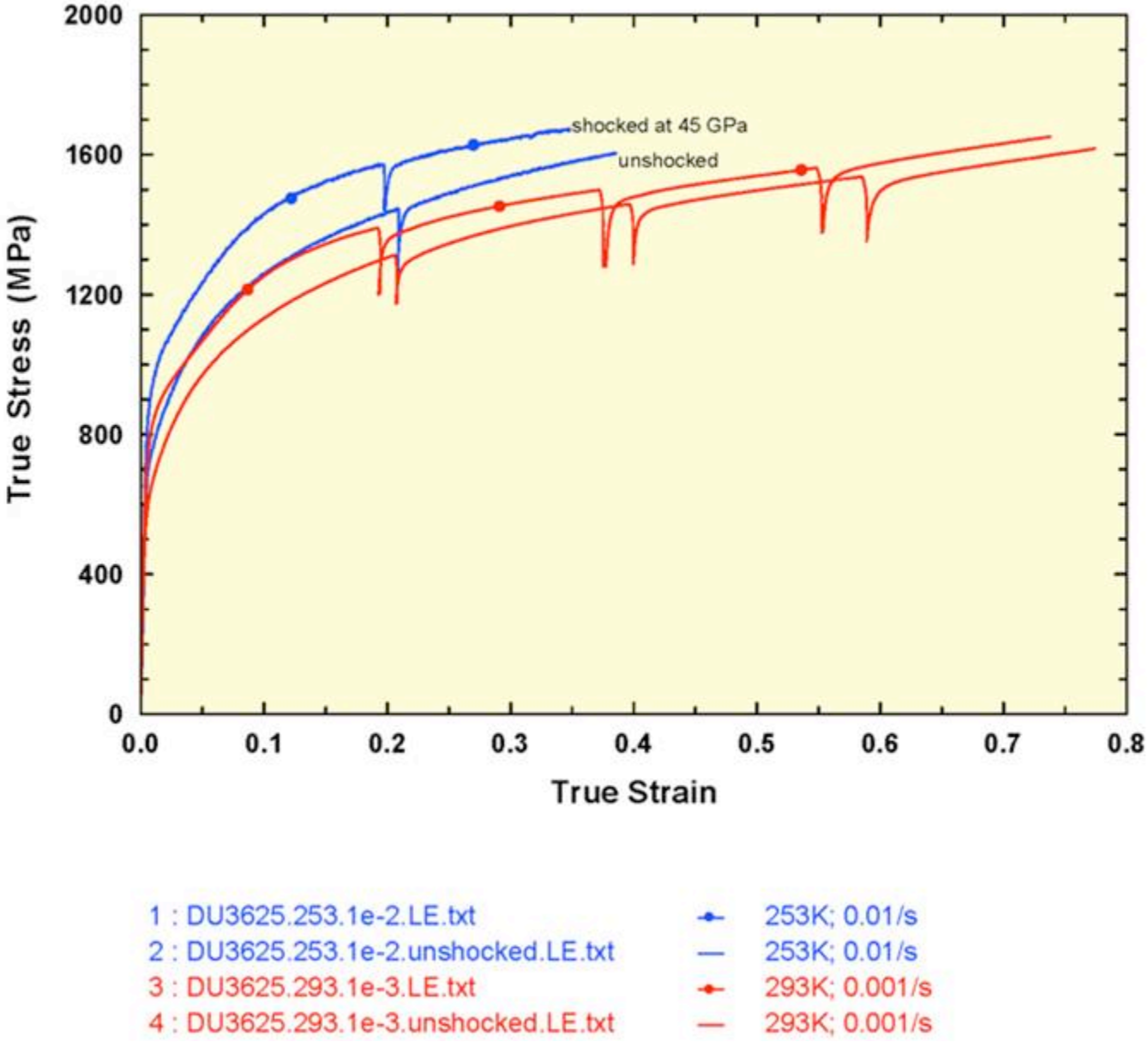

Fig. 10 Stress/strain responses of annealed DU and shocked DU (line with solid circles) without compensating plastic strains from shock.

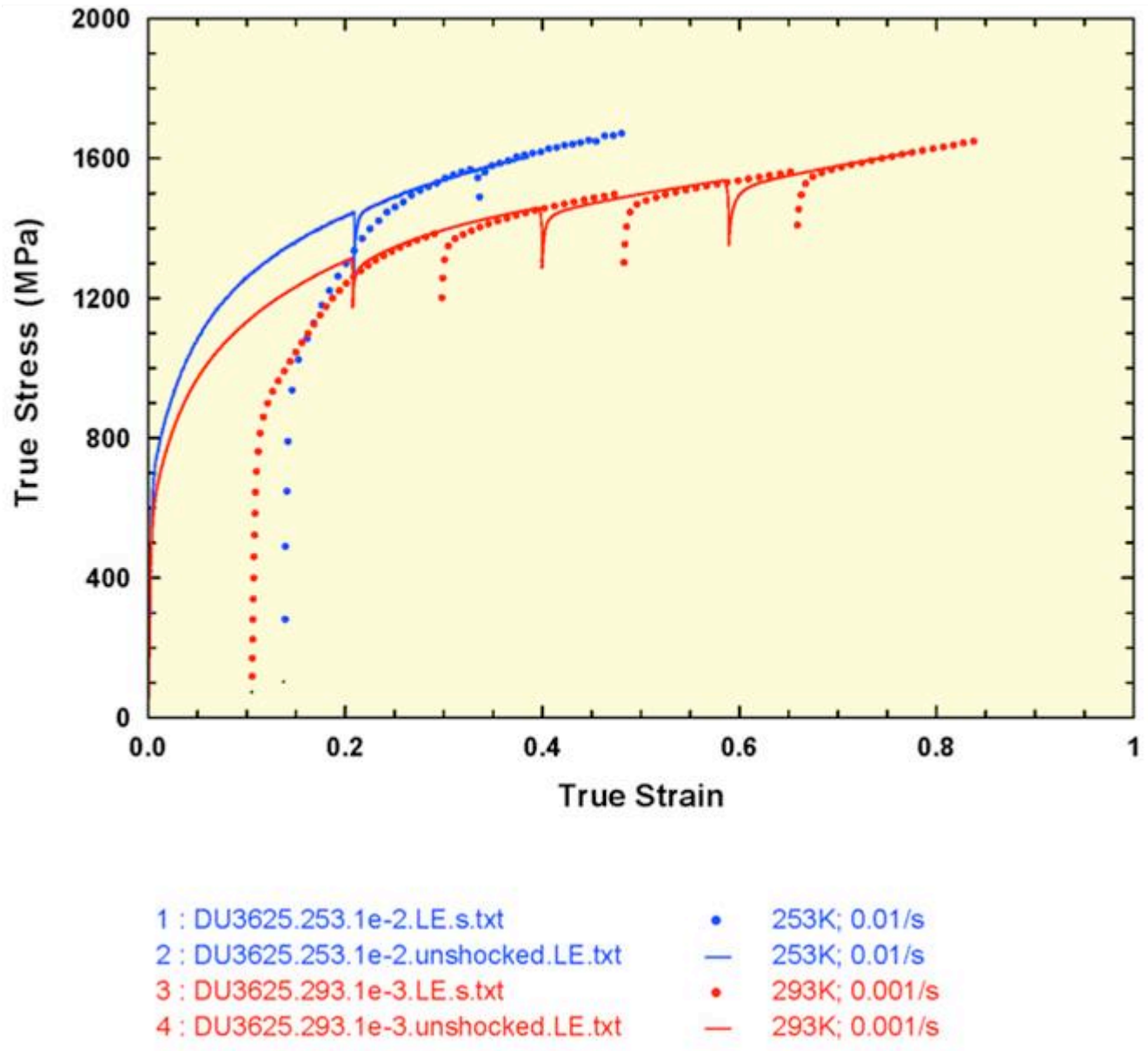

Fig. 11 Stress/strain responses of annealed DU and shocked DU (solid circles) after adding plastic strains until the work hardening matched at higher strains.

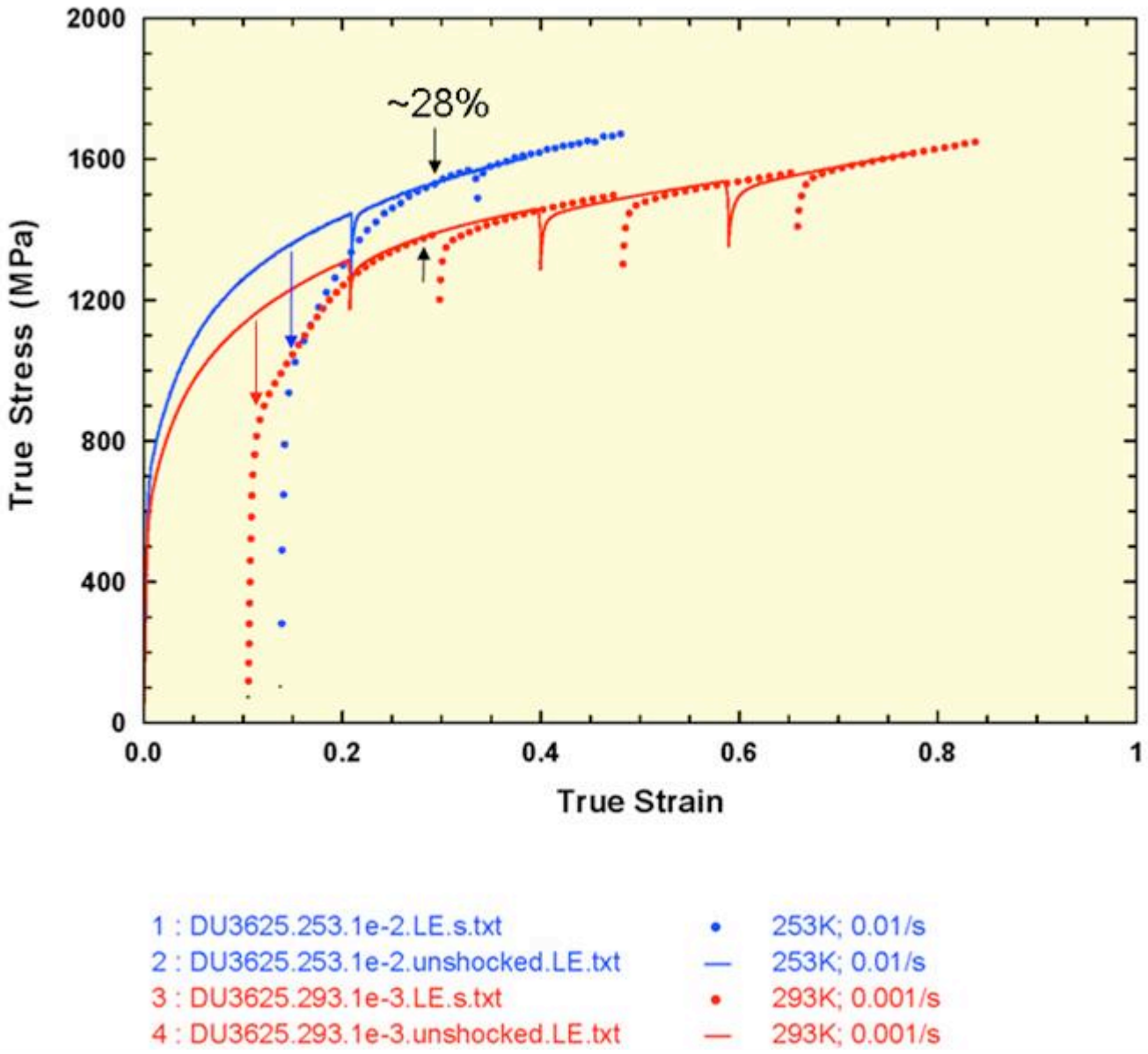

Fig. 12 Stress/strain responses of annealed DU and shocked DU (solid circles) after adding plastic strains until the work hardening matched at higher strains.

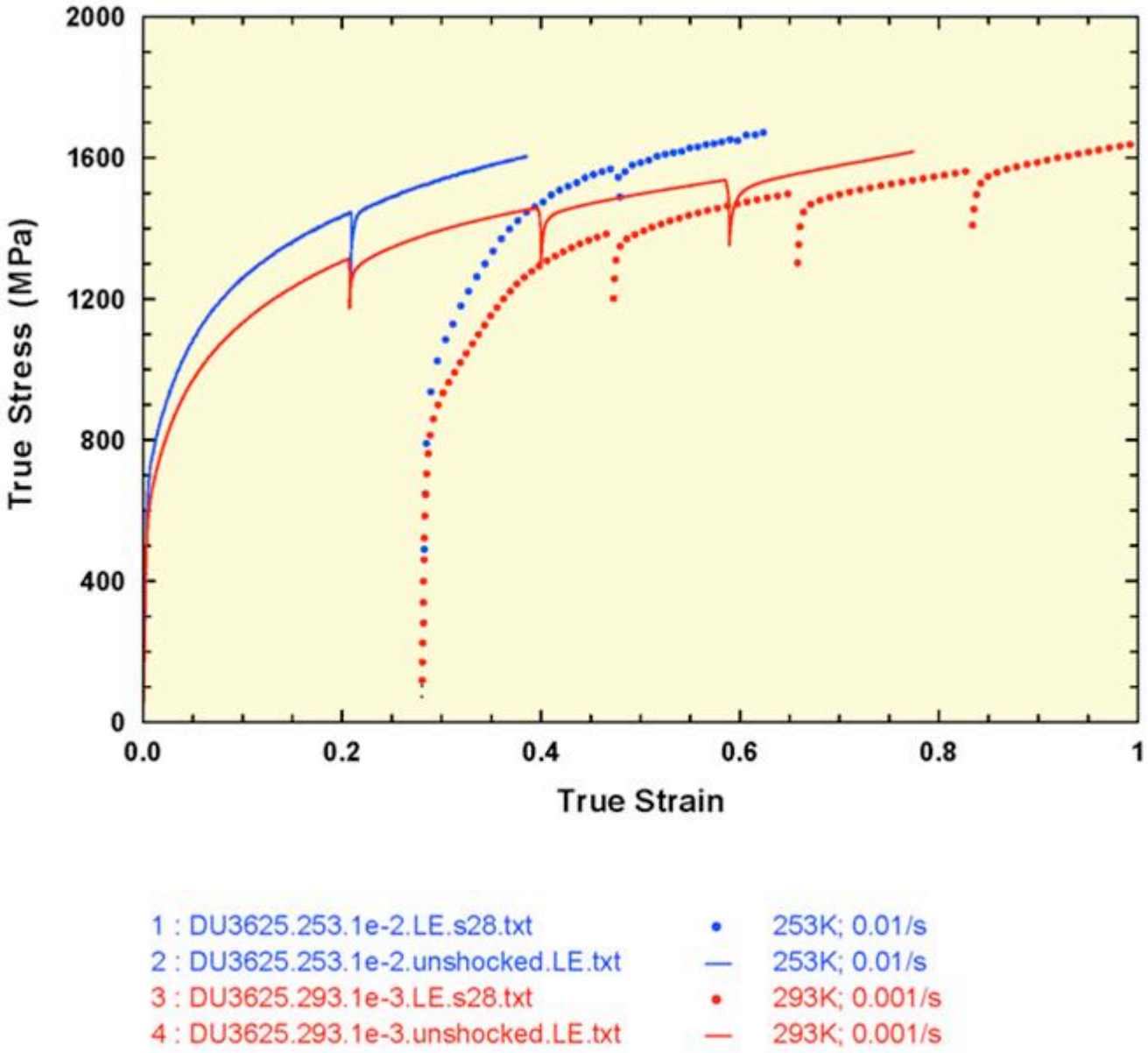

Fig. 13 Stress/strain responses of annealed DU and shocked DU (solid circles) after adding plastic strains in the amount calculated from EOS.

Section 4: Tensile Response and Damage / Failure Response of DU

E.K. Cerreta (MST-8), G.T. Gray III (MST-8), M.F. Lopez (MST-8), P.J. Maudlin (T-3, retired), and T.A. Mason (WX-DO)

Abstract: The quasi-static, mechanical behavior and fracture response of DU-38 was studied in tension through the use of smooth and notched bar specimens. The tests revealed the anisotropic nature of the plastic response prior to failure and a transition from a transgranular to an intergranular failure process with localization of stress. Additionally, comparison of the tensile behavior of DU that had been shock prestrained by direct high explosive (HE) drive with that in the as-annealed condition revealed enhanced yield stresses of the HE shock pre-strained materials.

Introduction:

There are a number of environments for which it is desirable to understand and predict the failure of a metal such as depleted uranium [1-3]. While many of these environments include dynamic, integrated loading conditions, it can be useful to set model parameters for a material damage model like TePla through the use of well controlled, lower rate uni-axial stress experiments [4]. Then, in a step-wise fashion, the validity and applicability of such parameters in more complicated loading scenarios can be tested.

It was with this research plan in mind, that the quasi-static, room temperature, tensile response of as-annealed and shock loaded DU was examined through both mechanical testing and post mortem metallography. The study revealed the role of stress state triaxiality on the nature of tensile failure, the role of stored work on yield and work hardening, and the role of texture on the mechanical response in high purity DU.

Experimental:

The high purity DU described in section 2 of this report was utilized for this study. In the as-annealed condition, three types of tensile specimens were sectioned in three different directions. The three types of specimens, shown schematically in Figures 1a and 1b, were smooth bar, A-notch, and D-notch tensile specimens used for the annealed and shock-prestrained DU testing, respectively. A description of how these geometries are utilized to examine the role of changing stress state triaxiality on failure is given elsewhere [5]. These specimens were then cut such that their loading axis was aligned with the north –south (N-S), east-west (E-W), and northwest-southeast (NW-SE) directions of the rolled and annealed plate to test the role of texture on tensile failure.

In addition, as-annealed DU material was reserved for shock loading under direct HE drive conditions. This material was loaded to a peak shock stress of ~450Kbar and soft recovered. Tensile specimens in the smooth and D-notch geometries were sectioned from the soft recovered plate.

All tensile specimens were tested at room temperature, in air, at a strain rate of 10^{-3}/s until failure. Both axial and diametral strain data were collected for all tests. Scanning electron microscopy (SEM) was performed on all fracture surfaces in secondary electron mode to examine anisotropy of failure and failure mode.

Results:

As-Annealed Tests:

The quasi-static, room temperature, tensile response of the DU-38 in the as-annealed state is shown in Figs. 2-8. In these figures, which show smooth, A-notch, and D-notch specimen type data from specimens sectioned with the loading axes aligned with the N-S, E-W, and the NW-SE texture directions of the rolled plate, axial strain data is given. The complimentary, diametral data is provided in Appendix 1. Figures 2-5 consistently display the highest yield stresses in the N-S direction but relatively similar rates of work hardening as a function of texture for smooth bar and A-notch specimens. D-notch specimens display similar rates of work hardening and similar yield stresses as a function of texture. Smooth bar specimens show the lowest strains to failure in the NW-SE direction as compared to the other loading directions. A-notch and D-notch specimens appear to have a great deal of scatter in the strain to failure data.

SEM of the fracture surfaces shows that all specimens failed in a ductile manner. Additionally, all specimens displayed similar modes of fracture as a function of texture, but a transition in fracture mode from intragranular to transgranular as a function of stress state triaxiality. Specifically, smooth bar specimens fractured transgranularly while A-notch and D-notch specimens fractured intergranularly. All specimens fractured along a plane perpendicular to the tensile axis. Finally, the anisotropy of the cross section of the fracture surface changed as a function of specimen type and therefore stress state triaxiality. Smooth bar specimens had the most anisotropic cross sections and the D-notch specimens had the least. This indicates that the competing roles of texture and stress state are critical to the plasticity leading to failure. Representative fracture surfaces, as imaged in secondary electron mode, for all specimens are given in Figs. 9-11.

Shock Prestrained DU Tests:

Depleted uranium that had been shock loaded to 450Kbar and soft recovered was sectioned into smooth bar and D-notch specimens. Texture (E-W, N-S, etc. directions) with respect to the original plate of material was not tracked. Smooth bar data is given in Fig. 12. These data show little scatter between specimens and a work hardening response that is quite similar to that displayed in the as-annealed material. However, the yield stress in these specimens is significantly enhanced over that of the as-annealed specimens, 650MPa as compared 450MPa. This indicates that while shock loading to 450Kbar stores a significant amount of work within the DU material, leading to the enhanced yield, it does not exhaust dislocation multiplication and glide mechanisms responsible for work hardening.

SEM of the fracture surfaces of these specimens revealed that all specimens failed in a ductile manner and that the fracture was transgranular in nature for the smooth bar specimens and intergranular in nature for the D-notch specimens. Additionally, the anisotropy of the cross sections of the smooth bar specimens was more significant than the D-notch specimens. SEM, Figs. 14 and 15, highlights the difference in failure response as a function of stress state triaxiality for the shock loaded DU.

Conclusions:

The quasi-static, room temperature failure response of DU has been investigated in the as-annealed and shock prestrained conditions as a function of texture and stress-state triaxiality. This study revealed that the tensile response is sensitive to texture, stress state triaxiality, and shock prestraining. The inter-granular, ductile fracture behavior of DU is sensitive to stress state triaxiality.

References:

1.) Bouchard, P.O., Gachet, J.M. Roux, E., "Ductile Damage Parameter Identification for Cold Metal Forming Applications", AIP Conference Proceedings (2011) vol. 1353, p. 47-52.
2.) Kucharshi, TR. "Modeling Ductile Damage of Steel in Aggressive Environments", TASK Quarterly (2006) vol. 10, p. 417-425.
3.) Ural, A., Krishnan, V.R., Papoulia, K.D., "A Cohesive Zone Model for Fatigue Crack Growth Allowing Crack Retardation", International Journal of Solids and Structures (2009) vol. 46, p. 2453-62.
4.) Bronkhorst, C.A., Cerreta, E.K., Xue, Q. Maudlin, P.J., Mason, T.A., Gray, G.T., "An Experimental and numerical Study of the Localization Behavior of Ta and Stainless Steel", International Journal of Plasticity (2006) vol. 22, p. 1304-1335.
5.) Harstad, E.N., Maudlin, P.J., and McKirgan, J.B., "Anisotropic Failure Modeling for HY-100 Steel", AIP Conference Proceedings –SCCM 2003, Eds. M.D. Furnish, Y.M. Gupta, and J.W. Forbes, (2004) no. 706, p. 569-572.

Figures:

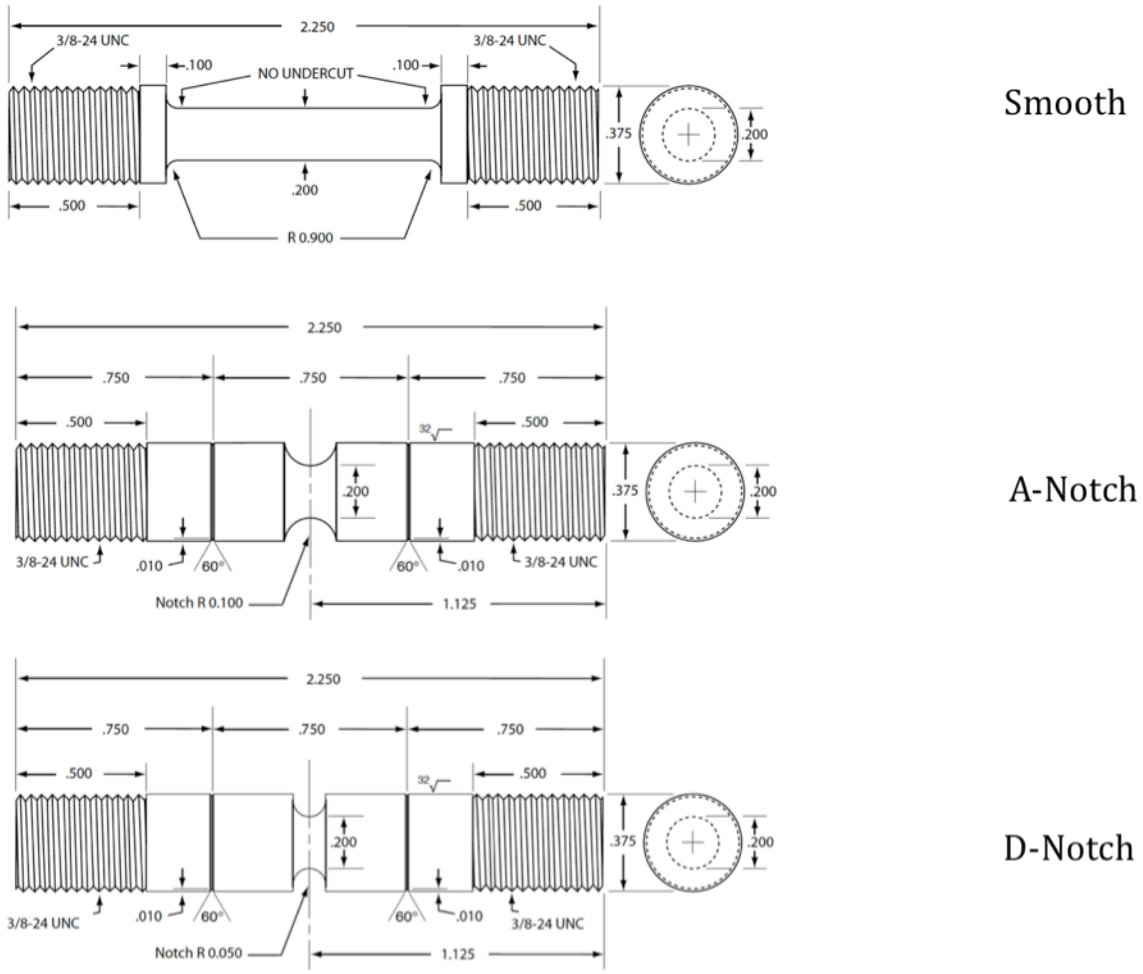

Figure 1a: Schematic of the smooth, A-notch, and D-notch tensile specimen geometries used for annealed DU tensile testing.

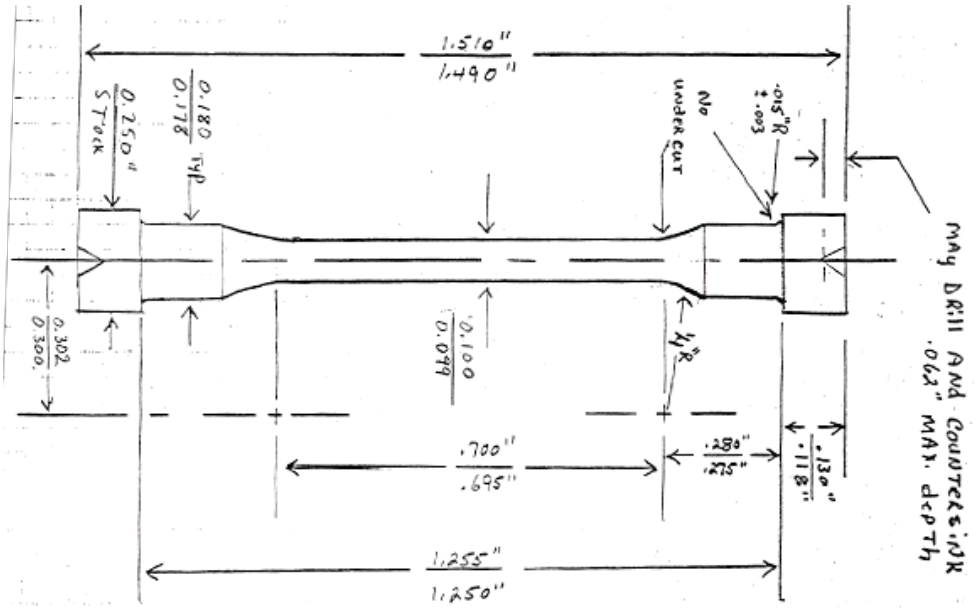

a) smooth-bar preshocked tensile sample drawing

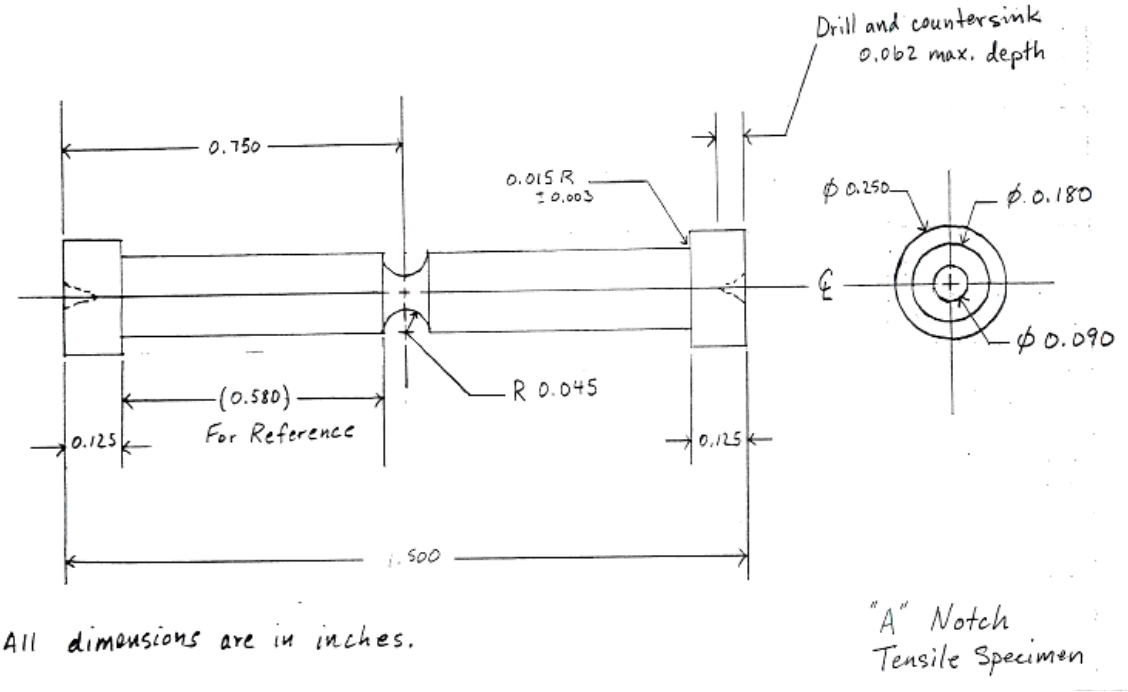

b) “A” notched-bar preshocked tensile sample drawing

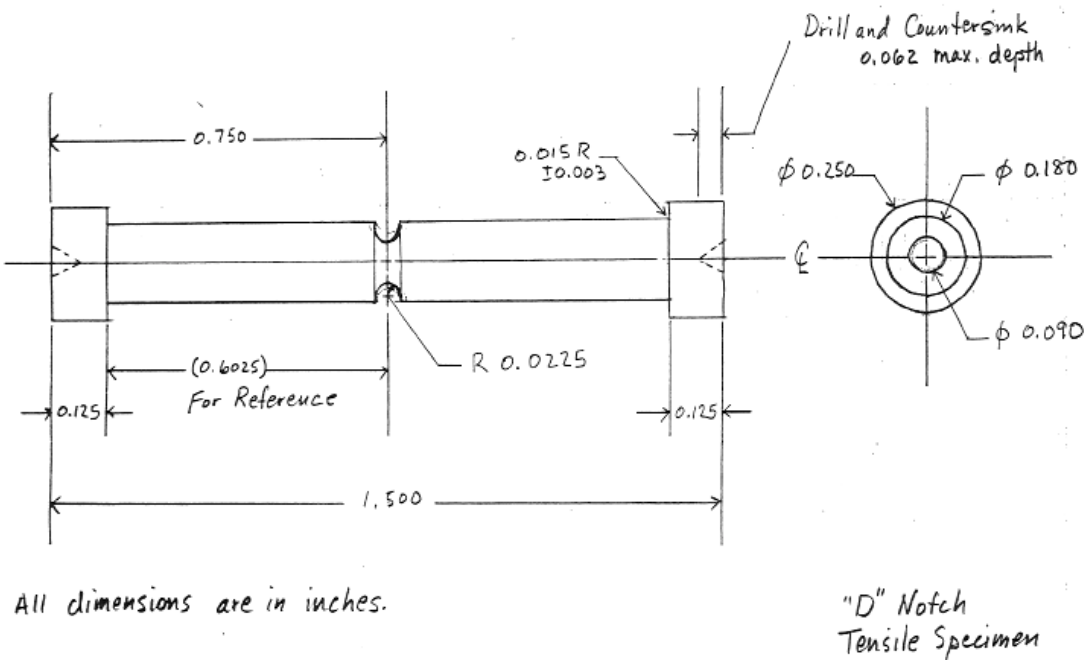

c) “D” notched-bar preshocked tensile sample drawing

Figure 1b: Schematic of the small-scale a) smooth, b) A-notch, and c) D-notch tensile specimen geometries machined from shock prestrained DU for tensile testing.

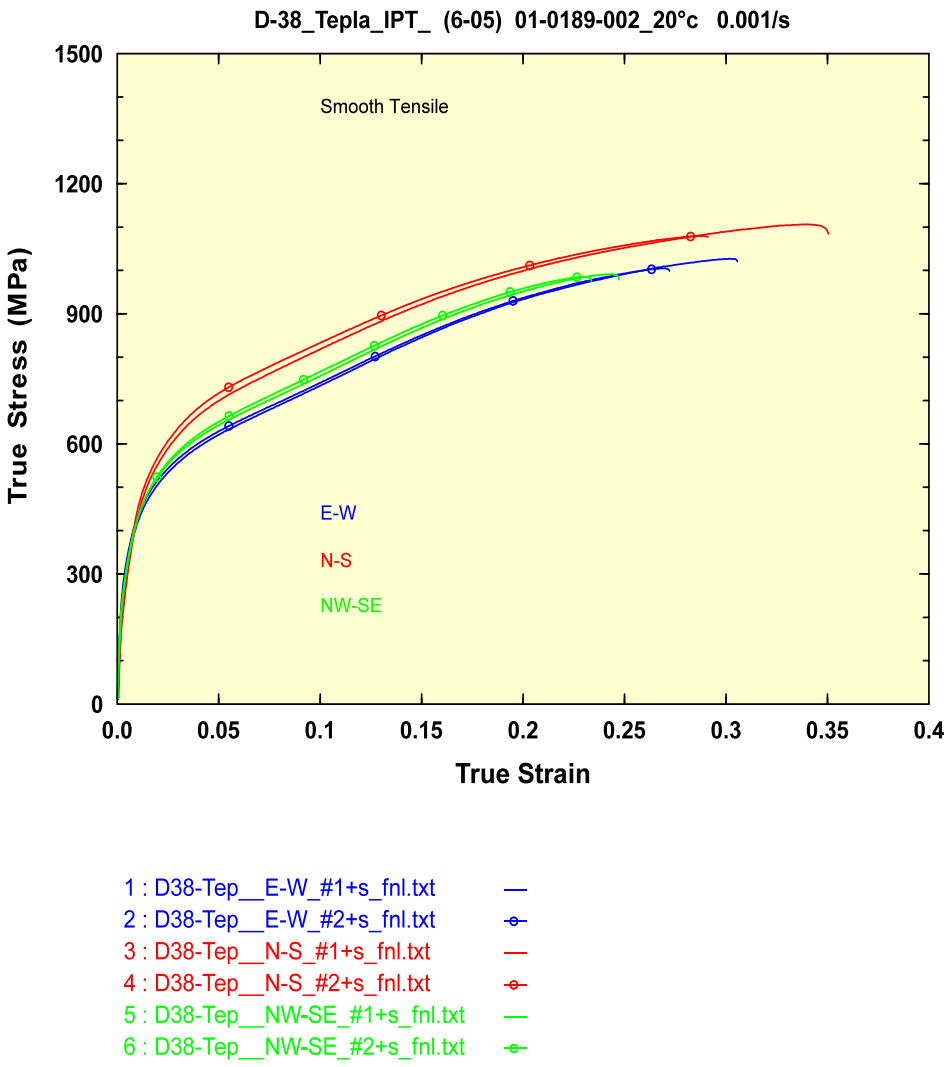

Figure 2: The quasi-static stress-strain response of smooth bar, as-annealed DU specimens in the N-S, E-W, and NW-SE texture directions.

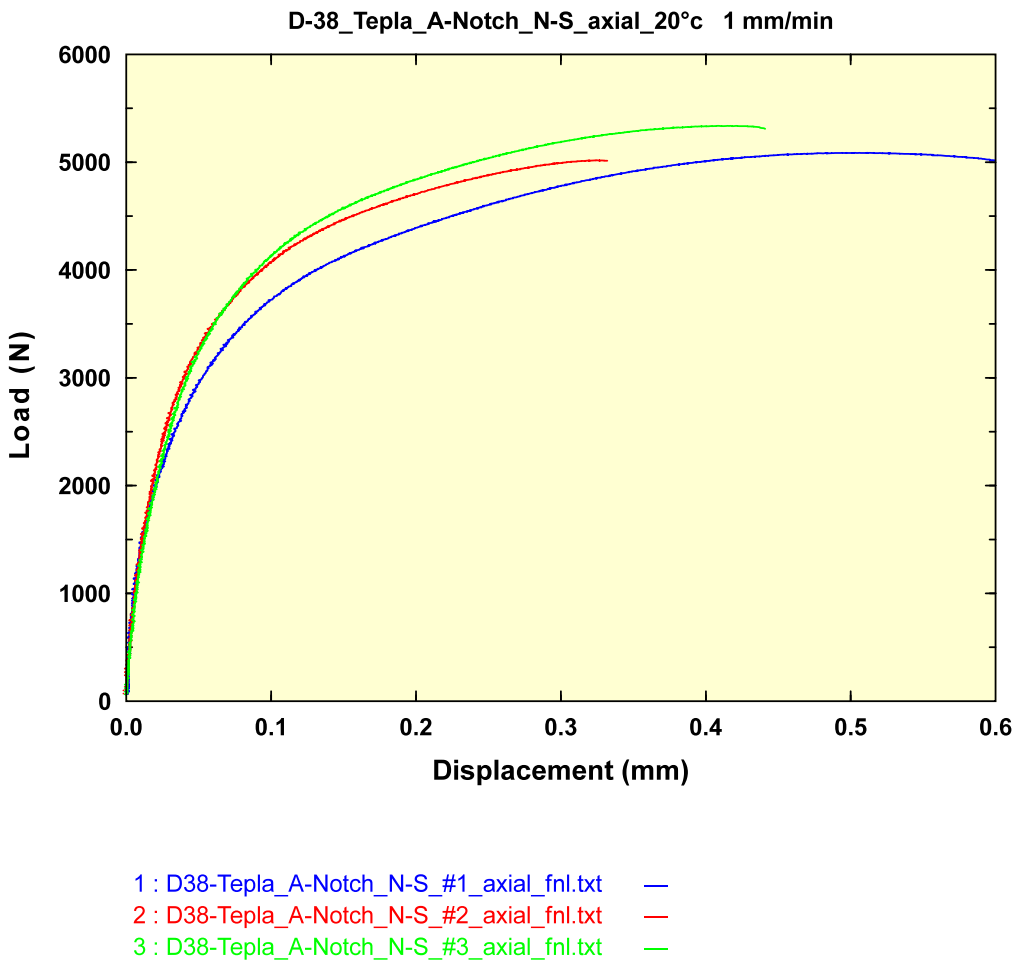

Figure 3: The quasi-static stress-strain response of A-Notch, as-annealed DU specimens in the N-S texture direction.

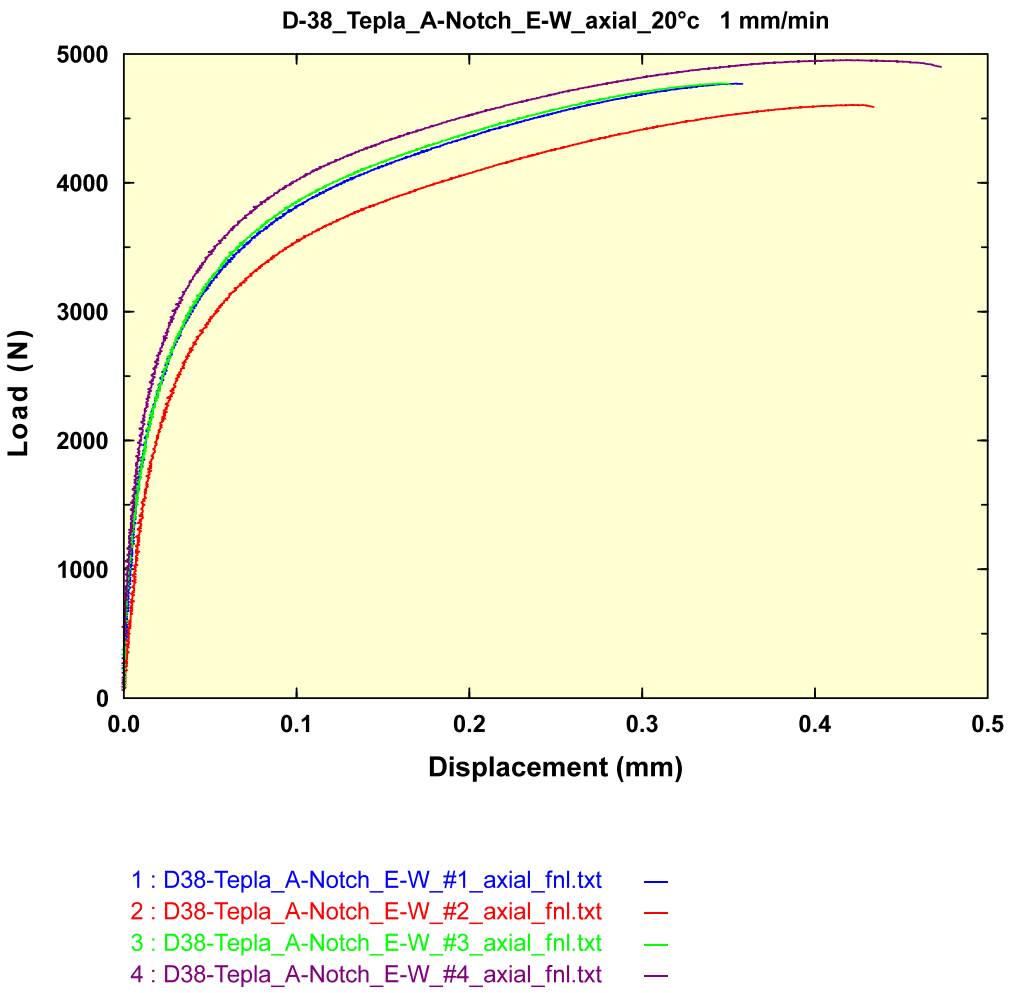

Figure 4: The quasi-static stress-strain response of A-Notch, as-annealed DU specimens in the E-W texture direction.

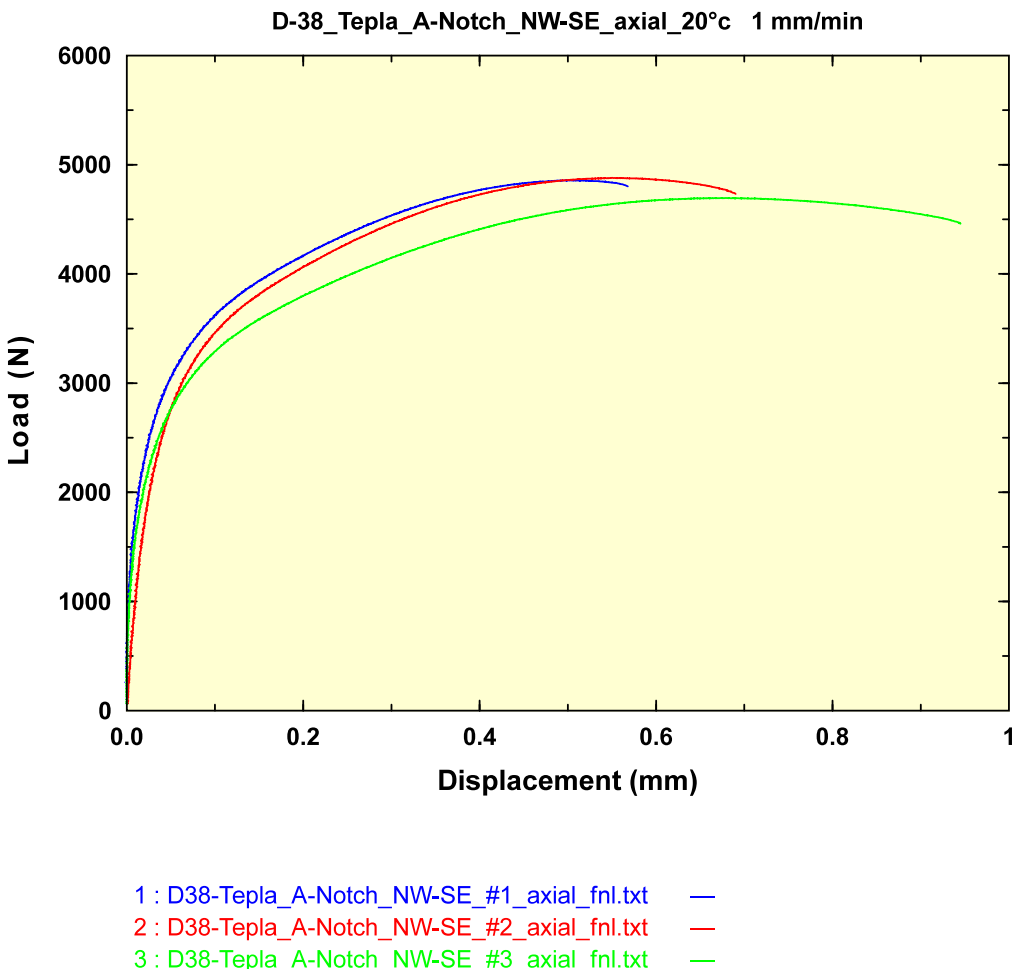

Figure 5: The quasi-static stress-strain response of A-Notch, as-annealed DU specimens in the NW-SE texture direction.

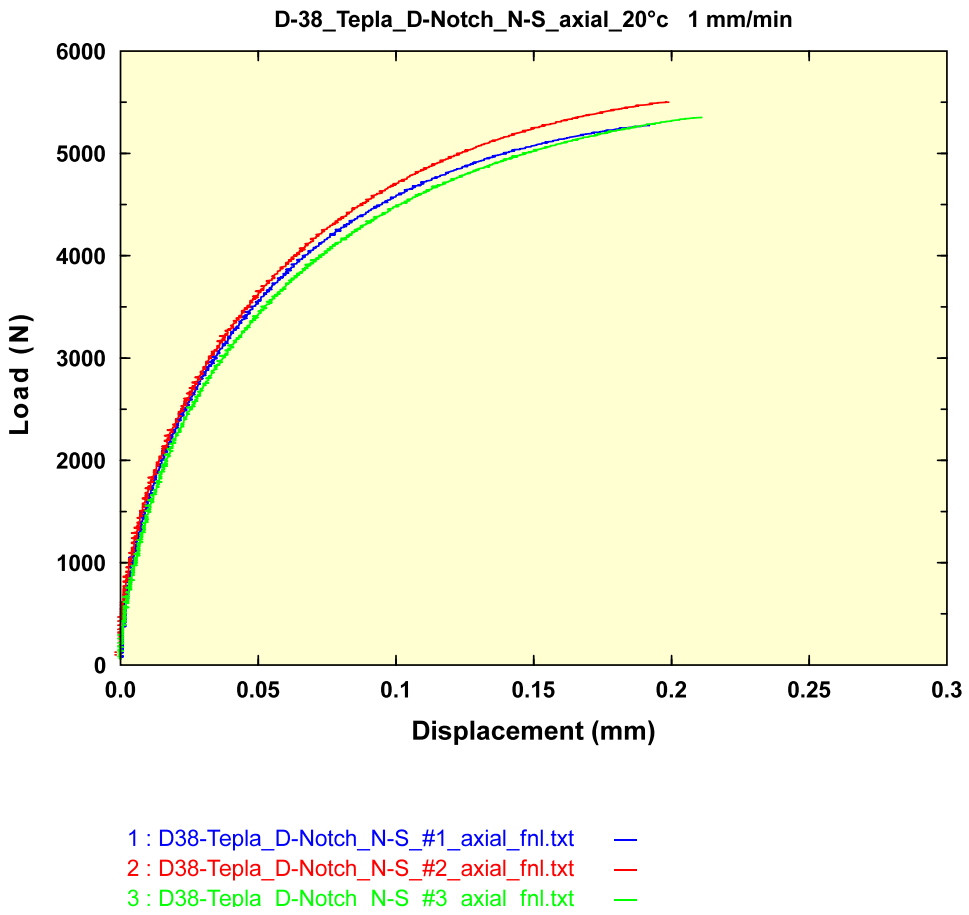

Figure 6: The quasi-static stress-strain response of D-Notch, as-annealed Du specimens in the N-S texture direction.

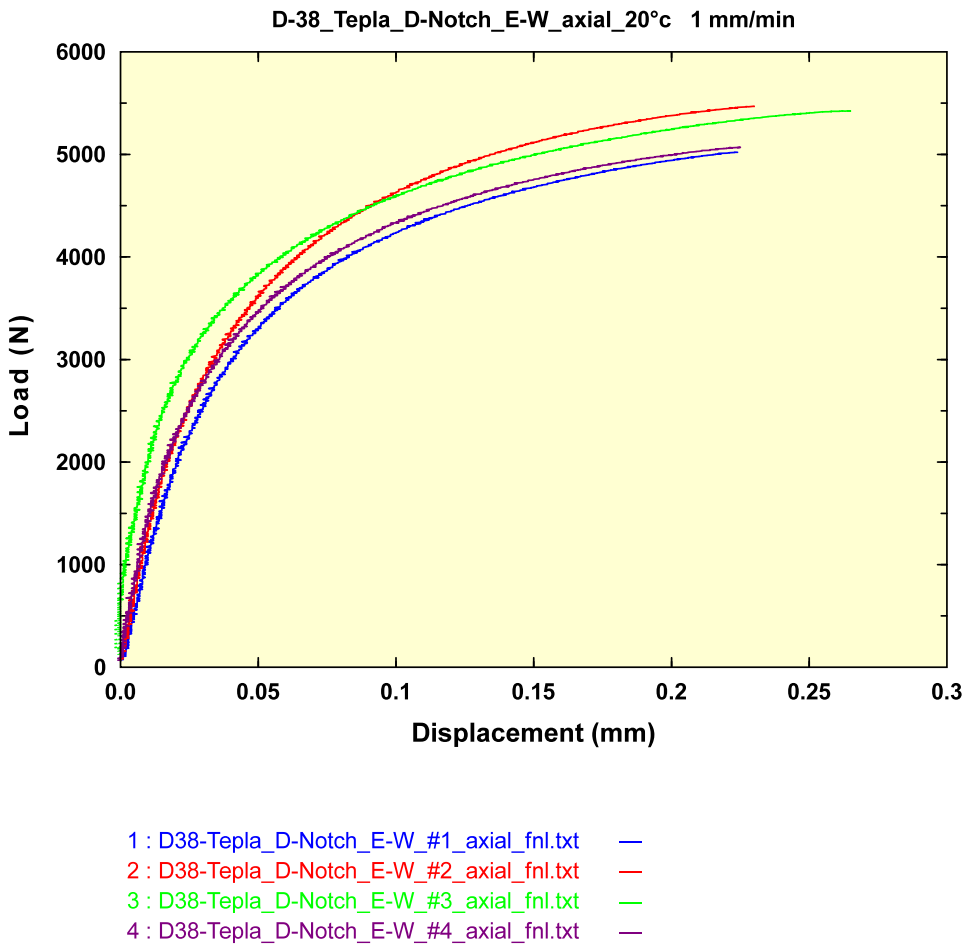

Figure 7: The quasi-static stress-strain response of D-Notch, as-annealed DU specimens in the E-W texture direction.

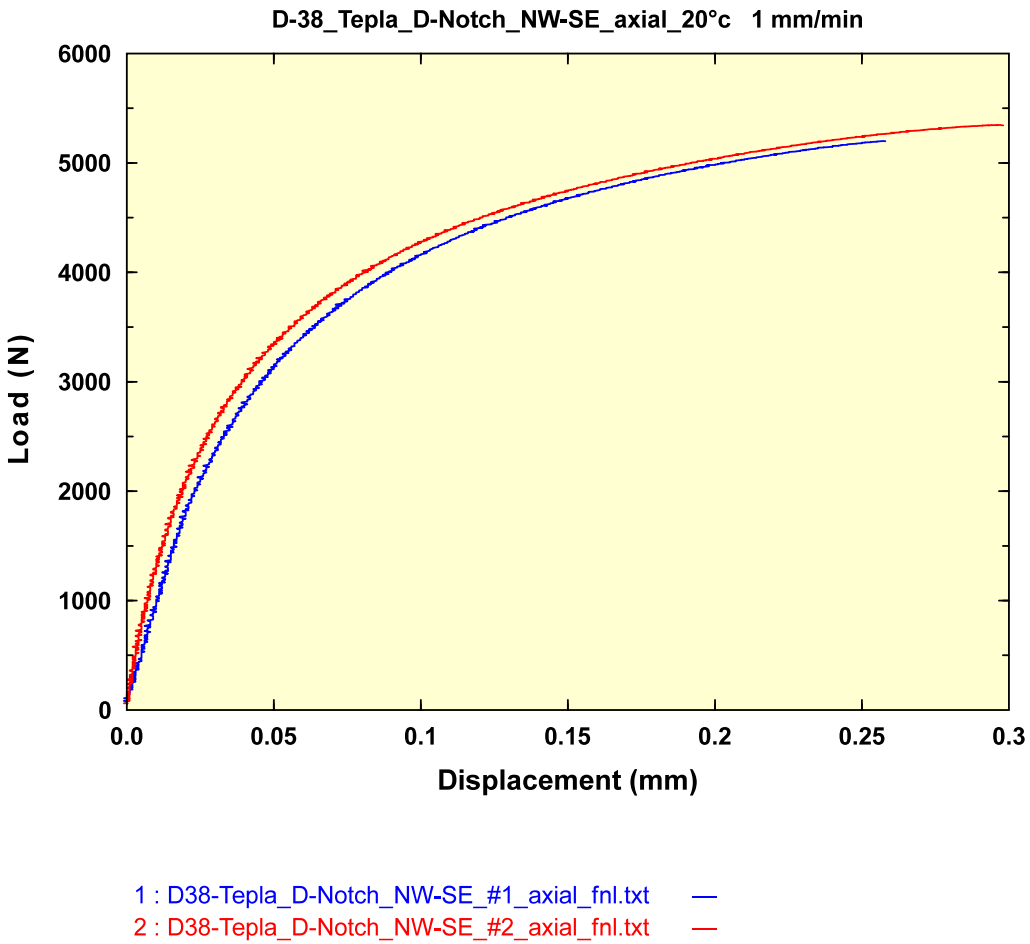

Figure 8: The quasi-static stress-strain response of D-Notch, as-annealed DU specimens in the NW-SE texture direction.

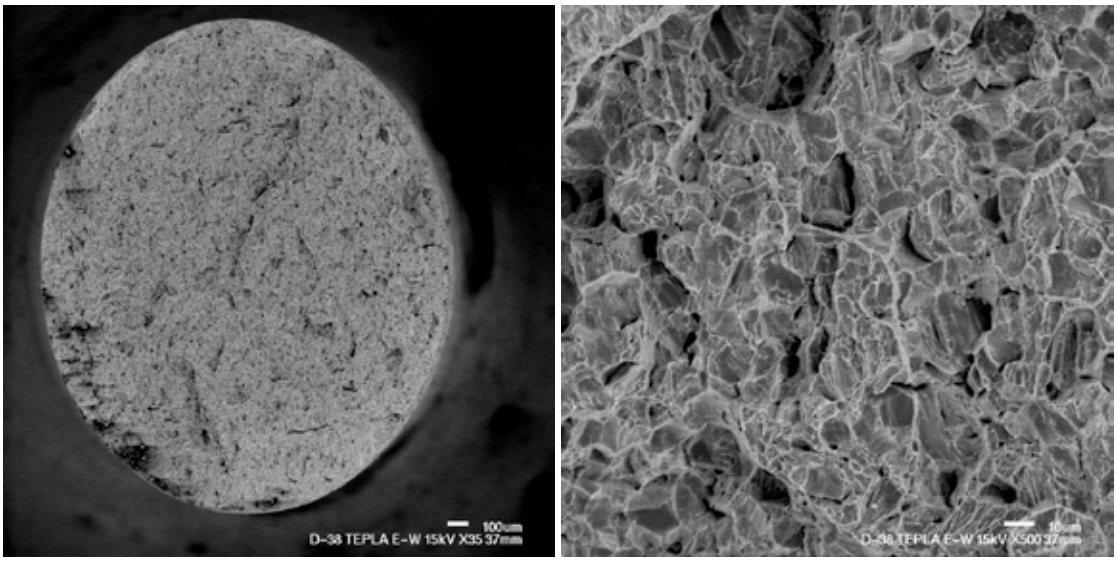

Figure 9: SEM of the fracture surface of the as-annealed, smooth bar specimen in the E-W texture direction.

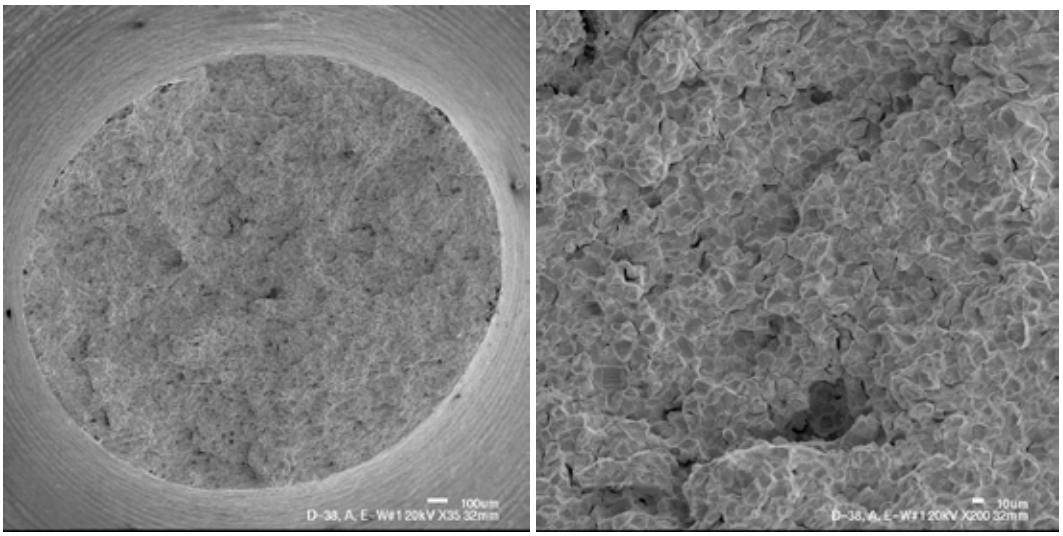

Figure 10: SEM of the fracture surface of the as-annealed, A-notch specimen in the E-W texture direction.

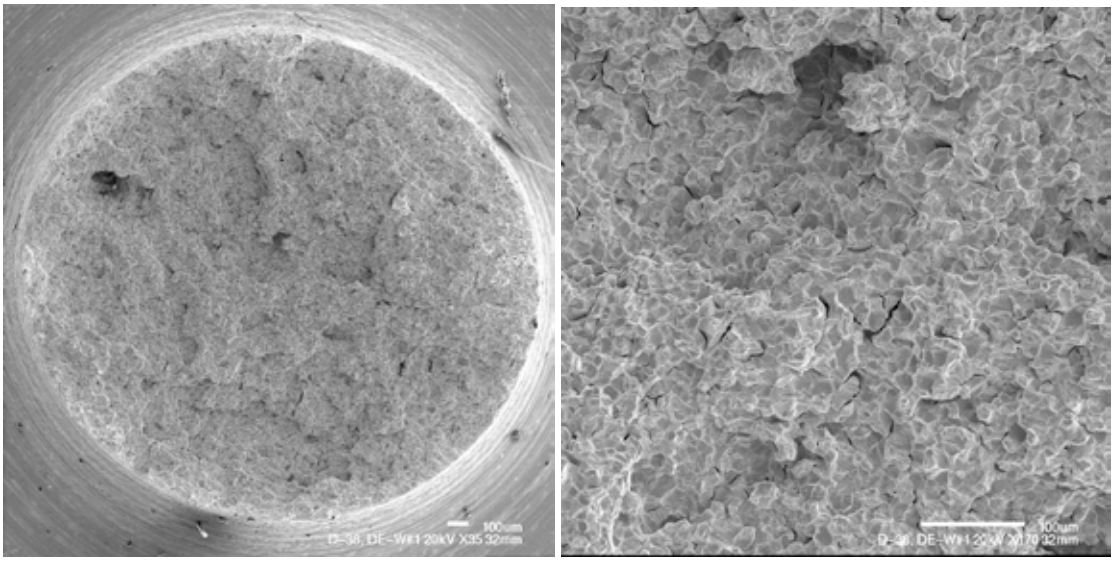

Figure 11: SEM of the fracture surface of the as-annealed, D-notch specimen in the E-W texture direction.

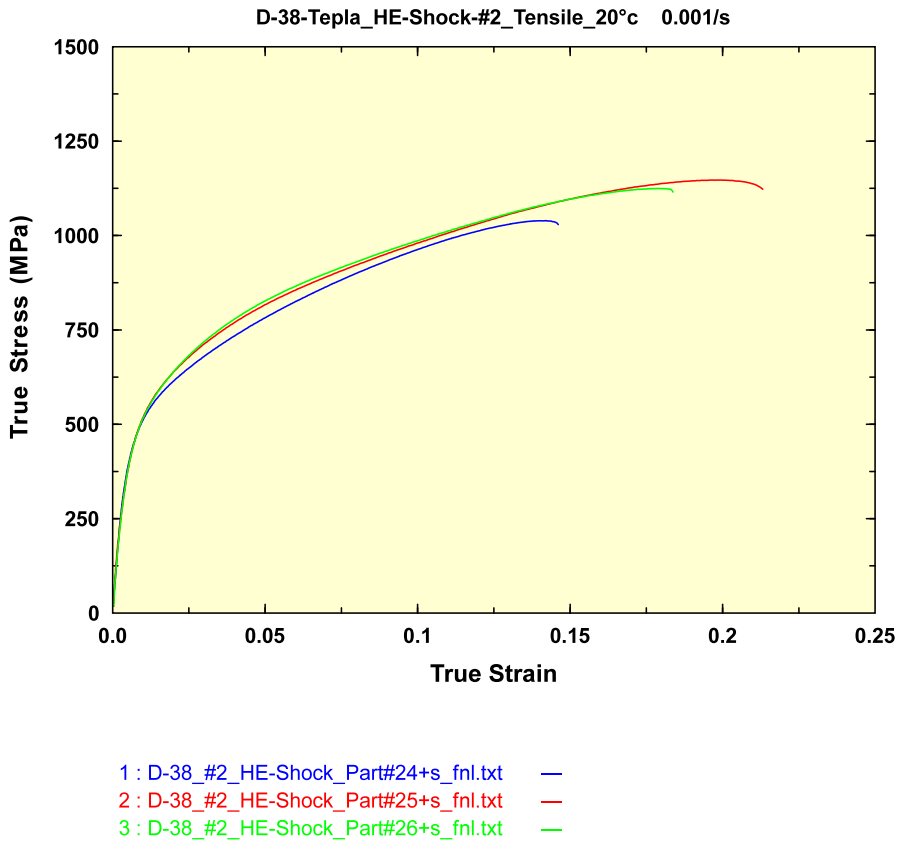

Figure 12: The quasi-static, stress-strain response of smooth bar, shock prestrained DU.

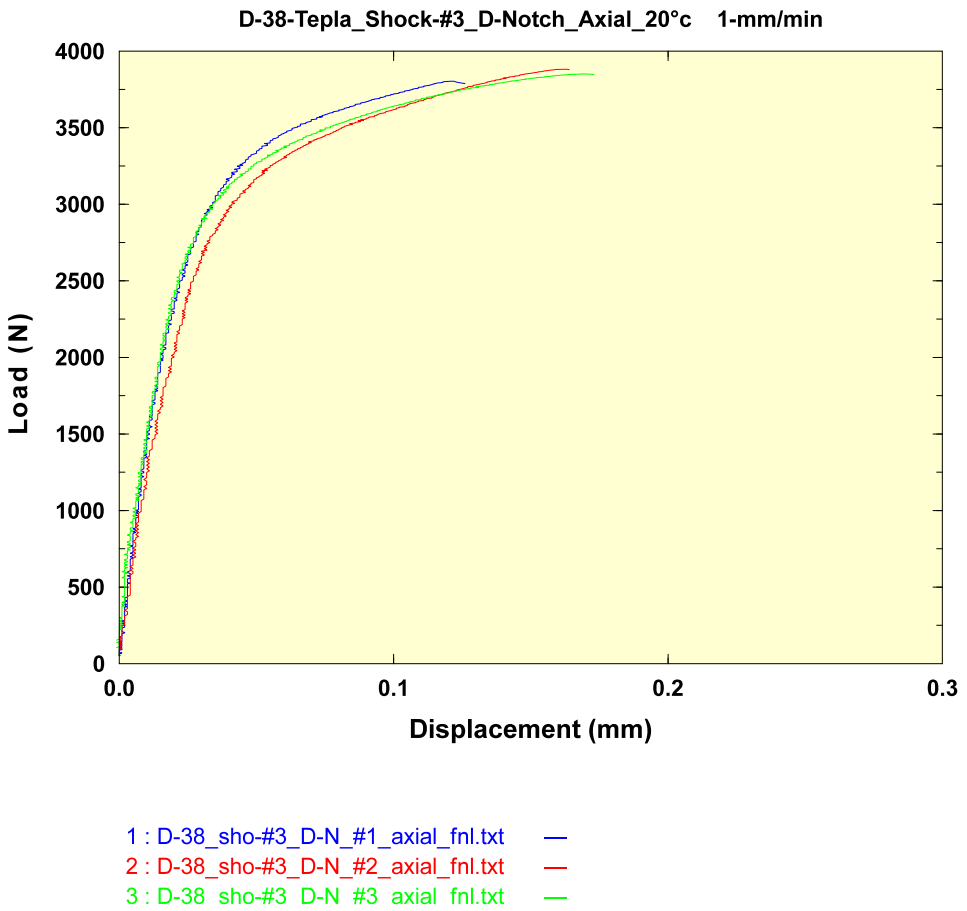

Figure 13: The quasi-static, stress-strain response of D-Notch, shock prestrained DU.

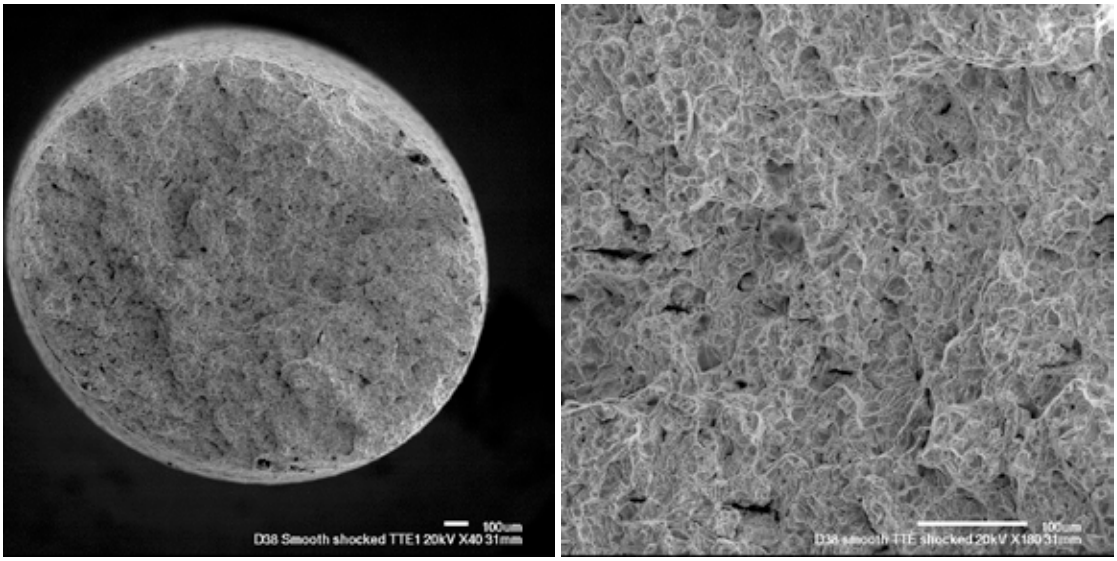

Figure 14: SEM of the fracture surface of the shock prestrained, smooth bar DU specimen.

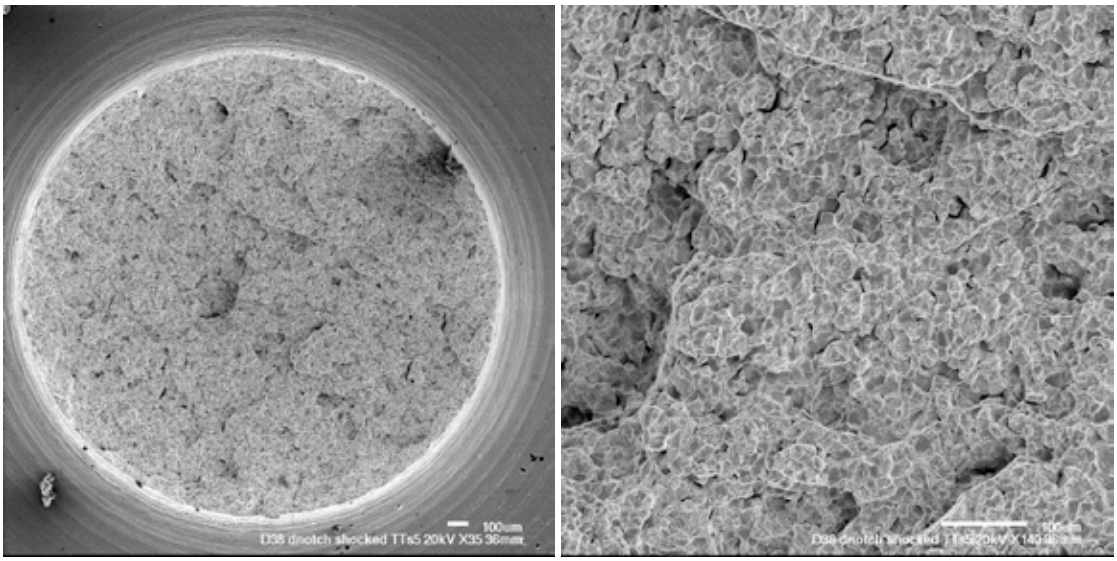
Figure 15: SEM of the fracture surface of the shock prestrained, D-Notch DU specimen.

Appendix 1: Diametral Data for the DU Tensile Tests

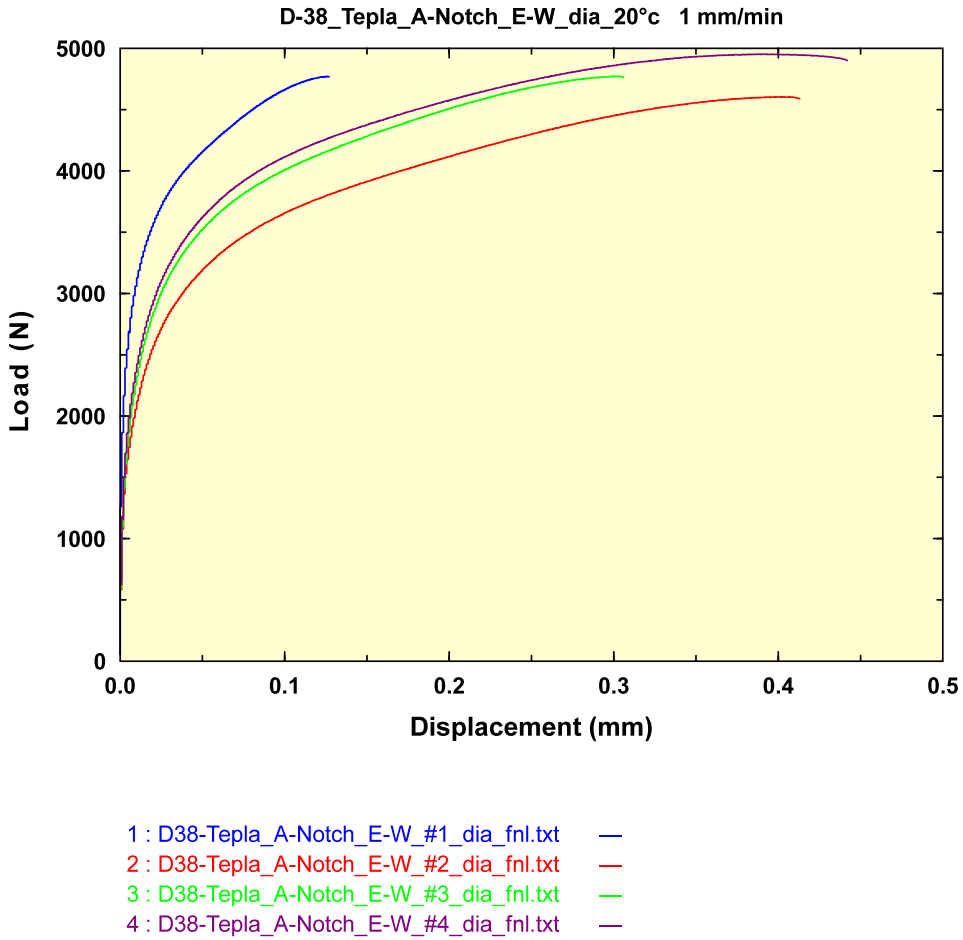

Figure 1: Diametral data for the as-annealed, A-notch, E-W, specimens.

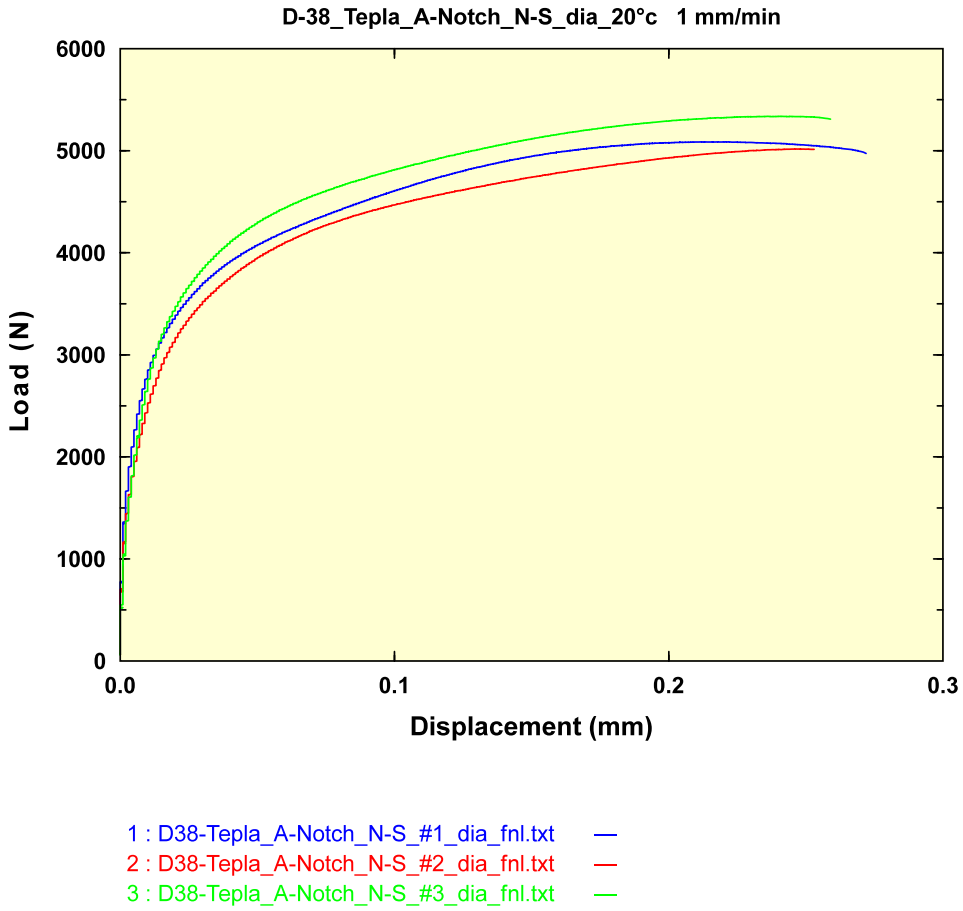

Figure 2: Diametral data for the as-annealed, A-notch, N-S, specimens.

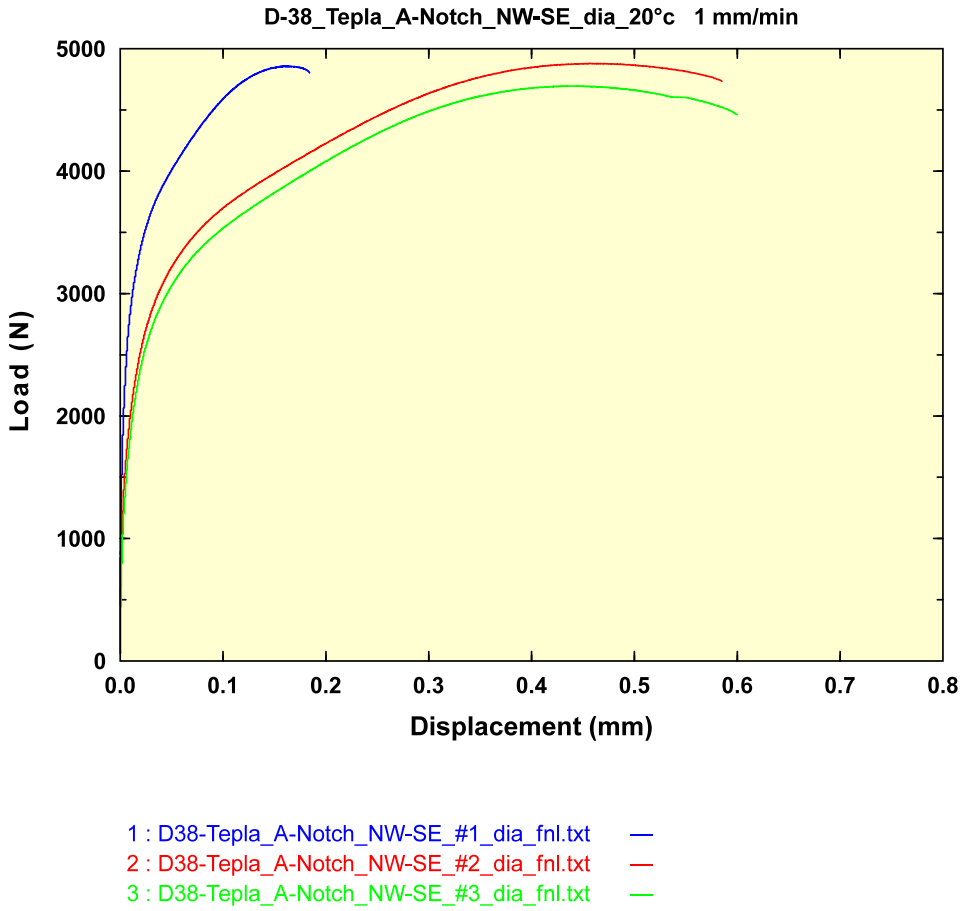

Figure 3: Diametral data for the as-annealed, A-notch, NW-SE, specimens.

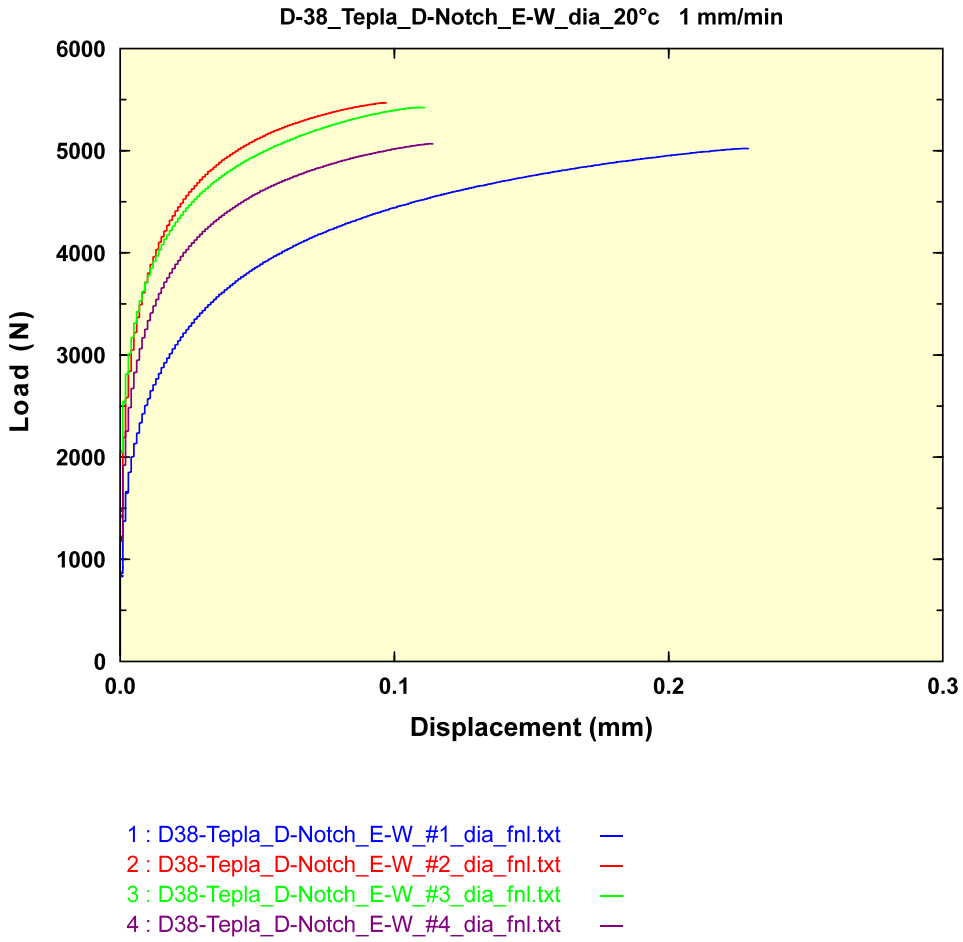

Figure 4: Diametral data for the as-annealed, D-notch, E-W, specimens.

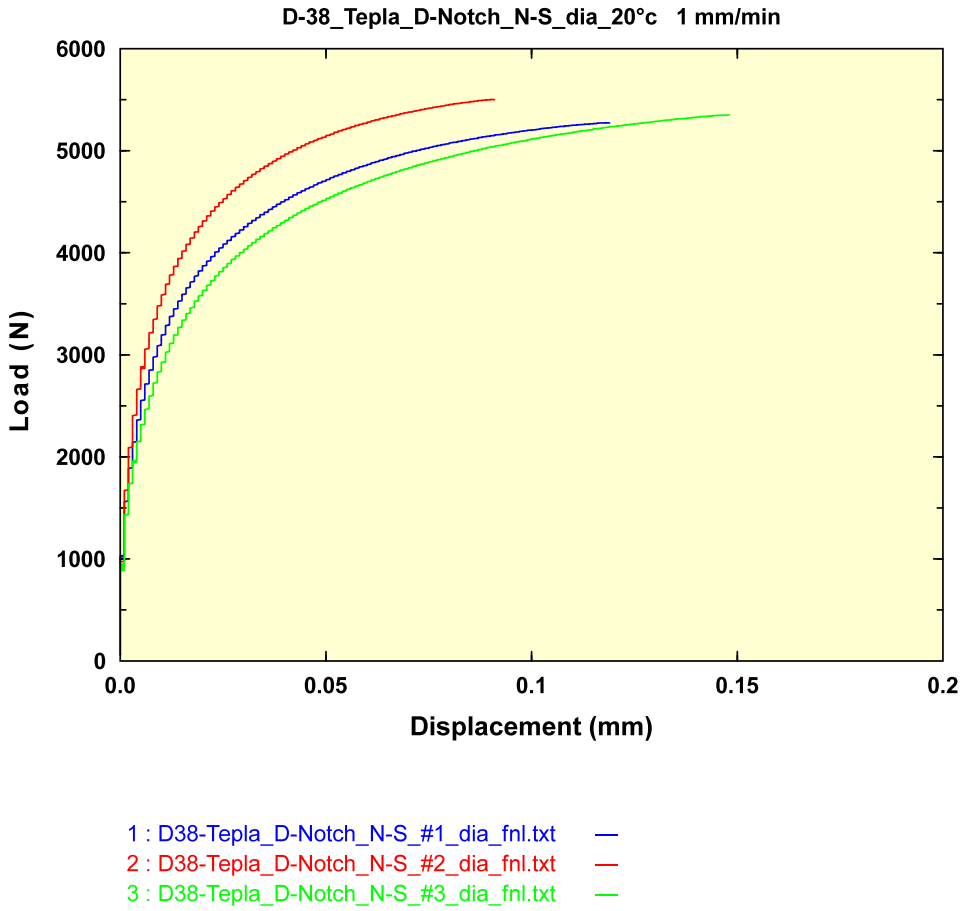

Figure 5: Diametral data for the as-annealed, D-notch, N-S, specimens.

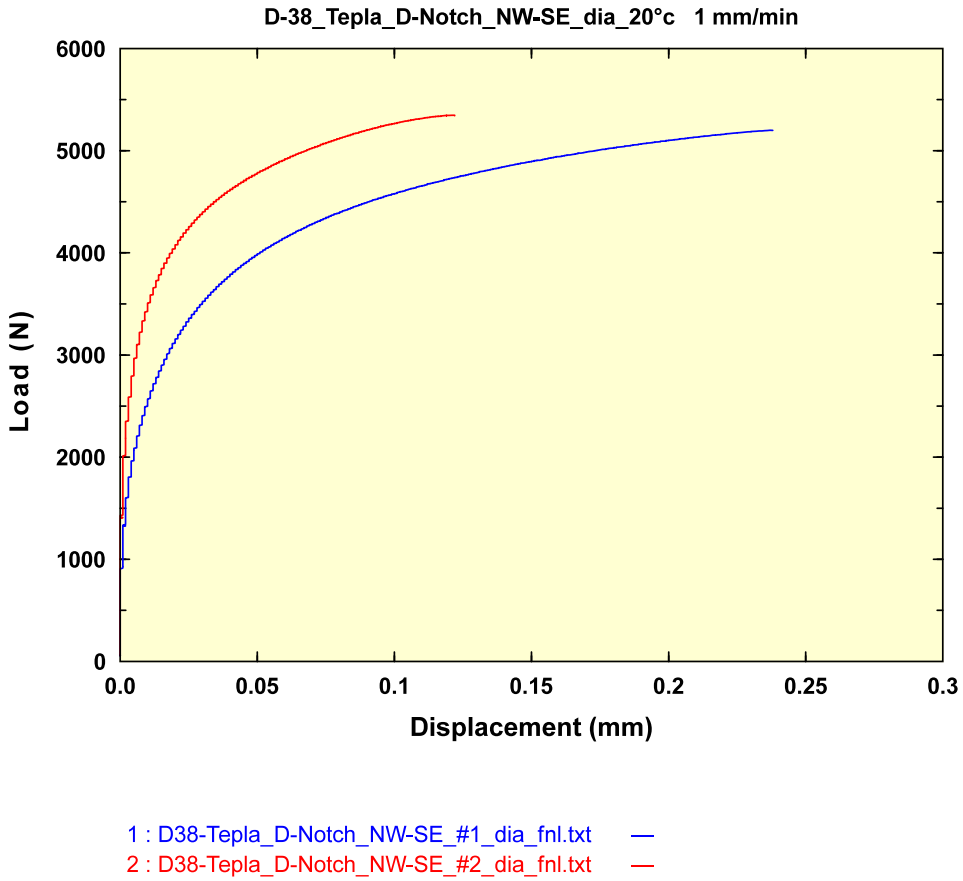

Figure 6: Diametral data for the as-annealed, D-notch, NW-SE, specimens.

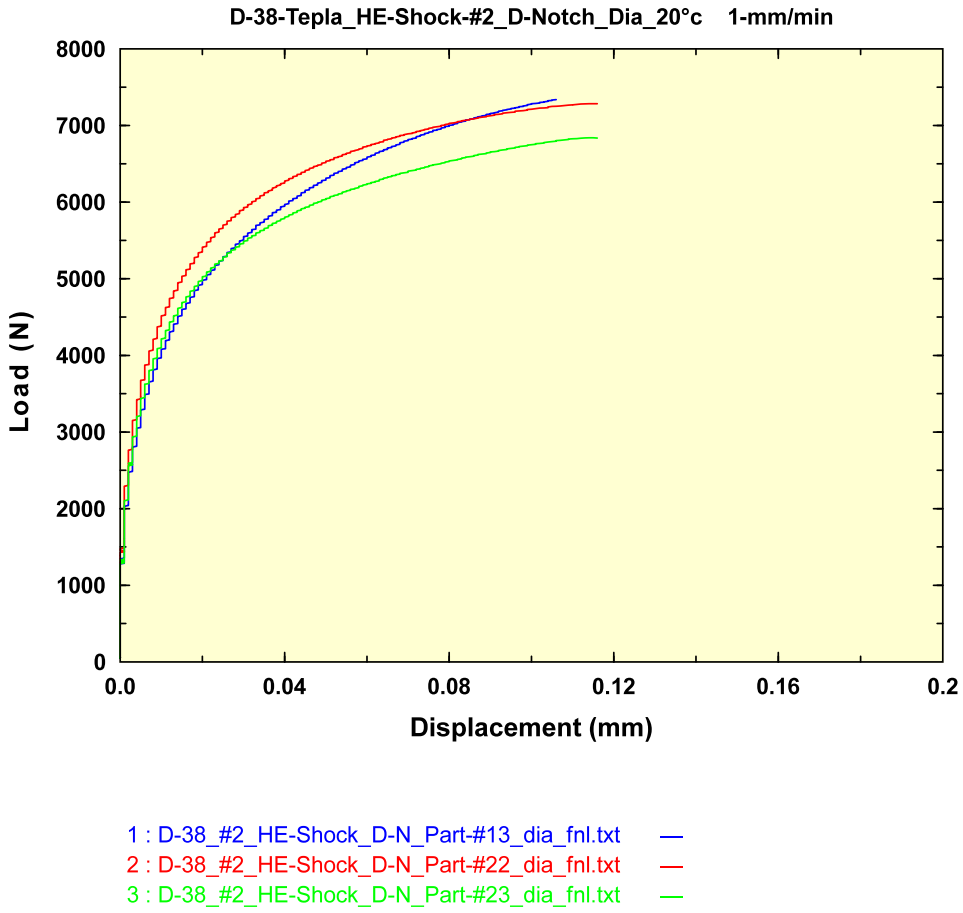

Figure 7: Diametral data for the shock prestrained, D-notch specimens.

SECTION 5: Influence of Energetic-Driven "Taylor-Wave" Shock-wave Prestraining on the Structure/Property Response of Depleted Uranium

G. T. (Rusty) Gray III, C.M. Cady, R.J. McCabe, R.S. Hixson, D.R. Korzekwa, and M.F. Lopez

Abstract: The influence of shock prestraining, via direct energetic "Taylor-wave" (triangular wave) loading, on the post-shock structure/property behavior of depleted uranium (DU) was studied. Samples were shock prestrained within a "soft" shock recovery fixture composed of momemtum traps and a spall plate to assure 1-dimensional loading. The DU samples exhibit roughly a 30% increase in yield strength following shock prestraining to ~45 GPa. The texture evolution in DU was quantified using electron-backscatter diffraction (EBSD). Detailed quantification of the substructure evolution following shock prestraining revealed high volume fractions of {130}, '{172}', and {112} deformation twins. The volume fraction of {130} twins was found to be ~10x the volume fraction of '{172}' and {112} twins. Details of the twin system activation and volume fraction relative to the local Schmidt factor within grains are presented. The influence of HE-driven shock prestraining on the structure/property response of DU is compared and contrasted to that seen in 304SS and 316SS subjected to "Taylor-wave" shock prestraining.

1. INTRODUCTION

Physically-based predictive modeling to support large-scale computer simulations of the high-strain-rate, large-strain plasticity, damage evolution, failure, and fragmentation of materials subjected to explosively-driven impulses, requires an understanding of how shock-wave loading affects material response. Over the past five decades, significant insight has been gained concerning the shock hardening and spallation response of materials subjected to shock-loading using "square-topped" shock profiles achieved via flyer-plate loading from either a gas gun or energetic drive[1, 2]. However, considerably less systematic quantitative information is known concerning the effect of direct, in-contact, high explosive (HE)-driven "Taylor-wave" or triangular-wave loading profile shock loading[3-5] on post-shock substructure evolution and mechanical behavior. This loading results in different prestraining and spallation on metals and alloys. Development of predictive capability for HE-driven shocks, therefore, requires the derivation and validation of advanced constitutive models that include the quantitative effect of shockwave profile shape on the substructure evolution and post-shock mechanical behavior of materials. Understanding the effect of the short pulse-duration, i.e., the time at the peak Hugoniot state which is known to strongly affect substructure evolution during shock hardening using square-wave loading[6], afforded by direct "Taylor-wave" energetic shock loading on substructure evolution remains a challenging endeavor. This is particularly complicated in materials whose plastic accommodation is derived from both dislocations and deformation twinning since extensive deformation twinning during shock-wave loading has been linked to kinematic processes on shock hardening, i.e., Bauschinger effect[7, 8].

Quantifying the physical properties of materials during the very rapid loading rate and short time interval during the actual passage of a shock wave through a material remains scientifically challenging. Research programs which couple both real-time and post-mortem

experimental measurements have demonstrated the greatest progress towards elucidating the operative shock processes occurring in ductile materials subjected to shockwave deformation and to support the development of physically-based model[1, 5]. In this paper the influence of direct energetic "Taylor-wave" shock prestraining on the substructure evolution and post-shock mechanical behavior of depleted uranium (DU) is presented. Quantitative analysis of the types and volume fractions of the deformation twins formed are presented.

2. EXPERIMENTAL TECHNIQUES

The material used for this investigation was a depleted-uranium plate material (DU) in 6.25 mm-thick plate form. The annealed DU possessed an equiaxed grain structure with an average grain size of 18 microns. The analyzed chemical composition of this depleted uranium (wt. pct.) was: 14 ppm Al, 40 ppm C, <10 ppm Ca, <10 ppm Fe, <2 ppm Mg, 4 ppm Mn, 11 ppm Ni, <10 ppm Si, and bal. U . The initial plate texture, quantified using orientation imaging microscopy (OIM), consisted of a strong [001] component in the plate through-thickness (TT) direction (max. 3.8 times random) with moderate texture asymmetries within the plane of the plate.

Shock recovery experiments were performed using direct-HE drive to impose a "Taylor-wave" triangular-shaped loading pulse to the DU samples. Depleted uranium samples were subjected to a HE-driven "Taylor-wave" pulse loading using a picture-frame shock recovery fixture[2] placed in contact with a 3-mm thick polymer buffer and explosively loaded by a 25.4-mm (1") thick piece of PBX 9501 driven by a 304.8-mm diameter (12") explosive (TNT/PBX 9501) plane-wave lens. The picture-frame recovery assembly was placed on top of a piece of 12.7-mm thick plywood in direct contact with ~600 liters of water. The central portions of the picture frame assembly components were fabricated from DU while the surrounding momentum-trapping rails, spall plate, and anvil were each fabricated from 304 SS. The loading history achieved in the DU is dictated by the detonation kinetics of the PBX 9501 and the impedance match into the DU target governed by the equation-of-state of the DU and PBX 9501 explosive. The peak pressure of the "Taylor wave" imposed on the DU sample is calculated to be nominally 45 GPa.

Quantification of the mechanical response of the DU in the annealed starting condition and following the "Taylor-wave" shock prestraining was accomplished by conducting compression tests on samples as a function of temperature and strain rate. Compression tests were conducted using an Instron™ screw-driven mechanical-test machine at an initial strain rate of 10^{-3} s^{-1} and using a split-Hopkinson Pressure Bar(SHPB) at a strain rate of ~2000 sec^{-1}. Cylindrical right-regular compression samples 5-mm in diameter by 5-mm long were used; the test samples were lubricated using moly-disilicide grease. Compression samples were sectioned from the shock-recovered disc parallel to the shock loading direction. For each set of testing conditions, at least two duplicate tests were performed to verify results. Specimens for optical metallography and electron backscatter diffraction (EBSD)[9] were sectioned from the annealed DU starting material and the shock-recovered samples and prepared with techniques discussed elsewhere[10]. Automated EBSD scans were performed at 25 kV in an FEI XL30 ESEM equipped with TSL data acquisition software. Regions were orientation mapped with step sizes ranging from 0.1 to 1 μm in a hexagonal grid. For the as-annealed sample, a 1 μm step size provided adequate grain detail. The OIM maps for the shocked material shown used a 0.2 μm step size. Twin boundaries were classified with the TSL-OIM Analysis 4 software using a

misorientation of 180º ± 5º about either K_1 or η_1 depending on whether the twin was Type I or Type II, with either working for the {130} compound twin. This method of twin identification is equivalent to the more common method of EBSD twin identification that defines a twin boundary based on a "minimum rotation" about the direction common to both parent and twin orientations necessary to bring the matrix and twin orientations into coincidence"[11].

3. RESULTS AND DISCUSSION

3.1 Substructure Evolution

The substructure of the shock prestrained DU was examined optically and the types and volume fractions of the deformation twins were quantified using EBSD scans. Twin volume fractions were measured with the OIM Analysis 4 software that calculates the parent versus daughter portion of a twinned grain based on a majority rule criterion. The majority rule criterion assigns the largest orientation fraction of a twinned grain as parent, and this criterion was found to provide high quality identification of the deformation twins formed in the shocked DU.

Figure 1a shows an EBSD image of the annealed DU material illustrating the equiaxed grain structure of the DU material studied and the absence of twins in the starting material. The color IPF (inverse pole figure) legend is a standard IPF that displays the actual orientation of the through thickness direction using a standard uranium orientation triangle. The images for the shock-prestrained DU samples were taken from a depth of about 4.1 mm from the shock impact surface, which is at approximately 75% of the plate thickness. The shocked microstructure was quantified using a 0.2 μm EBSD step size. Figure 1b shows the distribution of twins formed in the shock prestrained DU while Figure 2a identifies the three twins activated; {130}, {172}, and {112}.

Most of the regions where the TT sample direction is at a high angle to [001] are either '{172}' or {112} twins. {130} twinning results in a 69° rotation of material about the [001] axis. This change in orientation does not result in a considerable change in the overall texture as the initial texture has a strong [001] component near the shock direction, and the rotation is about this direction. Notice that many of the {130} twins have a similar TT orientation to their parent.

In this area, the projected thickness of {130} twins and fraction of grains twinned seems to correlate with the Schmid Factor in each grain; grains oriented with the maximum critical resolved shear stresses relative to the "nominal" shock loading direction. Twins not intersecting a grain boundary in the section are lenticular. Again the trend in twin thicknesses and fraction of grain twinned with Schmid Factor is observed.

Almost all grains in the preshocked sample displayed some {130} twins. Based on a 1mm OIM step size, the volume fraction of twins across the thru-thickness of the shock prestrained sample was quantified. The volume fraction of {130} twins was found to vary from around 16% down to 8% across the sample TT, while the volume fractions of '{172}' and {112} twins were both reasonably consistent at around 2% across the sample. The volume fraction of {130} twins is a lower limit as very fine {130} twins, below the resolution of the current EBSD scan, were indicated.

3.2 Mechanical Behavior

The influence of temperature and strain rate on the mechanical behavior of annealed DU is presented in Figure 3a. Increasing the strain rate and/or decreasing the temperature of deformation is seen to influence the flow stress and work-hardening behavior of DU. Increasing the strain rate from 0.001 to 0.1/sec at 22°C is seen to result in a modest increase in yield strength and virtually no influence on the rate of strain hardening; i.e., the stress-strain curves are parallel after yielding. This type of constitutive response is consistent with the mechanical behavior of many body-centered-cubic, hexagonal, and lower-crystal-symmetry metals and alloys whose mechanical behavior is principally controlled by a strong Peierls stress[12]. Changing the temperature of deformation from +100 to -75°C in DU at a strain rate of 0.01/sec is seen to affect modest changes, ~150 MPa, to the yielding while more significantly increasing the rate of work hardening with decreasing temperature; 500 MPa at a strain of 0.2.

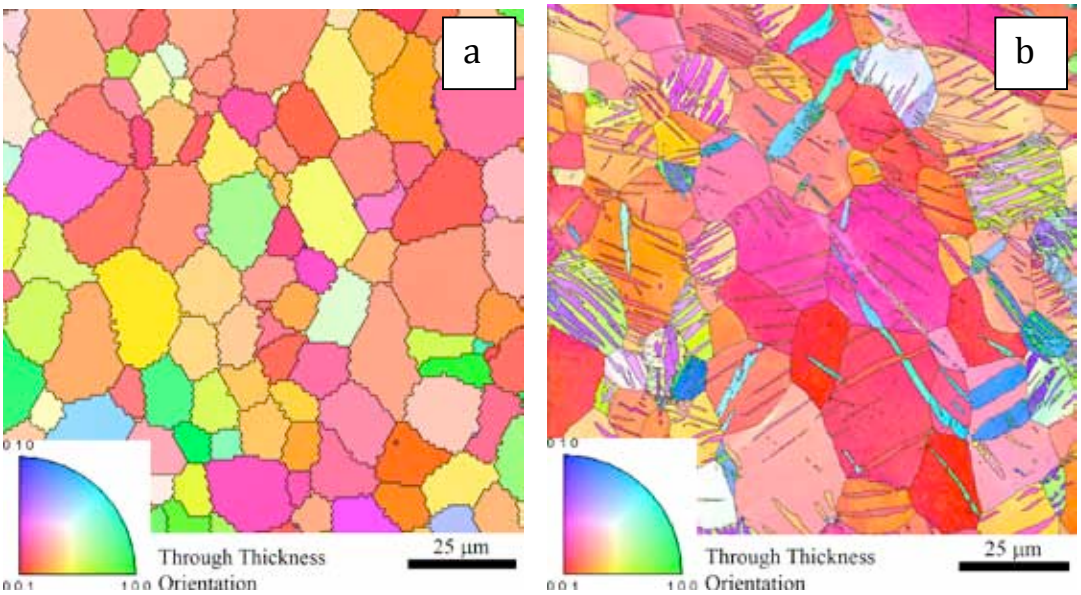

FIGURE 1. Electron-back-scatter diffraction micrographs of the (a) starting annealed DU, (b) shock prestrained DU.

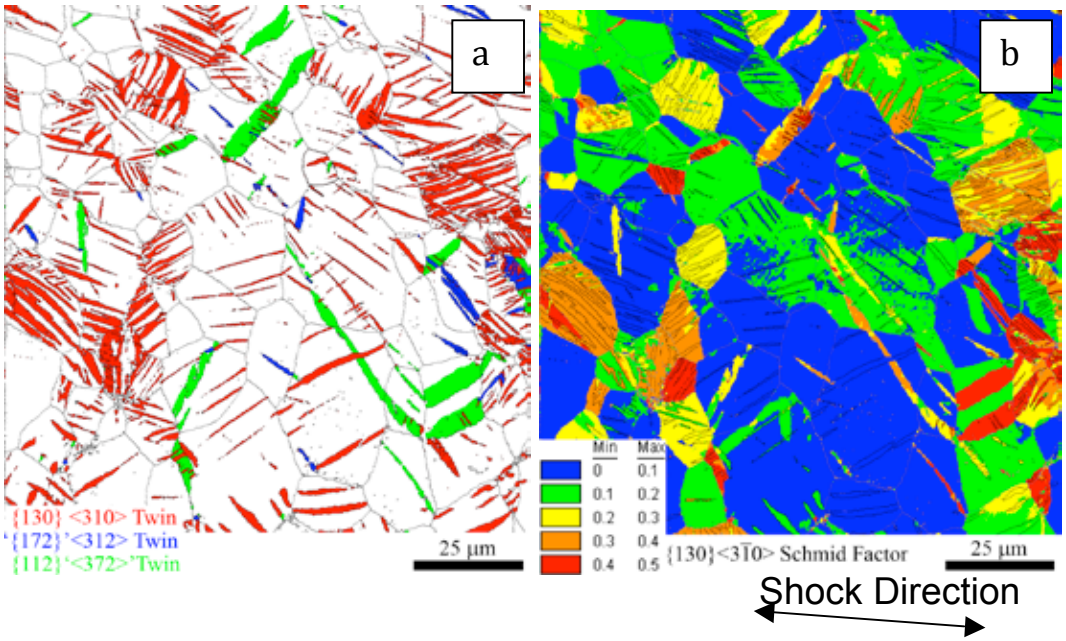

FIGURE 2. Electron-back-scatter diffraction micrographs showing (a) identification of the specific types of deformation twins activated in the shock prestrained DU and (b) the correlation of the specific twins activated relative to the "nominal" Schmidt factor for each grain orientation; the shear stress in the grain assuming the "nominal" 1-dimentisonal applied shock loading direction.

The increase in strain hardening rate in DU with decreasing temperature is seen to correlate microstructurally with an increased propensity of deformation twinning. The increase in the flow stress and increased twinning propensity of DU due to increasing strain rate / decreased temperature is consistent with the previous study mechanical behavior and substructure evolution in DU by Armstrong et al.[13].

The influence of strain rate and temperature on the constitutive response of the shock-prestrained DU is presented in Figure 3b. Through comparison of Figures 3a and 3b it is readily apparent that shock prestraining has increased the flow strength of DU compared to the annealed condition. The quasi-static compressive yield strength of DU is seen to increase by nominally 200 MPa due to shock prestraining. Further, shock hardening is seen to significantly increase the temperature dependence of the constitutive response of DU. Decreasing the temperature of loading at a strain rate of 0.01/sec from 22 to -75°C in the shock-prestrained material is seen to increase the yield strength from 800 to 1000 MPa. The increase in the flow stress, for loading at a strain rate of 0.01/sec, for the shock-prestrained DU at a true strain of 0.2 for temperatures of +100 to -75°C is 1000 to 1600 MPa, respectively. The stress-strain response measured at -75°C at 0.01/sec and that at 20°C when loaded dynamically at 2000/sec are additionally seen to be essentially identical suggesting similar suppression of thermal activation

The shock hardening observed is believed to significantly affected by the extensive deformation twinning in DU. Comparison of the quasi-static reload yield strength of the shock-restrained DU to the flow stress of the annealed material following ~28% plastic strain, nominally equivalent to the shock transient strain, supports a substantial Bauschinger influence on shock hardening in DU consistent with previous wave profile analysis[14]. However, distortion of the twins suggests significant dislocation activity after formation of the twins

consistent with plastic deformation[13, 15]. Future studies will focus on quantification of both the influence of shock-wave loading pulse shape and the Bauschinger effect on shock hardening in DU.

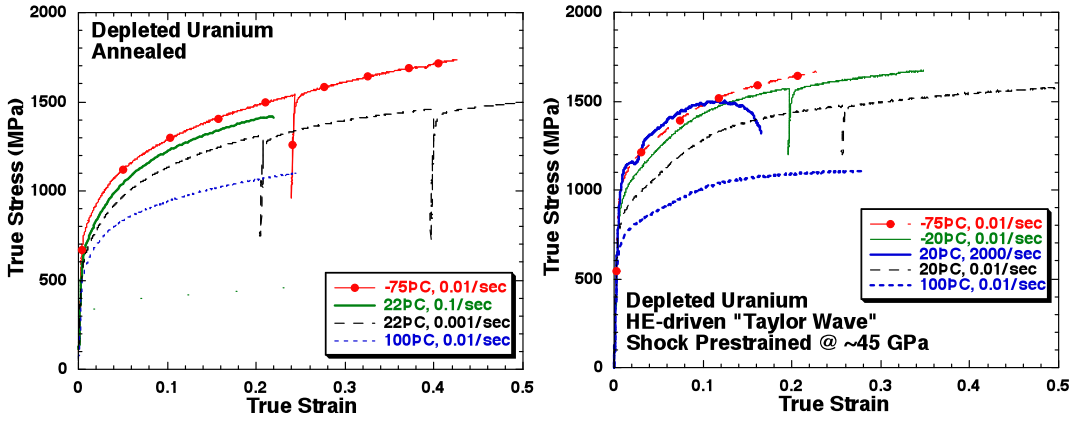

FIGURE 3. Compressive true-stress true-strain mechanical behavior of depleted uranium as a function of temperature and strain rate for a) annealed DU and, b) the DU material following HE-driven "Taylor wave" shock prestraining to ~45 GPa.

4. SUMMARY AND CONCLUSIONS

The current study of the effect of "Taylor-wave" energetic-driven shock prestraining on the structure/property behavior of depleted uranium (DU) reveals that:

1) He-driven "Taylor-wave" shock prestraining of DU to ~45 GPa is found to lead to significant increases in the defect density, in particular deformation twinning, and commensurate mechanical response of DU.
2) Energetic-driven shock prestraining of DU is seen to result in the formation of a significant volume fraction, 8-16%, of {130} deformation twins and a modest volume fraction, 2%, of '{172}' and {112} deformation twins.
3) Shock hardening in DU affords a significant increase in the post-shock mechanical behavior of DU;
4) Automated EBSD techniques can provide insight into the details of microstructural evolution during shock hardening of metals and alloys. This spatially-resolved data, which provides statistically appropriate information on deformation mechanisms and quantification of their relative activity, volume fractions, as a function of shock hardening and orientation is required to the development and validation of predictive material models.

References

[1] G. T. Gray III, "Influence of shock-wave deformation on the structure/property behavior of materials", in High-Pressure Shock Compression of Solids, J. R. Asay and M. Shahinpoor, eds., Springer-Verlag, vol. 1993, pp. 187-216.
[2] G. T. Gray III, "Shock wave testing of ductile materials", in ASM Handbook. Vol. 8: Mechanical Testing and Evaluation, H. Kuhn and D. Medlin, eds., ASM International, vol. 2000, pp. 530-538.
[3] J. N. Johnson, *J. Appl. Phys.*, **52** (1981) 2812-2825.
[4] G. T. Gray III, N. K. Bourne, B. L. Henrie and J. C. F. Millett, *J. Phys. IV France*, **110** (2003) 773-778.
[5] D. D. Koller, R. S. Hixson, G. T. Gray III, P. A. Rigg, L. B. Addessio, E. K. Cerreta, J. D. Maestas and C. A. Yablinsky, *J. Appl. Phys.*, **98** (2005) 103518.
[6] G. T. Gray III, "Influence of Shock-Wave Deformation on the Structure / Property Behavior of Materials", in High Pressure Shock Compression of Solids, J. R. Asay and M. Shahinpoor, eds., Springer-Verlag, vol. 1993, pp. 187-215.
[7] G. T. Gray III, R. Hixson and C. E. Morris, "Bauschinger Effect During Shock Loading", in Shock Compression of Condensed Matter - 1991, S. C. Schmidt, R. D. Dick, J. W. Forbes and D. G. Tasker, eds., Elsevier Science Publishers B.V., 1992, p. 427-430.
[8] A. Rohatgi, K. S. Vecchio and G. T. Gray III, *Acta mater.*, **49** (2001) 427-438.
[9] B. L. Adams, S. I. Wright and K. Kunze, *Metallurgical Transactions A*, **24A** (1993) 819-831.
[10] R. J. McCabe and D. F. Teter, *J. of Microscopy*, (2006) in press.
[11] J. F. Bingert, R. J. Hanrahan, R. D. Field and P. O. Dickerson, *J. of Alloys and Compounds*, **365** (2004) 138-148.
[12] S. R. Chen and G. T. Gray III, *Metall. Trans.*, **27A** (1996) 2994-3006.
[13] P. E. Armstrong, P. S. Follansbee and T. Zocco, *Inst. Phys. Conf. Ser.*, **102** (1989) 237-244.
[14] S. Cochran and D. Banner, *J. Appl. Phys.*, **48** (1977) 2729-2737.
[15] G. T. Gray III, *Acta Metallurgica*, **36** (1988) 1745-1754.

Section 6: Incipient Spall of DU SPY007 (Cold Rolled vs. Annealed)

Darcie Dennis-Koller (WX-9), E.K. Cerreta (MST-8), G.T. Gray III (MST-8), A.M. Kelly (MST-6), R. McCabe (MST-6), and P.A. Papin (MST-6)

Abstract: Dynamic damage studies on depleted uranium samples have revealed mixed mode failure mechanisms leading to incipient cracking as well as ductile failure process. Results show that delamination of inclusions upon compression may provide nucleation sites for damage initiation in the form of crack tip production. However, under tension the material propagates cracks in a mixed brittle and ductile failure mode. Cracks tips appear to link up through regions of severe, shear dominated plastic flow. Shock recovery experiments were conducted on a 50mm, single-stage, gas gun. Direct high explosive drive experiments were also conducted. Serial metallographic sectioning was performed on all recovered samples to characterize the bulk response of the sample. Results show damage illustrating ductile plasticity joining mixed-mode cracking.

Introduction:

Shock compression techniques are often used to investigate tensile damage in metals subjected to extreme loading conditions. Dynamic tensile damage occurs when rarefaction (expansion) waves within a material interact in such a manner as to produce tensile stresses in excess of the threshold required for damage initiation [1]. If the tension is of sufficient amplitude, damage will accrue and thereafter a new interface will form within the material, creating a "spall layer". Plate impact experiments offer several advantages to the investigation of dynamic tensile damage over other techniques including the ability to maintain truly one-dimensional, planar strain loading conditions for the duration of the experiment and the ability to recover the material for post-experiment metallurgical analysis.

Evidence that a spall layer has been created in a plate impact experiment is often obtained using a velocity interferometer system for any reflector (VISAR) or photonic Doppler velocimetry (PDV) [2] and has been the subject of numerous studies [3,4]. In general, the free surface velocity profile obtained using VISAR or PDV shows ringing consistent with wave reflections within a layer thinner than the original sample. If the tension is not of sufficient amplitude to form a completely separate layer, a region of significant damage – consisting of a localized band of voids and or cracks, for example – may still exist. This region may be of significantly lower impedance than the undamaged region and may produce a velocity profile similar or even identical to that obtained from the completely separated layer. Insight into this type of ambiguity can be found through post experiment sample recovery and material analysis. Early studies into the spall response of DU have been conducted [5,6] in an effort to better understand the cumulative dynamic response of this material.

To this end, the full and incipient spall response of DU SPY007 to dynamic shock loading has been investigated through both plate impact and direct explosive drive experiments. In-situ diagnostics as well as post mortem characterization was utilized to

examine both the continuum-level spall behavior as well as the meso-scale features of the microstructure that are linked to initial damage in the material. Experiments revealed that both as-received and as-annealed, high-purity, depleted uranium fails through a process of shear cracks and ductile void nucleation, growth and coalescence.

Material:

The material utilized in this study is described in Section 1 of this report. For the incipient spall experiments, it was utilized in both the as-received, cold rolled condition as well as in the as-annealed condition.

Shock Experiments (Plate Impact)

Plate impact experiments were conducted using a smooth bore 50 mm diameter light gas gun. Sapphire impactors were mounted to the front of aluminum sabots and accelerated down the barrel to velocities of approximately 300 m/s. Spall was generated in the sample when rarefaction waves generated at the back of the impactor traveled back into the sample and interacted (in the bulk of the target sample) with the rarefaction waves generated at the free surface of the sample material. When this interaction begins, a tensile region is formed which leads to damage and ultimately spall in the material [9].

To ensure that recovered samples have been subjected only to a known uni-axial loading/unloading history, it is important to prevent the sample from undergoing any significant radial release. Typically, this is accomplished by placing rings around the sample made of the same material referred to as "momentum trapping" rings. If properly designed, the rarefaction release wave relieves the stress to zero in the sample uni-axially and the sample separates from the rings before edge release waves reach it. This technique commonly referred to as momentum trapping [10], has proven effective in preserving uni-axial loading/unloading in numerous recovery and non-recovery experiments [11-14]. Finite difference calculations by Stevens and Jones [15] demonstrated that if the momentum trapping rings are not properly designed, the plastic work on the sample from radial release waves can be up to a factor of ten higher than that resulting from uni-axial loading/unloading only. Furthermore, a diameter to thickness ratio of greater than 7 to 1 is needed to reduce the radial release effects to acceptably low levels. In the review by Gray [10] a simple, centered flow condition calculation is used to determine the approximate minimum width for the momentum trapping rings.

Full and incipient spall experiments were conducted on as–received and as-annealed materials in 2007, 2008, and 2011. A PDV diagnostic was utilized in the 2008 experiments. This requires an image intensity extraction routine to be utilized to obtain particle velocity versus time data. All other experiments used VISAR, which yields particle velocity versus time data directly. Table I lists the relevant experimental parameters. The middle two numbers in the shot number designation represents the year, in which the experiments were conducted, i.e.: 56-08-15 occurred in 2008. It should be noted that P is peak shock stress of the experiments. Representative PDV and VISAR data for both incipient and full spall experiments conducted on fully annealed and as-received, cold rolled DU are given in Figs. 1-4.

The common means of determining spall strength from the magnitude Δu_{fs} of the velocity drop at the free surface of the specimen (as measured by VISAR) makes use of the assumptions that Δu_{fs} is exactly twice the corresponding change of the in-material particle velocity, Δu_p, and that the acoustic approximation is valid, so that the tensile stress at the spall plane is given by

$$\sigma^* = \frac{1}{2}\rho c \Delta u_{fs} \tag{1}$$

The further assumption that is normally made is that the density and sound speed at the time and location of fracture are sufficiently close to the original values in the unperturbed material, ρ_0 and c_0, (i.e., that heating and damage are negligible). With this assumption, these values may be substituted into eq. 1 to give

$$\sigma^* = \frac{1}{2}\rho_0 c_0 \Delta u_{fs} \tag{2}$$

It should be noted that, as normally used, the quantity Δu_{fs} is the magnitude of the velocity drop and is a positive, definite number. Since fracture is by definition an inelastic process, we can presume that the material has yielded plastically prior to fracture, so that the appropriate sound speed to use is the bulk sound speed c_b. This ignores the fact that the plastic rarefaction fans that interact to produce tensile stresses leading to spall are preceded by elastic waves, so there is a non-hydrostatic stress field that this treatment ignores. The most accurate measurement of the spall strength should take this into account and replace eq. (1) with a sum of the stresses due to the elastic and plastic parts of the release.

There is a further shortcoming in above practice in that the spall fracture occurs when the material is in tension. When the fracture occurs, stress at the spall plane drops to zero and the material, which has been in a tensile stress state, recovers the elastic portion of the tensile strain, launching a compressive elastic spall pulse with the magnitude of the material strength in the region of spall, along with a plastic pulse equal to the stress relaxation above the material yield strength, which lags behind. The leading part of the spall pulse, being an elastic wave, travels at the longitudinal wave speed c_l and overtakes the trailing edge of the release fan. This compressive elastic wave mutually annihilates with the portion of the tensile release fan that it encounters and so reduces the value of Δu_{fs} by the extent to which the rarefaction fan was overtaken. The so-called Romanchenko correction, as presented by Antoun et al. [1998], introduces a correction factor to help compensate for this effect. Unfortunately, this correction factor is derived for brittle materials failing under Taylor-wave loading and should not be applied to these data.

Table I: Plate impact experimental details

Experiment	u_D (km/s)	U_s (km/s)	+/- U_s	u_p (km/s)	+/-u_p	ρ (gm/cm^3)	+/-ρ	P (GPa)	+/-P	Δu_{fs} (km/s)	Spall strength (GPa)
56-07-22*	0.715	2.75	0.018	0.331	0.001	21.58	0.03	17.69	0.06	0.098	2.25
56-07-23*	0.608	2.719	0.010	0.282	0.001	21.17	0.02	14.96	0.03	0.094	2.20
56-07-24*	0.482	---	---	---	---	---	---	---	---	0.086	2.02
56-07-25*	0.558	2.681	0.010	0.260	0.001			13.64	0.02	0.088	2.06
56-08-15	0.183	2.62	0.02	0.086	0.001	19.83	0.10	4.34	0.019	---	No spall
56-08-16	0.287	2.20	0.016	0.145	0.001	20.46	0.10	6.43	0.028	0.06	1.40
56-08-23	0.270	2.22	0.016	0.136	0.001	20.37	0.10	6.06	0.026	0.062	1.45
56-11-33	0.285	---	---	---	---	---	---	~6.43	---	0.065	1.52
56-11-34	0.287	---	---	---	---	---	---	~6.43	---	0.065	1.52
56-11-38*	0.439	---	---	---	---	---	---	~10.57	---	0.069	1.62
56-11-46*	0.433	---	---	---	---	---	---	~10.42	---	0.064	1.50

* indicates full spall

Shock Experiments (Direct Explosive Drive)

In addition to plate impact experiments, as-annealed DU was shock loaded with direct high explosive (HE) drive. Specimens were loaded with a P56 plane wave lens. This means the HE was 9501. While there was no drive measurement, VISAR data was collected during the dynamic loading. This data is given to Fig. 5 and compared to data obtained by loading U6Nb in similar configuration. Samples were then soft recovered for post mortem metallographic analysis.

Post Mortem Characterization:

All specimens were soft recovered and therefore subject to post mortem characterization through both optical and scanning electron microscopy. Macroscopic images of cross-sectioned, plate impact specimens reveal that damage evolution is sensitive to the drive condition. For example in Fig. 6, as-received DU subjected to 4.3 (56-08-15), 6.06 (56-08-23), and 6.43(56-08-16) GPa peak stress states results in the following volume fractions of damage, respectively: 0, 0.97% and 0.45%. Additionally, higher resolution metallography did not reveal significant differences in the failure response of the as-annealed and the as-received DU. In both cases, failure occurs at grain boundaries, Figs. 7-8, leading to a fracture surface in the fully-spalled specimens that is typical of intergranular fracture, Fig. 9. It is interesting to note that this is similar to the type of failure observed in notched tensile DU specimens pulled quasi-statically in uni-axial stress conditions. The notched tensiles impart a high triaxiality stress state, just as in the plate impact experiments and the ultimate failure mechanism, independent of rate, is observed to be sensitive to that. Finally, in both materials, adiabatic shear banding appears to be the mechanism linking non-coplanar set of intergranular cracks in both the as-received and as-annealed materials, as is shown in Fig. 10.

It is recognized that DU accommodates plastic strain during shock loading through a combination of slip and twinning [16]. Optical images in Figs. 7 and 8 show some obvious areas of twin formation in the specimens examined in this study. High-resolution, electron back-scattered diffraction (EBSD), shown in Fig. 11, revealed that this twinning was significant through out the thickness of the deformed specimens and that often times multiple twin variants were activated within a grain. The bent or curvy nature of many of the twin laths also appears to indicate that twinning was likely activated early in the shock process and then once twins were formed they were deformed by subsequent slip and shear.

In contrast to the plate impact specimens, was the post mortem microstructure of the explosively driven DU specimens. While failure still seemed to be related to the formation of cracks in the region of peak tension, the microstructure surrounding these cracks had been significantly coarsened, as is observed in Fig. 12. Significant adiabatic heating in the neighborhoods local to the regions of damage is assumed to significantly coarsen the microstructure, but this process is thought to happen after loading and damage events have been completed. Since the heating is assumed to modify the microstructure late in time, it is difficult to draw conclusions about the linkage between microstructure and damage evolution in these explosively driven shots.

Conclusions:

Two overarching conclusions can be drawn from this study. The first is that while drive condition has a subtle affect on continuum level response like spall strength (spall strength varies from 1.4 to 2.25GPa for a peak stress drive condition from 6.1 to 17.7 GPa), it does affect the details of the damage evolution. In the plate impact experiments, volume fraction of damage was highly sensitive to small changes in drive condition (no damage observed for a drive condition with a peak stress of 4.1GPa where as obvious incipient damage is observed by 6.1GPa). Additionally, while the HE drive condition resulted in very similar failure characteristics, it seems to have undergone a very different adiabatic heating history. The second conclusion to be drawn is that the damage mechanisms are insensitive to annealing this high purity material. This can be seen as both the as-annealed and the as-received material appear to fail through a combination of void nucleation and coalescence at grain boundaries and adiabatic shear banding and display rather similar spall strengths. This suggests that the triaxiality of the stress state produced by the drive condition may have more a more significant role in damage in failure than subtle microstructural changes in this material. Future work should focus on characterization of the features of grain boundaries to understand why they promote failure and to understand if certain boundaries are more prone to failure than others.

References:

[1] T. Antoun, L. Seaman, D. Curran, G. Kanel, S. Razorenov, A. Utkin, Spall Fracture, Springer (2002) pg 26.

[2] L.M. Barker and R.E. Hollenbach, J.A.P., **43**, 4669 (1972).

[3] W.F. Hemsing, *Review of Scientific Intruments*, 50 pp 73-78 (1979).

[4] R.S. Hixson, G.T. Gray III, P.A. Rigg, L.B. Addessio and C.A. Yablinsky, Shock Compression of Condensed Matter, 2003, edited by M.D. Furnish, Y.M. Gupta, and J.W. Forbes, pg 469.

[5] Zurek, A.K., Embury, J.D., Kelly, A., Thissell, W.R., Gustavsen, R.L., Vorthman, J.E., Hixson, R.S., in Shock Compression of Condensed Matter, AIP, (1991).

[6] S. Cochran and D. Banner, J. Appl. Phys, Vol 48, No. 7, (1977).

[7] Jim Johnson 1981

[8] G.T. Gray III, Influence of Shock-Wave Deformation on the Structure/Property Behavior of Materials, in *High Pressure Shock Compression of Solids*, (edited by J.R. Asay and M. Shahinpoor), Springer-Verlag, New York, 1993, 187 pp.

[9] E.G. Zukas, *Metals Engineering Quarterly*, 6 (10660, 16.

[10] D.G. Doran and R.K. Linde, *Solid State Physics*, 19 (1966), 229.

[11] R.N. Orava and R.H. Wittman, Techniques for the Control and Application of Explosive Shock Waves, in *Proceedings of the 5th International Conference on High Energy Fabrication*, University of Denver, Denver, 1975, p.1.

[12] P.S. Decarli and M.A. Meyers, Design of Uni-axial Strain Shock Recovery Experiments, in *Shock Waves and High Strain Rate Phenomena in Metals*, (edited by M.A. Meyers and L.E. Murr), Plenum, New York, 1981, 341 pp.

[13] A.L. Stevens and O.E. Jones, *Journal of Applied Mechanics*, **39** (1972), 359.

[14] O. T. Strand, et. al., Rev. Sci. Instrum. **77**, 083108 (2006)

[15] D. Shechtman, *Metallurgical Transactions A*, 7A, pp. 151-152 (1976).

[16] D.D. Koller, E.K. Cerreta, and G.T. Gray III, in DYMAT 2009, vol. 2,pp. 1061-1067 (2009).

Figures:

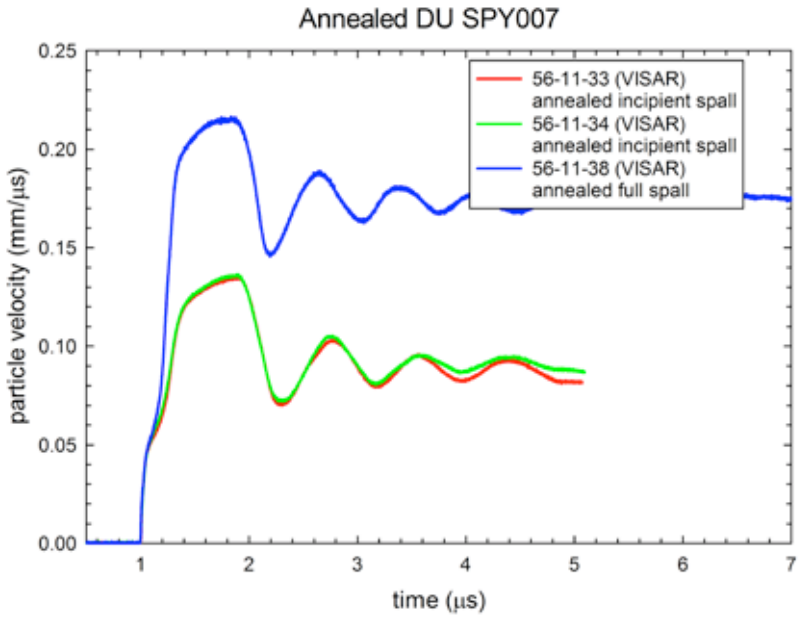

Figure 1: Three experiments conducted on annealed DU SPY007. Excellent agreement in the HEL and spall strength is observed.

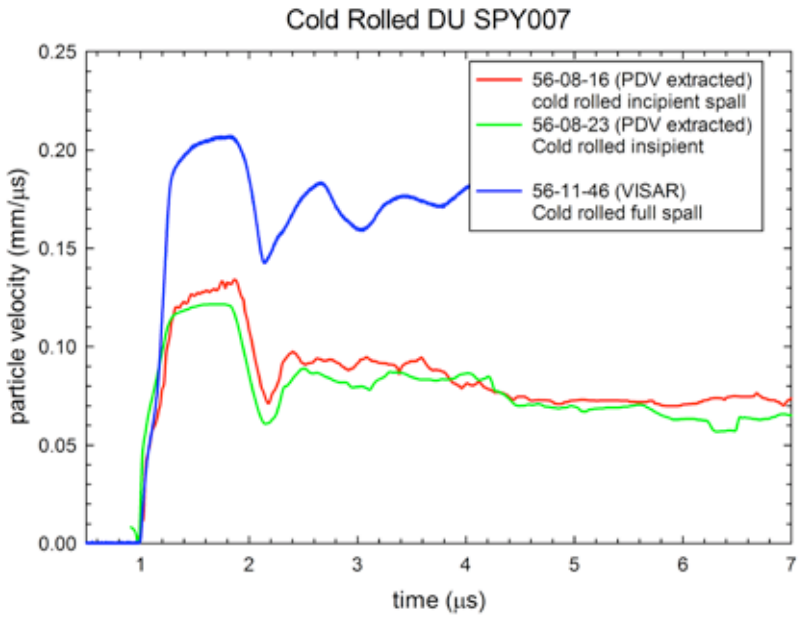

Figure 2: Three experiments conducted on DU SPY007 in the as-received condition (no post annealing). Good agreement in the HEL is still observed. The differences in the peak state and structure are attributable to PDV image extraction routines. However, this does not result in significant differences in calculated spall strength.

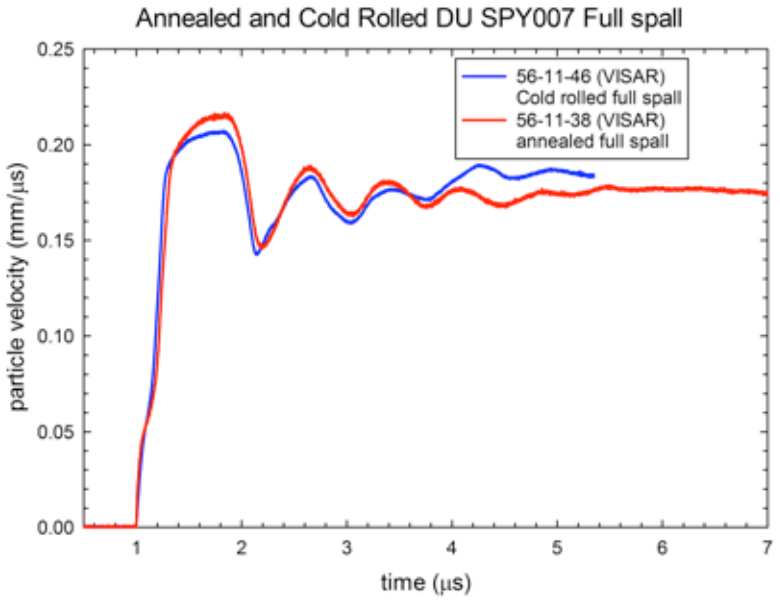

Figure 3: Comparison of annealed and as received, cold rolled microstructures shows no significant differences in the dynamic response. Good agreement in the HEL as well as in the calculated spall strength is observed. Differences in the VISAR are due to small differences in experimental geometry.

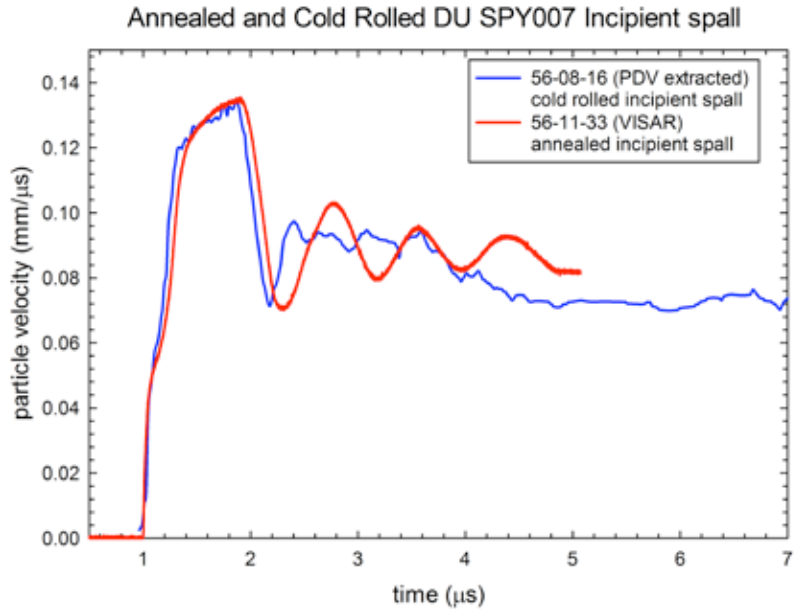

Figure 4: Comparison of annealed and as-received, cold rolled microstructures shows no significant differences in the dynamic response. Good agreement in the HEL as well as in the calculated spall strength is observed. Differences in the VISAR and extracted PDV are attributable to PDV image extraction routines and small differences in experimental geometry.

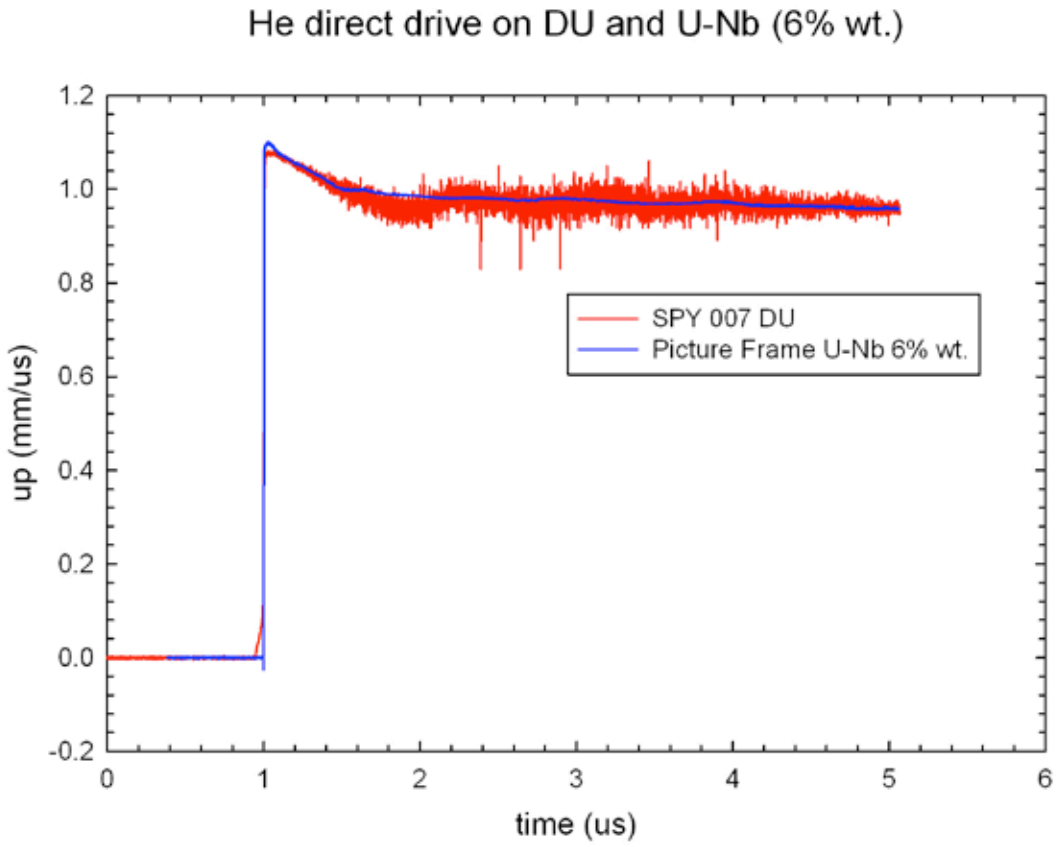

Figure 5: VISAR data from direct HE drive experiments conducted on DU and U6Nb loaded in similar configurations.

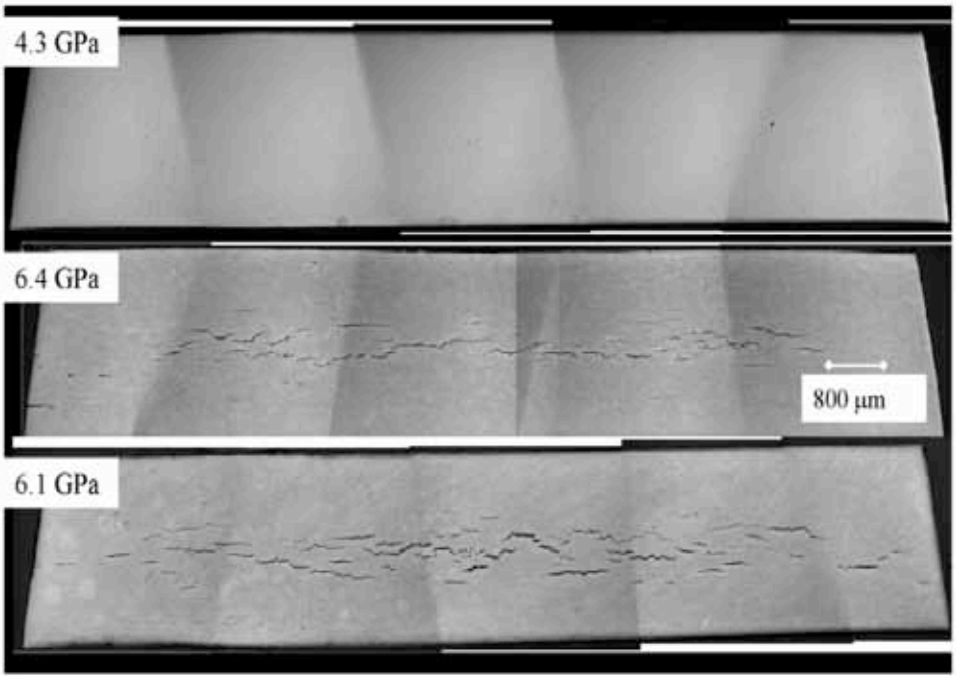

Figure 6: Optical metallography of the full cross section of as-rolled DU that has been incipiently spalled. 4.3GPa corresponds to shot 56-08-15, 6.1GPa corresponds to shot 56-08-23, and 6.4GPa corresponds to shot 56-08-16.

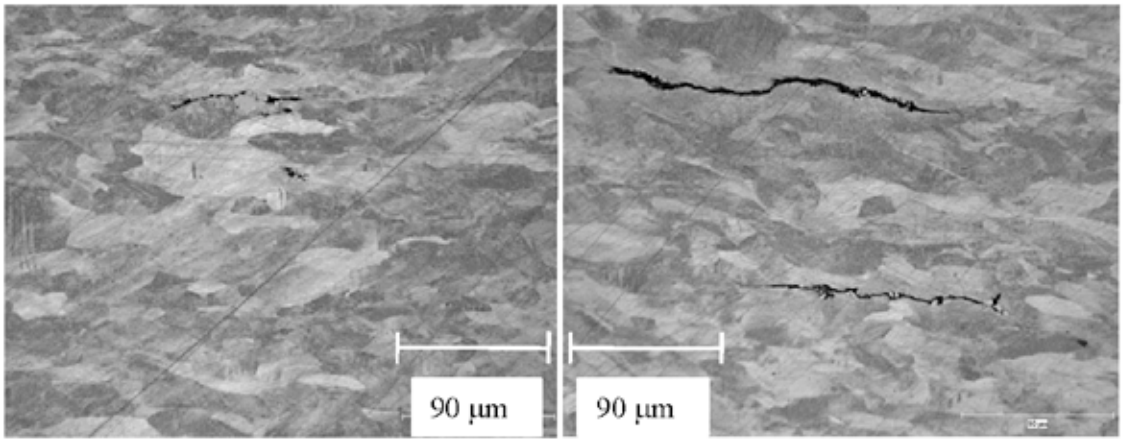

Figure 7: Optical metallography showing that incipient damage in the as-rolled DU, shot number 56-08-23, is primarily associated with cracking at grain boundaries and sometimes inclusions.

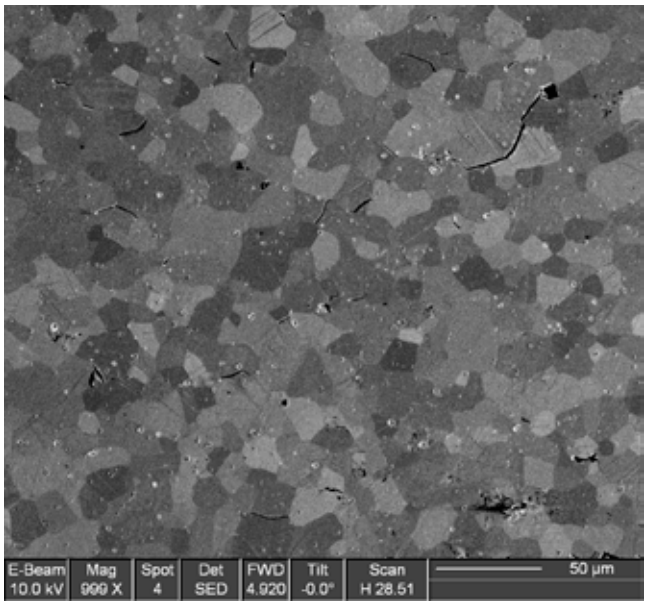

Figure 8: Scanning electron microscopy (SEM) image of the incipient damage in the as-annealed DU, shot number 56-11-34. Cracking along grain boundaries and at inclusions is apparent.

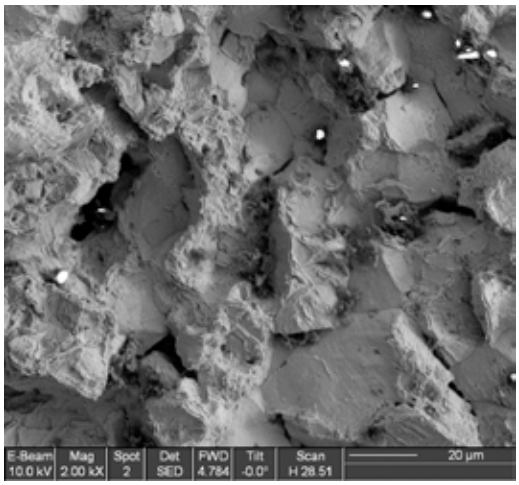

Figure 9: SEM image of the fracture surface in the fully spalled 56-11-38.

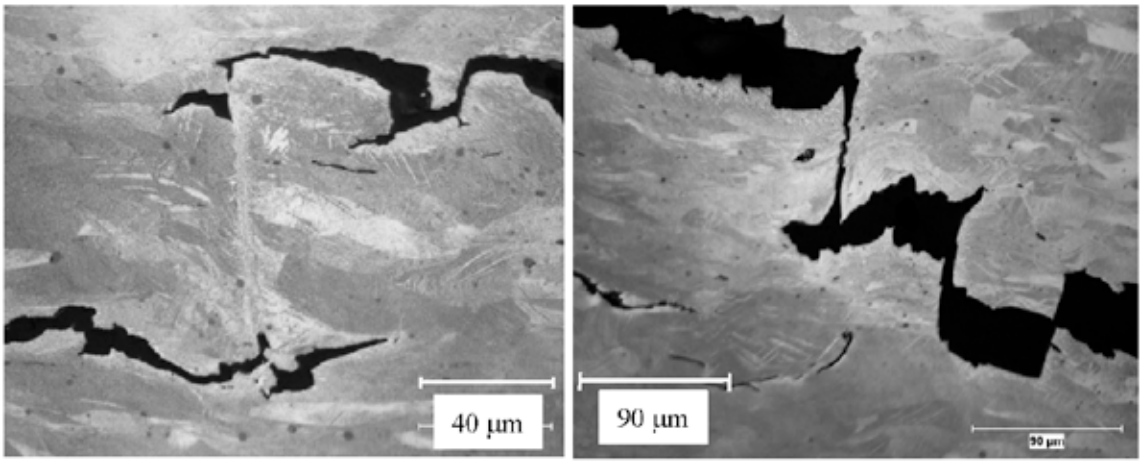

Figure 10: Adiabatic shear banding and cracking through previous adiabatic shear bands that links up intergranular cracks in the as-rolled DU shot 56-08-23.

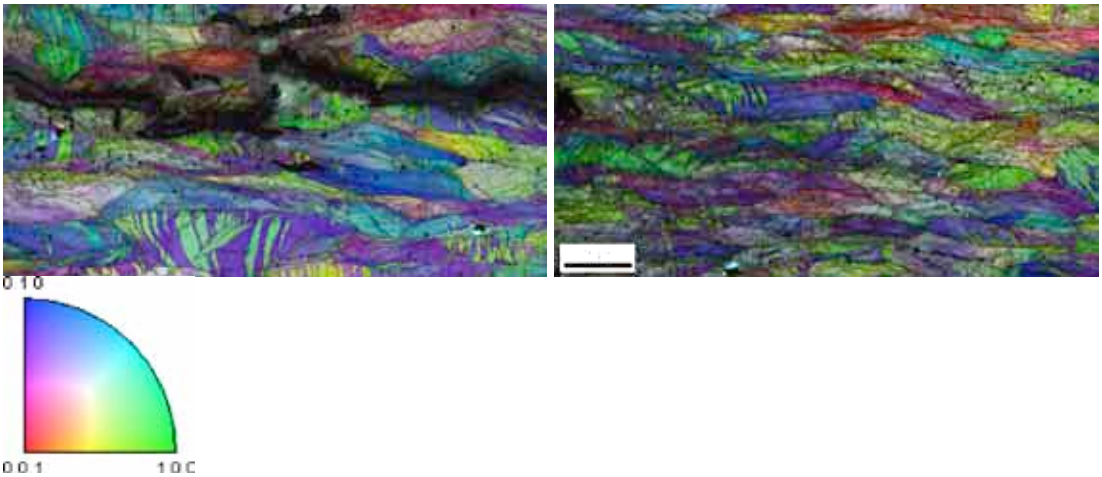

Figure 11: EBSD images showing details of twinning and damage in the incipiently spalled, as-rolled DU.

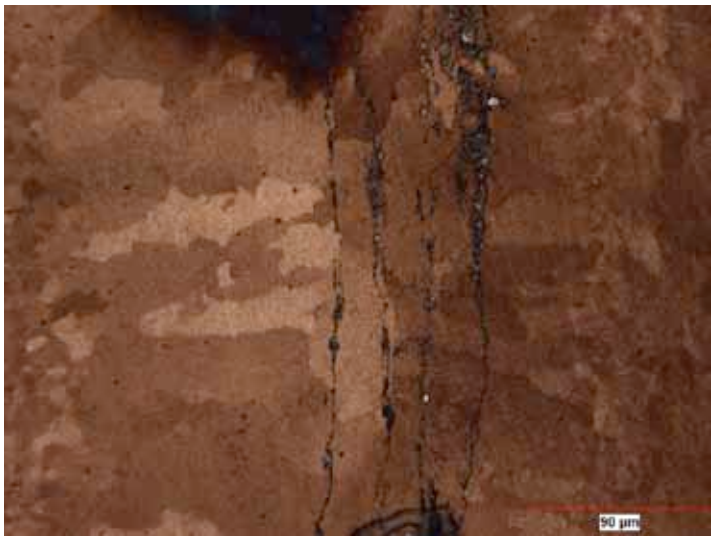

Figure 12: Optical image of spall plane in the HE driven as-annealed DU specimen. Note significant grain coarsening in the region of the spall plane, which runs vertically rather than horizontally in this image.

Appendix 2: Low Pressure Equation of State Data for DU

In support of the planned detailed spallation studies on DU, a series of low peak pressure EOS experiments were conducted by WX-9 (Darcie Koller) on annealed SPY007 plate material to augment the Marsh EOS compendium. These experiments were conducted to provide the basis for a more refined EOS for DU at low peak pressures. The experimental procedures and the results of all these tests were detailed in the 2007 APS Topical Conference listed for reference. Table I presents the detailed specifications of the low-pressure EOS shots conducted.

Table I: Recent low pressure DU Hugoniot data. The measured HEL for the DU studied was 1.4 GPa, for material possessing an initial density, ρ_0= 19.03 g/cm^3, C_0= 2.46 mm/μs, and s=1.569.

Shot	C_L mm/μs	C_s mm/μs	ρ_0 g/cm^3	ρ_1 g/cm^3	P_2 GPa	U_{s2} mm/μs	U_{p2} mm/μs	ρ_2 g/cm^3
56-06-37	3.426	2.089	19.0396	19.1516	9.7563	2.7372	0.1808	20.34
56-07-01	3.499	2.164	19.055	19.1422	2.7605	2.5519	0.0481	19.4122
56-07-02	3.503	2.162	19.06	19.1767	4.0208	2.6527	0.0729	19.5594
56-07-14	3.497	2.15	18.954	19.0703	15.1826	2.894	0.2712	20.8748
56-07-15	3.500	2.15	19.028	19.1446	12.5288	2.8165	0.2278	20.6615

Comparison of this data from WX-9 (Darcie Koller) in comparison to the Marsh Compendium is presented in Figures 1 and 2. Consistent with the indications of a Bauschinger contribution to the shock-loading response of DU, as detailed and discussed in Section 5, the wave profiles for the DU a quasi-elastic release wave shape instead of a classic elastic-plastic "notch" on release from the Hugoniot stress and are discussed in the APS Conference reference cited. A plot of the low-pressure wave profiles is presented in Figure 3.

Reference:

D.D. Koller, G.T. Gray III, and R.S. Hixson:
Shock Compression of Condensed Matter-2007, (2007) AIP Conference Proceedings 955, Melville, N.Y., edited by M. Elert, M.D. Furnish, R. Chau, N. Holmes, J. Nguyen, ISBN 978-0-7354-0469-4, pp. 553-556.
"Shock Wave Profile and Bauschinger Effect in Depleted Uranium"

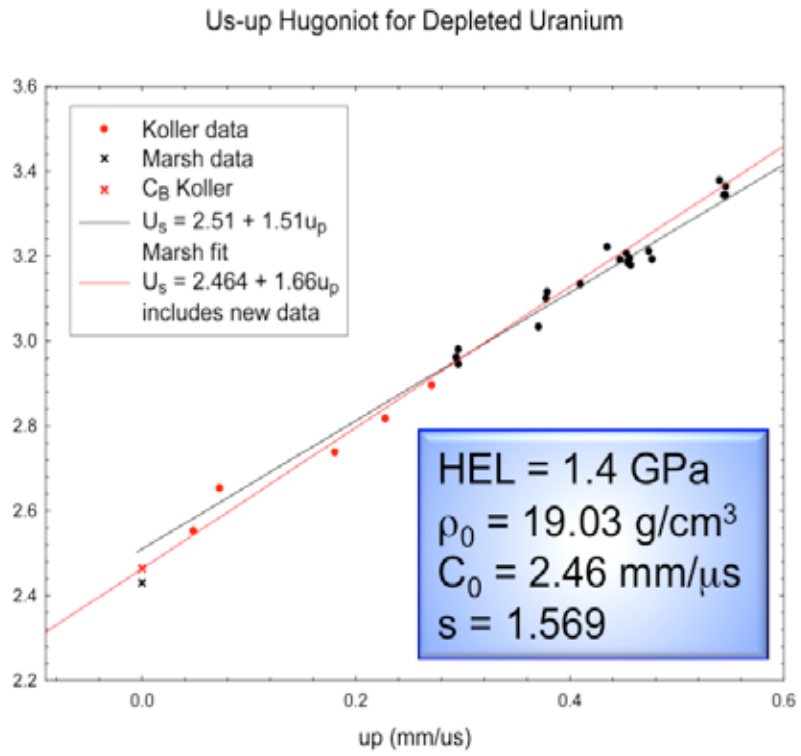

Figure 1: Plot of U_s – U_p Hugoniot Data for Depleted Uranium; Marsh Compendium and the new Koller Data and U_s fitting.

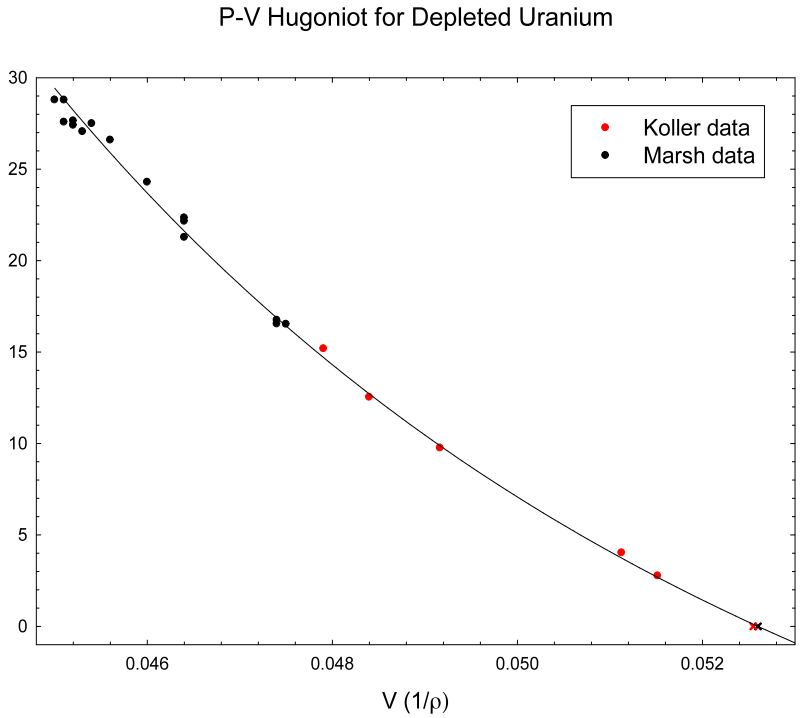

Figure 2: Plot of P – V Hugoniot Data for Depleted Uranium

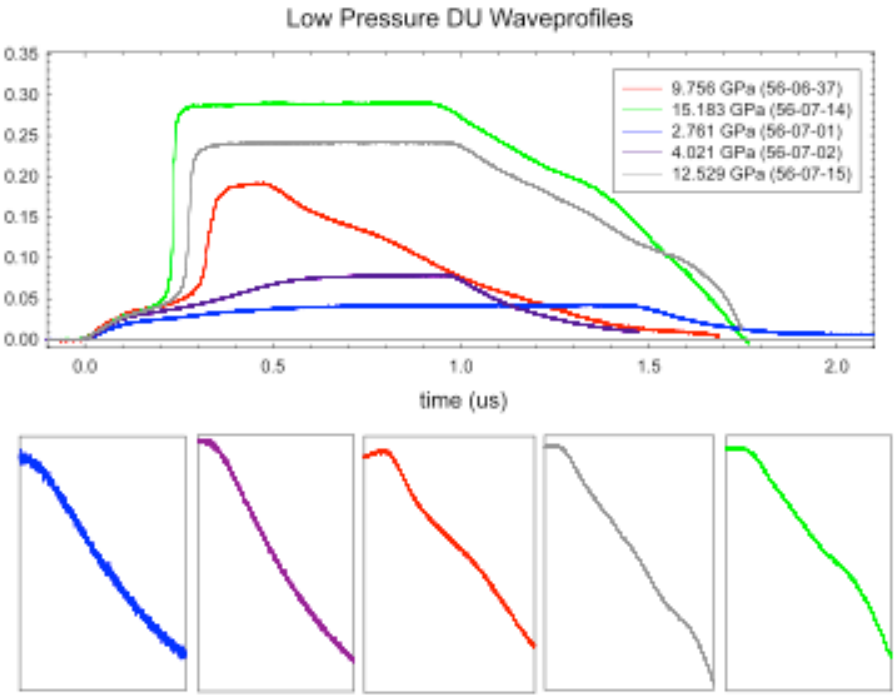

Figure 3: VISAR wave profiles from low pressure DU Hugoniot experiments showing non-ideal quasi-elastic release wave shapes consistent with a Bauschinger effect operative in DU.

Section 7: Dynamic Sphere Extrusion Response of DU as a Function of Temperature

Experimental:

Dynamic Extrusion Test:

DU bullets with approximate dimensions are shown in Fig. 1a were machined from plate at the machine shop in MST-6. The specimens were machined with the long axis of the bullet perpendicular to the normal of the plate for the DU bullet samples.

The schematic of the experimental set-up is shown in Fig. 1b. Dynamic tensile extrusion tests were conducted in a modified 7.62 mm diameter Taylor cylinder facility in MST-8 [1]. Bullets were accelerated in an He-gas launcher at speeds in the 300-600m/s range and temperatures of 25-250°C, into a high strength steel extrusion die (A2 or S7 tool steel with a Rockwell Hardness of 56 and 54, respectively) designed with an entrance diameter of 7.62mm and an exit diameter of 2.79mm (area reduction of 63%). In all cases tested here, some portion of each specimen was not fully extruded and remained in the die. Fully extruded pieces were soft recovered. The in-situ extrusion process was captured using high speed photography [1,2]. All recovered pieces from each shot were weighed and compared to the starting bullet weight to ensure no segments were lost during recovery.

Characterization:

Post mortem characterization of recovered specimens consisted of optical metallography (OM) and scanning electron microscopy (SEM). SEM was performed on as-recovered segments of the DU using an FEI Inspect SEM. OM was performed on cross-sectioned specimens ground to an 800grit finish and then electro-polished and etched.

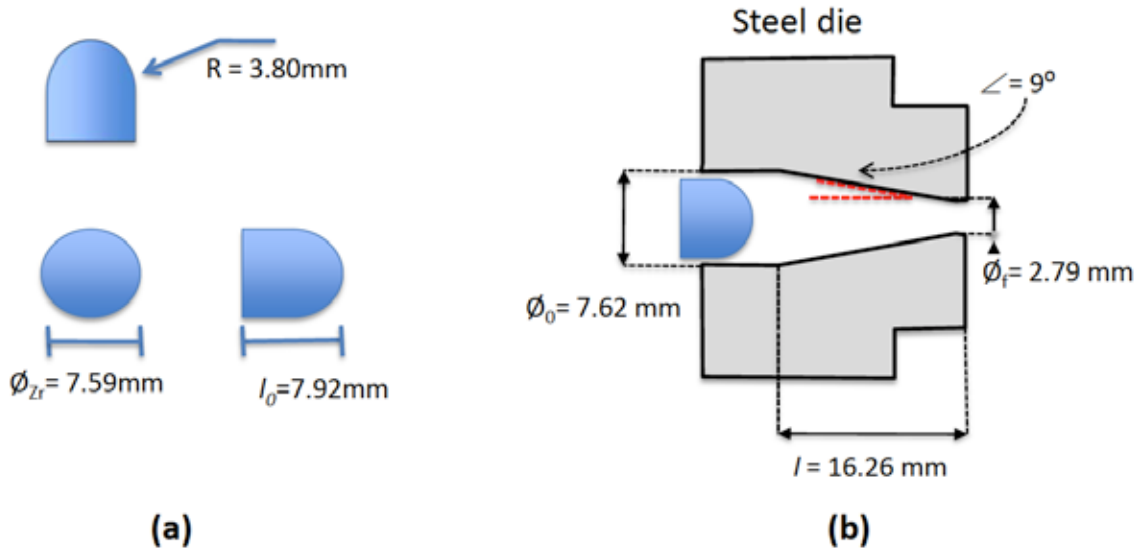

Figure 5.1: (a) Geometry of the DU bullets and (b) geometry of the extrusion die

DU Dynamic Tensile Extrusion Results:

<u>High-Speed Photography:</u>

Representative high-speed photography results of six different experiments are shown in Fig. 2. In particular, Fig. 2a and b show DU baseline material fired at a velocity of approximately 470m/s at 25°C. From these images it is apparent, that unlike previous experiments on Ta and Cu [1,2], the extrusion process in these experiments is dominated by shear failure occurring following modest plastic straining. Arrows in these images highlight these specific failures. This failure process produced fragments that were soft recovered but difficult to reassemble in extrusion order, therefore final extrusion lengths were not measured for these specimens.

In Figs. 2b, the role of temperature on the shear failure process is shown. DU exhibited an increase in overall plastic straining at elevated temperatures but fracture remained dominated by shear damage processes as shown in Fig. 2b.

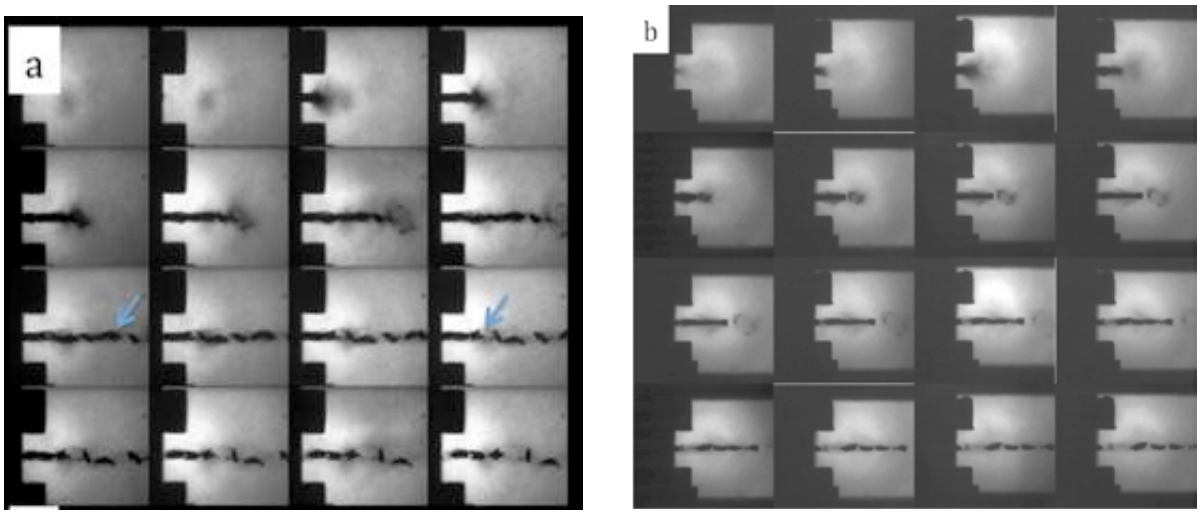

Figure 2: (a) DU at 25°C and 470m/s, (b) DU at 200°C and 425m/s

Optical Metallography:

To identify the cause for the difference in extrusion responses of the DU, optical metallography was performed on select specimens. Specifically, the gradient in deformation in the pieces caught in the die were of interest. Multiple regions were seen in the recovered fragments that can be described as follows: region 1 contains undeformed grains, region 2 has elongated grains, region 3 contains elongated and twinned grains, region 4 has severely elongated and twinned grains, and region 5 is so heavily worked that the microstructure is difficult to resolve. This gradient in deformation is likely evidence of the difference in the role of shear as a function of radial distance from the outer edge to the centerline of the specimen. Near the outer edge, the microstructure is sheared against the die and more severely deformed than material some radial distance toward the centerline.

Some of the DU specimens displayed significant recrystallization adjacent to the fracture surfaces. In Fig. 3, a representative microstructure is given showing the recrystallization microstructure very near the fracture surface in one fracment. This recrystallization suggests significant temperature rise due to less work dissipated through plastic processes such as slip as well as the low thermal conductivity in DU. Elevated temperatures due to shear banding are believed to have led to the formation of the larger recrystallized grains.

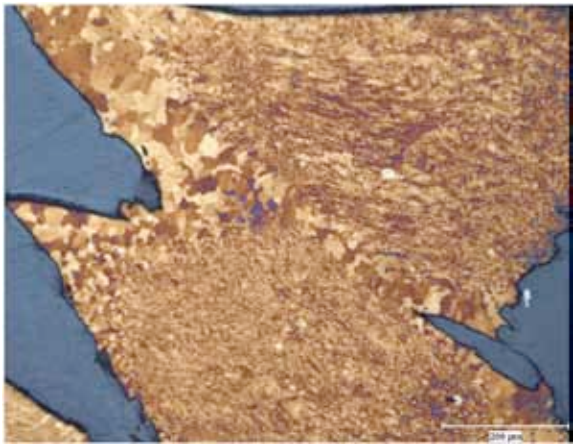

Figure 3: DU tested at 541m/s and 25°C showing significant recrystallization in regions of failed and incipient shear bands

Discussion:

Both high-speed photography and SEM characterization reveal that there is a change in deformation and failure process for DU as a function of temperature during dynamic extrusion. Shear failure dominates the lower temperature extrusion processes and tensile necking, which terminates in fracture, dominates the high temperature responses. Interestingly, the difference in specimens displaying these two types of behavior is the development of an elongated but not heavily twinned microstructure.

Furthermore, for specimens that lack a region 2 microstructure, deformation was dominated by twinning and these same specimens had an extrusion response dominated by shear failure. This suggests that twinning, which can reduce effective glide distances for slip, promotes localization of plastic flow, adiabatic shear band formation, and subsequently shear-dominated failures during dynamic extrusion. The observation of more incipient shear bands in specimens lacking a region 2 microstructure, further supports this notion.

For conditions examined in this study, the activation of enhanced slip, and therefore significantly increased plasticity, was not observed for DU. Clearly 200°C was seen to significantly increase the dynamic ductility in Ta. Further testing of Ta at yet higher temperatures as well as post-mortem microstructural examination will be conducted to elucidate the deformation and damage mechanisms responsible for this behavior. In addition, finite-element-modeling (FEM) of some of the Ta extrusion experiments will be pursued.

Conclusions:

DU dynamic extrusion experiments revealed that while in all cases these materials failed in a ductile manner under the combined shock, shear, tensile loading conditions of extrusion, the manner in which the material failed was sensitive to processing and testing temperature. For the temperatures examined in this study (25-250°C), a transition between twin-dominated and enhanced-slip deformation, was not observed in DU.

References:

1. Gray, G.T., et al. *Influence of Shock Prestraining and Grain Size on Dynamic Tensile Extrusion Response of Copper: Experiments and Simulation*. in *Shock Compression of Condensed Matter* 2005. Baltimore, MD: AIP.
2. Cao, F., et al., *Dynamic Tensile Extrusion of Tantalum.* Acta Materialia, 2008. **56**: p. 5804-5817.

Section 8: Constitutive Modeling of Annealed and Shock Prestrained DU and Model Validation using Taylor Cylinder Testing and Finite-Element Simulations

Constitutive Modeling

Nomenclature:

σ: flow stress

ε: true plastic strain

$\dot{\varepsilon}$: true plastic strain rate

κ: a constant that modifies Voce hardening law

$\hat{\theta}_0$: initial normalized strain hardening rate $\left(d\hat{\sigma}_\varepsilon / d\varepsilon\right)_{\varepsilon=0}$

$\hat{\sigma}$: mechanical threshold strength, the flow stress of material without the assistance of thermal activation at zero Kelvin

A_0, A_1, A_2, A_3 : constants in an empirical relation describing strain-rate-dependent of $\hat{\theta}_0$

$\hat{\sigma}_i$: maximum mechanical threshold of yield strength without the assistance of thermal activation at zero Kelvin

p: a constant describing the shape of the top of a glide resistance profile $\left(\sigma \approx \hat{\sigma}\right)$

q: a constant describing the shape of the tail of a glide resistance profile $\left(\sigma \approx 0\right)$

g_{0i}, $g_{0\varepsilon}$, g_{0sS} : normalized total activation energy related to yield stress, structure evolution during deformation, and the saturation stress respectively

b: Burgers vector of a dislocation

k: Boltzmann constant

T: temperature in Kelvin

ρ: density

μ: shear modulus

μ_o: shear modulus at 0K

D_0, T_0 : constants describing temperature-dependent of shear modulus

C_p: heat capacity

C_{p0}, C_{p1}, C_{p2} :: constants describing temperature-dependent of heat capacity

Ψ: percent of work converted into heat under adiabatic deformation condition

Description of the Mechanical Threshold Strength (MTS) model:

The frame work and detailed description of the mechanical threshold stress (MTS) model is given elsewhere[1-5]. A summary of the MTS model is presented here to provide an overview and map all equations used in the model with physical constants. Plastic deformation is known to be controlled by the thermally activated interactions of dislocations with obstacles. In the MTS model the current structure of a material is represented by an internal state variable, the mechanical threshold ($\hat{\sigma}$)[6], which is defined as the flow stress at 0K. The mechanical threshold is separated into athermal and thermal components,

$$\hat{\sigma} = \hat{\sigma}_a + \sum \hat{\sigma}_t, \tag{1}$$

where the athermal component $\hat{\sigma}_a$ characterizes the rate independent interactions of dislocations with long-range barriers such as grain boundaries, dispersoids, or second phases. The thermal component $\hat{\sigma}_t$ characterizes the rate dependent interactions of dislocations with short range obstacles (forest dislocations, interstitial, solutes, Peierls barrier, etc.) that can be overcome with the assistance of thermal activation. The summation of the contributions from different obstacles doesn't need to be linear[2]. The flow stress of a constant structure at a given deformation condition can be expressed in terms of the mechanical threshold as:

$$\frac{\sigma}{\mu} = \frac{\sigma_a}{\mu} + \sum \frac{\sigma_t}{\mu} = \frac{\sigma_a}{\mu} + \sum S(\dot{\varepsilon}, T)\frac{\hat{\sigma}_t}{\mu_0}, \tag{2}$$

where the athermal component is a function of temperature only through the shear modulus, and the factor *S* specifies the ratio between the applied stress and the mechanical threshold stress. This factor is smaller than 1 for thermally activated controlled glide because the contribution of the thermal activation energy reduces the stress required to force a dislocation past an obstacle.

For simplicity, an empirical equation[7] was used to fit the data to incorporate the temperature dependence of "μ" in the form of:

$$\mu = \mu_0 - \frac{D}{\exp\left(\frac{T_0}{T}\right) - 1} \tag{3}$$

where μ_0, D and T_0 are fitting constants.

In the thermally activated glide regime the interaction kinetics for short range obstacles are described by an Arrhenius expression of the form:

$$\dot{\varepsilon} = \dot{\varepsilon}_0 \exp\left(\frac{-\Delta G}{kT}\right). \tag{4}$$

The free energy (ΔG) is a function of stress and a phenomenological relation was chosen[6]:

$$\Delta G = g_0 \mu b^3 \left[1 - \left(\frac{\sigma_t / \mu}{\hat{\sigma}_t / \mu_0} \right)^p \right]^q . \tag{5}$$

g_0 in units of μb^3 is the normalized activation energy for the dislocations to overcome the obstacles. It is also an indication of the sensitivity of overcoming this obstacle to changes in temperature and strain rate. p and q are parameters with the ranges $0<p\leq 1$ and $1\leq q\leq 2$. They detail the glide resistance profile in the higher and lower activation energy regions, respectively[27]. Upon rearrangement, we have the following relation between the applied stress (σ_t) and the mechanical threshold stress ($\hat{\sigma}_t$) at a constant structure:

$$\frac{\sigma_t}{\mu} = \left[1 - \left(\frac{kT}{g_0 \mu b^3} \ln \frac{\dot{\varepsilon}_0}{\dot{\varepsilon}} \right)^{1/q} \right]^{1/p} \cdot \frac{\hat{\sigma}_t}{\mu_0} . \tag{6}$$

For single-phase materials with cubic crystal structures, the thermal component (σ_t) consists of the linear summation of a term describing the thermal portion of the yield stress ($\sigma_i = \sigma_y - \sigma_a$) and a term describing the evolution of the dislocation structure σ_ε as a function of temperature, strain rate and strain. Equation (2) can be written as:

$$\frac{\sigma}{\mu} = \frac{\sigma_a}{\mu} + \frac{\sigma_i}{\mu} + \frac{\sigma_\varepsilon}{\mu} = \frac{\sigma_a}{\mu} + S_i(\dot{\varepsilon}, T) \frac{\hat{\sigma}_i}{\mu_0} + S_\varepsilon(\dot{\varepsilon}, T) \frac{\hat{\sigma}_\varepsilon}{\mu_0} . \tag{7}$$

The second term on the right hand side of the equation describes the rate dependent portion of the yield stress mainly due to intrinsic barriers such as the strong Peierls stress in bcc materials at low temperatures or at high strain rates. It is further assumed that this term doesn't evolve after yielding. The mechanical threshold, $\hat{\sigma}_\varepsilon$ in equation (7), evolves with strain due to dislocation accumulation (work hardening) and annihilation (recovery). This structure evolution $\hat{\theta} = d\hat{\sigma}_\varepsilon / d\varepsilon$ is written[8]:

$$\hat{\theta} = \hat{\theta}_0 - \hat{\theta}_r(T, \dot{\varepsilon}, \hat{\sigma}_\varepsilon) , \tag{8}$$

where $\hat{\theta}_0$ is the hardening due to dislocation accumulation and $\hat{\theta}_r$ is the dynamic recovery rate. The physical understanding of the work hardening behavior of polycrystals is still inadequate to unify this complex process and represent it entirely by physically-based parameters. A simple form that was based on Voce law with modification to capture mechanical response at large strains was found to provide a robust fit to hardening behavior in most metals when dynamic recovery is the controlling deformation mechanism:

$$\hat{\theta} = \hat{\theta}_0 \left(1 - \frac{\hat{\sigma}_\varepsilon}{\kappa \cdot \hat{\sigma}_v(\dot{\varepsilon}, T)}\right)^\kappa = \hat{\theta}_0 \left(1 - \frac{\hat{\sigma}_\varepsilon}{\hat{\sigma}_{\varepsilon s}(\dot{\varepsilon}, T)}\right)^\kappa \tag{9}$$

where κ approaching one represents a linear variation of strain hardening rate with stress (Voce law). The saturation threshold stress ($\hat{\sigma}_{\varepsilon s} = \kappa \cdot \hat{\sigma}_v$, $\hat{\sigma}_v$ is the saturation stress when Voce law holds) is a function of temperature and strain rate. The concept of saturation is a limiting factor in this model. The material may or may not reach saturation within the strain range of interest. The constant κ describes the degree of deviation from the Voce law, it is found that a fitted value of 1, 1.5, 2, 2.5, or 3 captures the hardening behavior of most materials reasonably well. There is no benefit of using for example 1.665 or 2.789 for κ since the strain hardening plot, which is a first-order differential curve of the stress/strain data, is very noisy in general, therefore the determination of κ as well as $\hat{\theta}_0$ is not precise. Kocks[9] has proposed a description for $\hat{\sigma}_{\varepsilon s}$ that has the same form as that proposed by Haasen[10] for the beginning of dynamic recovery which in turn was based on calculations by Schoeck and Seeger[11] of the stress dependence of the activation energy for cross slip in fcc metals. The relation is written:

$$\ln \frac{\dot{\varepsilon}}{\dot{\varepsilon}_{\varepsilon s0}} = \frac{g_{0\varepsilon s} \mu b^3}{kT} \ln \frac{\hat{\sigma}_{\varepsilon s}}{\hat{\sigma}_{\varepsilon s0}}, \tag{10}$$

where $\dot{\varepsilon}_{\varepsilon s0}$, $g_{0\varepsilon s}$, and $\hat{\sigma}_{\varepsilon s0}$ are constants.

References

1. P.S. Follansbee and U.F. Kocks: A Constitutive Description of Copper Based on the Use of the Mechanical Threshold Stress as an Internal State Variable, *Acta metall.*, 1988, vol. 36, pp. 81-93.
2. P.S. Follansbee and G.T. Gray, III: An Analysis of the Low Temperature and High-Strain-Rate Deformation of Ti-6Al-4V, *Metall. Trans. A*, 1989, vol. 20A, pp. 863-874.
3. P.S. Follansbee, J.C. Huang, and G.T. Gray, III: Low-Temperature and High-Strain-Rate Deformation of Nickel and Nickel-Carbon Alloys and Analysis of the Constitutive Behavior According to An Internal State Variable Model, *Acta metall.*, 1990, vol. 38, pp. 1241-1254.
4. S.R. Chen and G.T. Gray, III: Constitutive Behavior of Tantalum and Tantalum-Tungsten Alloys, *Metall. Trans. A*, 1996, vol. 27A, pp. 2994-3006.
5. U.F. Kocks and H. Mecking: Physics and Phenomenology of Strain Hardening: the FCC Case, *Progress in Materials Science*, 2003, vol. 48, pp. 171-273.
6. U.F. Kocks, A.S. Argon, and M.F. Ashby: *Thermodynamics and Kinetics of Slip*, Progress in Materials Science, Vol. 19, Pergamon Press, New York, 1975.
7. Y.P. Varshni: Temperature Dependence of the Elastic Constants, *Phys. Rev. B*, 1970, vol. 2, pp. 3952-3958.

8. H. Mecking and U.F. Kocks: Kinetics of Flow and Strain-Hardening, *Acta metall.*, 1981, vol. 29, pp. 1865-1875.
9. U.F. Kocks: Laws for Work-Hardening and Low-Temperature Creep, *J. Eng. Mater. Tech., Trans. ASME*, 1976, vol. 98, pp. 76-85.
10. P. Hassen: Plastic Deformation of Nickel Single Crystals at Low Temperatures, *Phil. Mag.*, 1958, vol. 3, pp. 384-418.
11. G. Schoeck and A. Seeger: *Defects in Crystalline Solids*, Physical Society, London, 1955.
12. S.R. Chen, M.G. Stout, U.F. Kocks, S.R. MacEwen, and A.J. Beaudoin: Constitutive Modeling of a 5182 Aluminum as a Function of Strain Rate and Temperature, *Hot Deformation of Aluminum Alloys II*, T.R. Bieler, L. Lalli, and S.R. MacEwen, eds., The Minerals, Metals & Materials Society, 1998.
13. W.R. Blumenthal, R.W. Carpenter, G.T. Gray, III, D.D. Vannon, and S.P. Abeln: Influence of Strain Rate and Temperature on the Mechanical Behavior of Beryllium, *Shock Compression of Condensed Matter*, Proc. Vol. 429, AIP, 1997, pp. 411-414.
14. D.W. Brown*, et al.*: Development of Crystallographic Texture during High Rate Deformation of Rolled and Hot Pressed Beryllium, *Metall. Trans. A*, 2005, vol. 36, pp. 929-939.
15. S.R. Chen and U.F. Kocks: High-Temperature Plasticity in Copper Polycrystals, *High Temperature Constitutive Modeling - Theory and Application*, A.D. Freed and K.P. Walker, eds., Atlanta, GA, The American Society of Mechanical Engineers, 1991, pp. 1-12.
16. S.R. Chen, P.J. Maudlin, and G.T. Gray, III: Constitutive Behavior of Model FCC, BCC, and HCP Metals: Experiments, Modeling and Validation, *The Seventh International Symposium on Plasticity and Its Current Applications*, A.S. Khan, ed. Cancun, Mexico, Neat Press, 1999, pp. 623-626.
17. E. Cerreta, C.A. Yablinsky, G.T. Gray, III, S.C. Vogel, and D.W. Brown: The Influence of Grain Size and Texture on the Mechanical Response of High Purity Hafnium, *Materials Science and Engineering A*, 2007, vol. 456, pp. 243-251.
18. S.R. Chen, P.J. Maudlin, and G.T. Gray, III: Mechanical Properties and Constitutive Relations for Molybdenum under High-rate Deformation, *Molybdenum and Molybdenum Alloys*, A. Crowson, E.S. Chen, J.A. Shields, and P.R. Subramanian, eds., The Minerals, Metals & Materials Society, 1998, pp. 155-172.
19. G.T. Gray, III, S.R. Chen, and K.S. Vecchio: Influence of Grain Size on the Constitutive Response and Substructure Evolution of MONEL 400, *Metall. Trans. A*, 1999, vol. 30A, pp. 1235-1247.
20. U.F. Kocks and S.R. Chen: On the Two Distinct Effects of Thermal Activation on Plasticity: Application to Nickel, *phys. stat. sol. (a)*, 1992, vol. 131, pp. 403-413.
21. A.J. Beaudoin, A. Acharya, S.R. Chen, D.A. Korzekwa, and M.G. Stout: Consideration of Grain-Size Effect and Kinetics in the Plastic Deformation of Metal Polycrystals, *Acta mater.*, 2000, vol. 48, pp. 3409-3423.
22. C.M. Cady, S.R. Chen, G.T. Gray, III, D.A. Korzekwa, and J.F. Bingert: Dynamic Materials Testing, Texture, and Yield-Surface Calculation of an Automotive Sheet Steel, *Metall. Trans. A*, 2000, vol. 31A, pp. 2439-2448.

23. S.R. Chen, G.T. Gray, III, and S.R. Bingert: Mechanical Properties and Constitutive Relations for Tantalum and Tantalum Alloys under High-Rate Deformation, *Tantalum*, The Minerals, Metals, & Materials Society, 1996, pp. 173-184.
24. P.J. Maudlin, J.F. Bingert, J.W. House, and S.R. Chen: On the Modeling of the Taylor Cylinder Impact Test for Orthotropic Textured Materials: Experimental and Simulations, *International J. Plasticity*, 1999, vol. 15, pp. 139-166.
25. G.T. Gray, III and K.S. Vecchio: Influence of Peak Pressure and Temperature on the Structure/Property Response of Shock-Loaded Ta and Ta-10W, *Metall. Trans. A*, 1995, vol. 26A, pp. 2555-2562.
26. S.R. Chen and G.T. Gray, III: Constitutive Behavior of Tungsten and Tantalum: Experiments and Modeling, *2nd International Conference on Tungsten and Refractory Metals*, A. Bose and R.J. Dowding, eds., October 17-19, McLean, VA, Metal Powder Industries Federation, Princeton, New Jersey, 1995, pp. 489-498.
27. S. Nemat-Nasser and W. Guo: High Strain-rate Response of Commercially Pure Vanadium, *Mech. Mater.*, 2000, vol. 32, pp. 243-260.
28. S.G. Song and G.T. Gray, III: Influence of Temperature and Strain Rate on Slip and Twinning Behavior of Zr, *Metall. Trans. A*, 1995, vol. 26A, pp. 2665-2675.
29. S.R. Chen and G.T. Gray, III: Influence of Twinning on the Constitutive Response of Zr: Experiments and Modeling, *J. DE PHYSIQUE IV*, 1997, vol. 7, pp. 741-746.

The constitutive model fit with the MTS model for the DU plate studied was found to be excellent as seen in Fig 1 and Fig. 2 for the through-thickness and in-plane compression directions. The MTS parameters are listed in Tables 1 and 2. The work hardening of this material is observed to be strongly dependent on strain rate and temperature. It was found to be even more significant for the material deformed in the in-plane direction where deformation twinning is the initially dominant deformation mechanism.

To address uncertainty assessment, a rolling study was performed following a specification established to process this wrought DU plate stock. Within the specification, DU plate material was found to exhibit acceptable variation in its mechanical response. The effect of this variation on the constitutive model can be captured by an adjustment to a single parameter, namely the mechanical threshold saturation stress that represents the absolute strength of a material without thermal activation assistance. This result is shown in Fig. 3. Within this tight specification, it is not surprised to see that a change in the saturation stress in the amount of +-8.3% captures the experimental data reasonably well. We have newer data obtained from historical materials that exhibit a much wider and distinct variation in strength as discussed in the historical opening chapter of this report. We will report these results separately in the future to provide guideline in treating this material in calculations and simulations.

The fit to the PTW constitutive model is presented in the next section. One caution concerning the PTW model is that it has a separate power-law relation to provide a much higher mechanical stress often thought to be necessary at much higher strain rates ($>10^5$/s) such as are needed for simulating shock-loading. Without proper derivation, the parameters for this range of deformation due to lack of experimental data, it can be harmful to simply apply the PTW model in the simulation of lower-rate experiments. We are in the process of quantifying additional data to better constrain a few of the parameters listed in the PTW model by simulating results both in flyer-impact and Rayleigh-Taylor instability experiments that each probe the higher strain-rate behavior of materials.

Uranium-depleted (through-thickness): MTS Model Fit

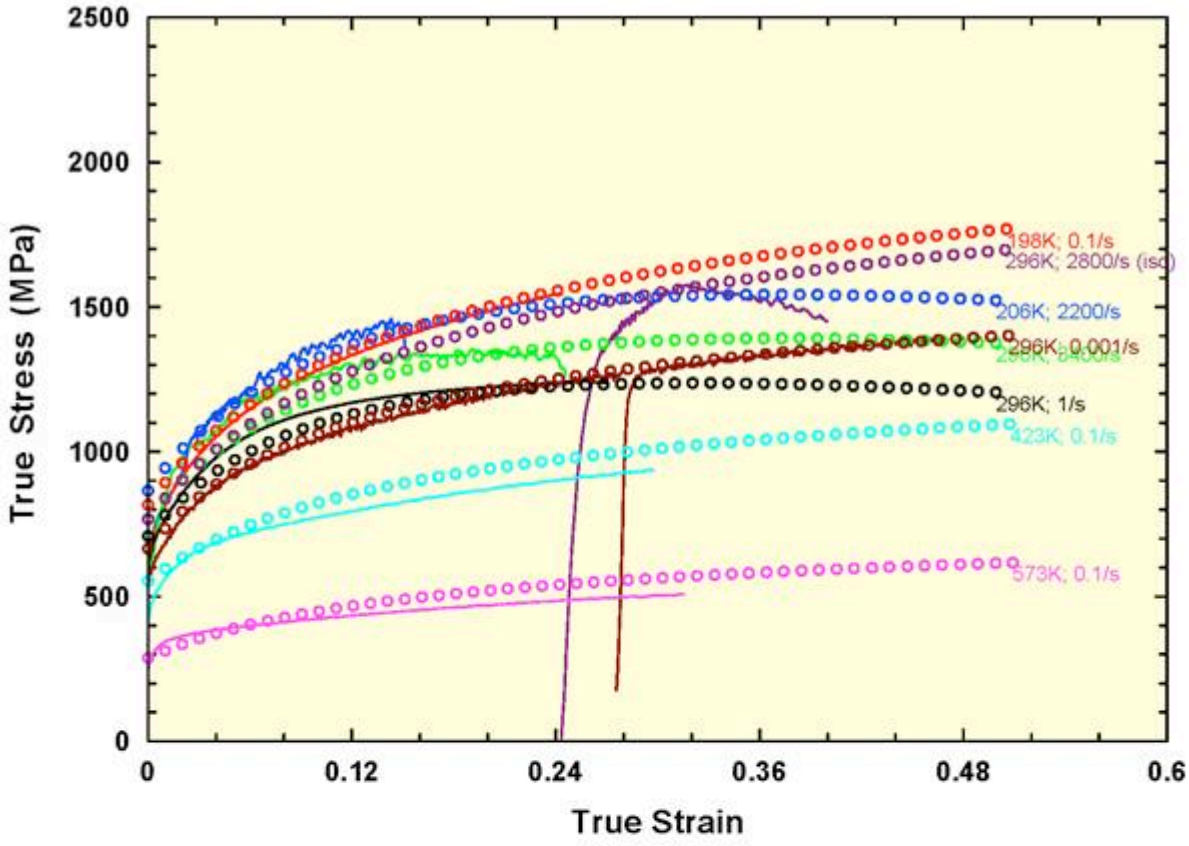

1 : DUtt-67223.p.txt	206K; 2200/s
2 : DUtt-7510-1.p.txt	198K; 0.1/s
3 : DUtt023343.p.txt	296K; 3400/s
4 : DUtt023283r.p.txt	296K; 2800/s
5 : DUtt023100.p.txt	296K; 1/s
6 : DUtt02310-3b.p.txt	*296K; 0.001/s
7 : DUtt02310-3br.p.txt	296K; 0.001/s
8 : DUtt15010-1.p.txt	423K; 0.1/s
9 : DUtt30010-1.p.txt	573K; 0.1/s
10 : DUtt-67223.p.txt.aMTSf	206K; 2200/s
11 : DUtt-7510-1.p.txt.MTSf	198K; 0.1/s
12 : DUtt023343.p.txt.aMTSf	296K; 3400/s
13 : DUtt023283r.p.txt.MTSf	296K; 2800/s (iso)
14 : DUtt023100.p.txt.aMTSf	296K; 1/s
15 : DUtt02310-3b.p.txt.MTSf	296K; 0.001/s
16 : DUtt15010-1.p.txt.MTSf	423K; 0.1/s
17 : DUtt30010-1.p.txt.MTSf	573K; 0.1/s

Fig. 1 Stress/strain responses and the MTS model fit (symbols) to an annealed DU plate.

Uranium-depleted (in-plane): MTS Model Fit

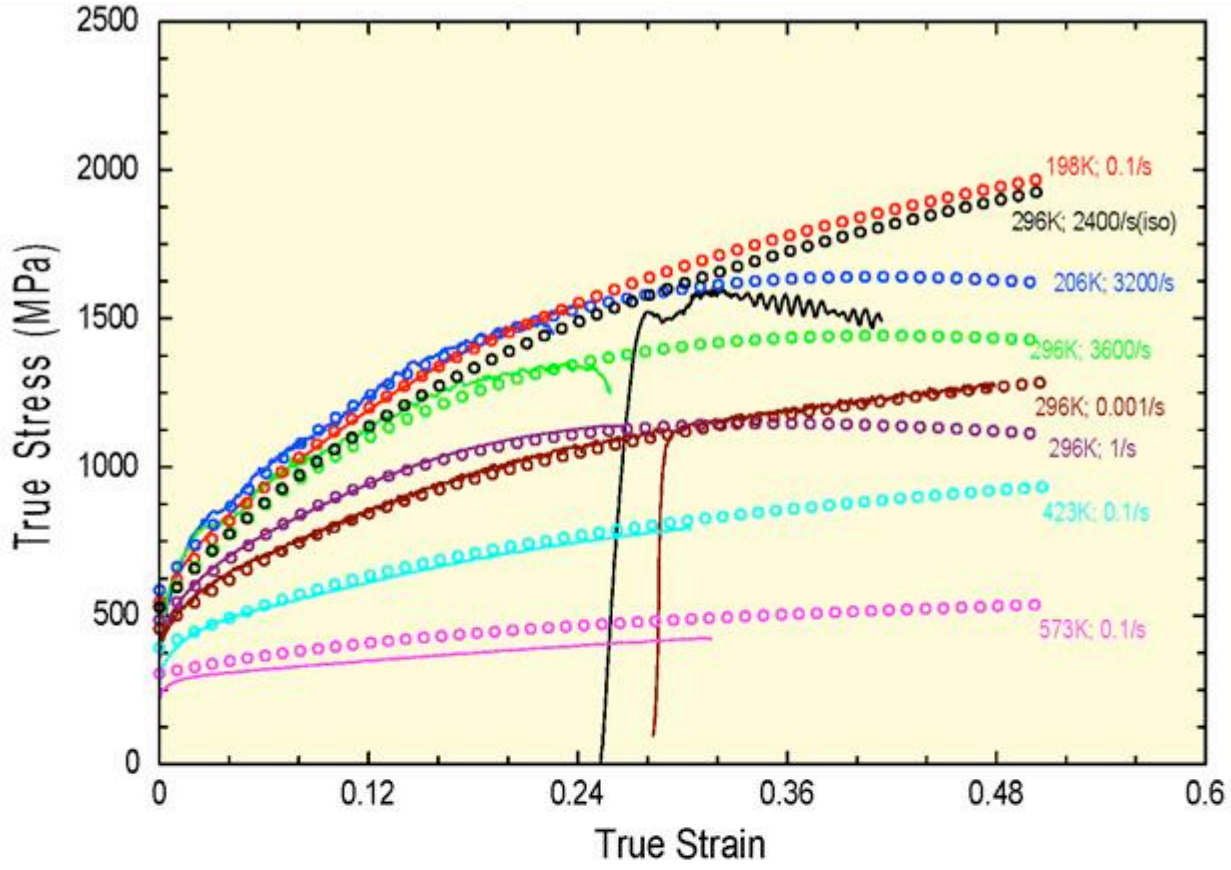

1 : DUip-67323.p.txt	206K; 3200/s
2 : DUip-7510-1.p.txt	198K; 0.1/s
3 : DUip023363.p.txt	296K; 3600/s
4 : DUip023243r.p.txt	296K; 2400/s
5 : DUip023100.p.txt	296K; 1/s
6 : DUip02310-3b.p.txt	*296K; 0.001/s
7 : DUip02310-3br.p.txt	296K; 0.001/s
8 : DUip15010-1.p.txt	423K; 0.1/s
9 : DUip30010-1.p.txt	573K; 0.1/s
10 : DUip-67323.p.txt.aMTSf	206K; 3200/s
11 : DUip-7510-1.p.txt.MTSf	198K; 0.1/s
12 : DUip023363.p.txt.aMTSf	296K; 3600/s
13 : DUip023243r.p.txt.MTSf	296K; 2400/s(iso)
14 : DUip023100.p.txt.aMTSf	296K; 1/s
15 : DUip02310-3b.p.txt.MTSf	296K; 0.001/s
16 : DUip15010-1.p.txt.MTSf	423K; 0.1/s
17 : DUip30010-1.p.txt.MTSf	573K; 0.1/s

Fig. 2 Stress/strain responses and the MTS model fit (symbols) to an annealed DU plate.

Table 1 Equations and Parameters of a Depleted Uranium (thru-thickness comp) for the MTS Model

- $\frac{\sigma}{\mu} = \frac{\sigma_a}{\mu} + S_i(\dot{\varepsilon},T)\frac{\hat{\sigma}_i}{\mu_0} + S_\varepsilon(\dot{\varepsilon},T)\frac{\hat{\sigma}_\varepsilon}{\mu_0}$

  Where: σ_a = 40 MPa

- $\mu = \mu_0 - \frac{742.7\ MPa}{\exp\left(\frac{10.93\ K}{T}\right) - 1}$

  Where: μ_0 = 1.0672×10^5 MPa

- $S_i(\dot{\varepsilon},T) = \left\{1 - \left[\frac{kT}{\mu b^3 g_{0i1,2}}\ln\left(\frac{\dot{\varepsilon}_{0i}}{\dot{\varepsilon}}\right)\right]^{1/q_i}\right\}^{1/p_i}$

  Where: $\frac{k}{b^3}$ = 0.511 MPa / K, b~3×10^{-10} m
  $\dot{\varepsilon}_{0i}$ = 1×10^7 s^{-1}
  q_i=3/2 $p_{i=}$ 1/2 g_{0i} = 0.715
  $\frac{\hat{\sigma}_i}{\mu_0}$ = 0.01055, $\hat{\sigma}_i$ =1126 MPa

- $S_\varepsilon(\dot{\varepsilon},T) = \left\{1 - \left[\frac{kT}{\mu b^3 g_{0\varepsilon}}\ln\left(\frac{\dot{\varepsilon}_{0\varepsilon}}{\dot{\varepsilon}}\right)\right]^{1/q_\varepsilon}\right\}^{1/p_\varepsilon}$

  Where: $\dot{\varepsilon}_{0\varepsilon}$ = 1×10^7 s^{-1}
  g_{0_ε} = 1.6
  q_{0_ε} = 1 p_{0_ε} = 2/3

- $\frac{d\hat{\sigma}_\varepsilon}{d\varepsilon} = \theta_0(\dot{\varepsilon},T)\cdot\left[1 - \frac{\tanh\left(\alpha\frac{\hat{\sigma}_\varepsilon}{\hat{\sigma}_{\varepsilon s}(\dot{\varepsilon},T)}\right)}{\tanh(\alpha)}\right]$

  Where:
  θ_0 = 4000 MPa
  α = 2.0 or κ = 2.2

  or $\frac{d\hat{\sigma}_\varepsilon}{d\varepsilon} = \hat{\theta}_0\cdot\left[1 - \frac{\hat{\sigma}_\varepsilon}{\kappa\cdot\hat{\sigma}_{\varepsilon v}}\right]^{\kappa} = \hat{\theta}_0\cdot\left[1 - \frac{\hat{\sigma}_\varepsilon}{\hat{\sigma}_{\varepsilon s}}\right]^{\kappa}$

- $\ln\frac{\hat{\sigma}_{\varepsilon s}}{\hat{\sigma}_{\varepsilon s0}} = \frac{kT}{\mu b^3 g_{0\varepsilon s}}\ln\frac{\dot{\varepsilon}}{\dot{\varepsilon}_{0\varepsilon s}}$

  Where: $g_{0_\varepsilon s}$ = 0.089
  $\hat{\sigma}_{\varepsilon s0}$ = 1870 MPa
  $\dot{\varepsilon}_{0\varepsilon s}$ = 1×10^7 s^{-1}

- $\Delta T = \frac{\Psi}{\rho C_p}\int\sigma(\varepsilon)d\varepsilon;\ when\dot{\varepsilon} \geq 1s^{-1}$

  Where: Ψ = 0.95
  ρ = 19.05 Mg/m^3
  C_p = 0.14 MPa m^3/Mg/K

Table 2 Equations and Parameters of a Depleted Uranium (in-plane comp.) for the MTS Model

- $\frac{\sigma}{\mu} = \frac{\sigma_a}{\mu} + S_i(\dot{\varepsilon}, T)\frac{\hat{\sigma}_i}{\mu_0} + S_\varepsilon(\dot{\varepsilon}, T)\frac{\hat{\sigma}_\varepsilon}{\mu_0}$

  Where: $\sigma_a = 40$ MPa

- $\mu = \mu_0 - \frac{742.7\ MPa}{\exp\left(\frac{10.93\ K}{T}\right) - 1}$

  Where: $\mu_0 = 1.0672\times10^5$ MPa

- $S_i(\dot{\varepsilon}, T) = \left\{1 - \left[\frac{kT}{\mu b^3 g_{0i1,2}} \ln\left(\frac{\dot{\varepsilon}_{0i}}{\dot{\varepsilon}}\right)\right]^{1/q_i}\right\}^{1/p_i}$

  Where: $\frac{k}{b^3} = 0.511$ MPa / K, b~3×10^{-10} m
  $\dot{\varepsilon}_{0i} = 1\times10^7\ s^{-1}$
  q_i=3/2 $p_{i=}$ 1/2 $g_{0i} = 0.715$
  $\frac{\hat{\sigma}_i}{\mu_0} = 0.00655$, $\hat{\sigma}_i$=699 MPa

- $S_\varepsilon(\dot{\varepsilon}, T) = \left\{1 - \left[\frac{kT}{\mu b^3 g_{0\varepsilon}} \ln\left(\frac{\dot{\varepsilon}_{0\varepsilon}}{\dot{\varepsilon}}\right)\right]^{1/q_\varepsilon}\right\}^{1/p_\varepsilon}$

  Where: $\dot{\varepsilon}_{0\varepsilon} = 1\times10^7\ s^{-1}$
  $g_{0\varepsilon} = 1.6$
  $q_{0\varepsilon} = 1$ $p_{0\varepsilon} = 2/3$

- $\frac{d\hat{\sigma}_\varepsilon}{d\varepsilon} = \theta_0(\dot{\varepsilon}, T)\cdot\left[1 - \frac{\tanh\left(\alpha\frac{\hat{\sigma}_\varepsilon}{\hat{\sigma}_{\varepsilon s}(\dot{\varepsilon}, T)}\right)}{\tanh(\alpha)}\right]$

  Where:
  $\theta_0 = 4000$ MPa
  $\alpha = 2.0$
  or $\kappa = 2.2$

  or $\frac{d\hat{\sigma}_\varepsilon}{d\varepsilon} = \hat{\theta}_0\cdot\left[1 - \frac{\hat{\sigma}_\varepsilon}{\kappa\cdot\hat{\sigma}_{\varepsilon v}}\right]^\kappa = \hat{\theta}_0\cdot\left[1 - \frac{\hat{\sigma}_\varepsilon}{\hat{\sigma}_{\varepsilon s}}\right]^\kappa$

- $\ln\frac{\hat{\sigma}_{\varepsilon s}}{\hat{\sigma}_{\varepsilon s0}} = \frac{kT}{\mu b^3 g_{0\varepsilon s}} \ln\frac{\dot{\varepsilon}}{\dot{\varepsilon}_{0\varepsilon s}}$

  Where: $g_{0\varepsilon s} = 0.0425$
  $\hat{\sigma}_{\varepsilon s0} = 4500$ MPa
  $\dot{\varepsilon}_{0\varepsilon s} = 1\times10^7\ s^{-1}$

- $\Delta T = \frac{\Psi}{\rho C_p}\int\sigma(\varepsilon)d\varepsilon;\ when\dot{\varepsilon} \geq 1s^{-1}$

  Where: $\Psi = 0.95$
  $\rho = 19.05$ Mg/m^3
  $C_p = 0.14$ MPa m^3/Mg/K

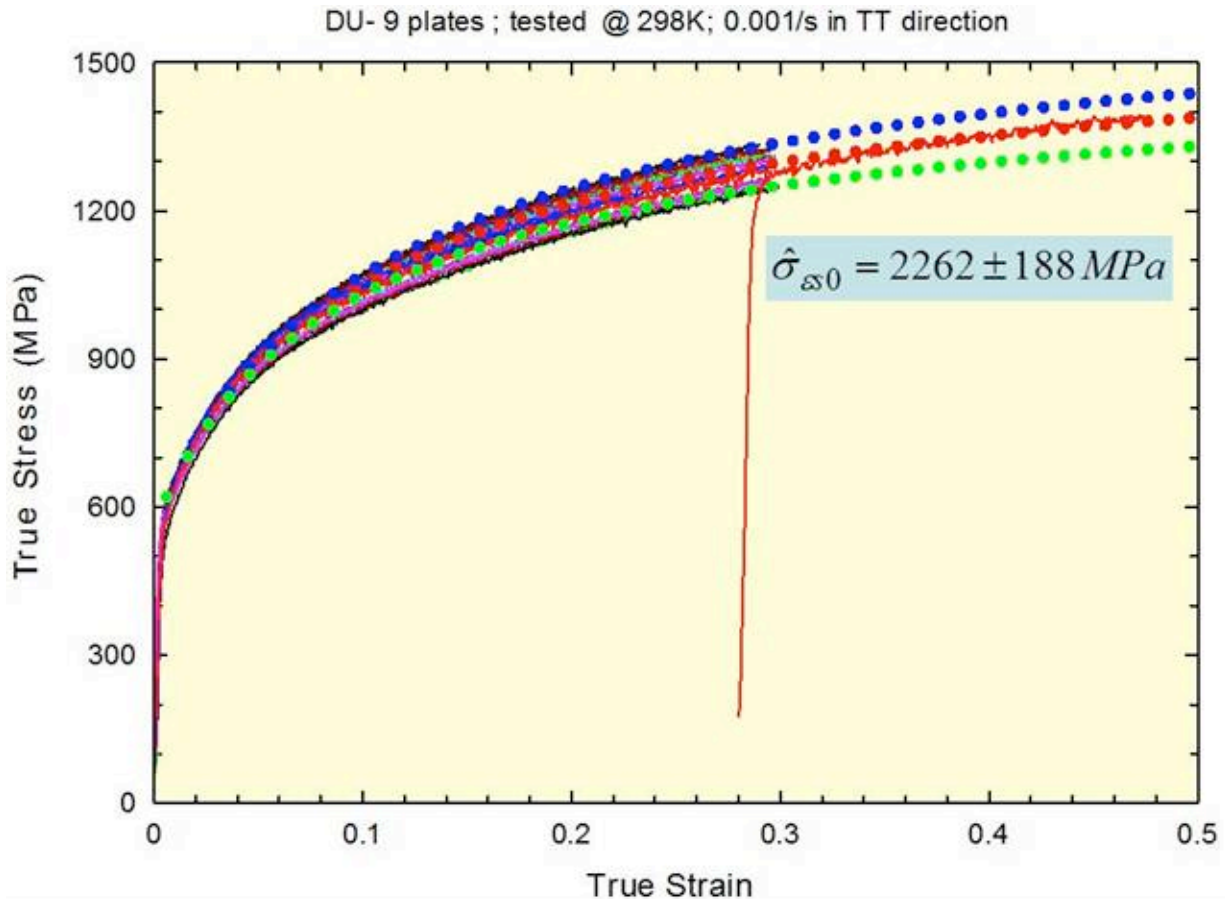

Fig. 3 Stress/strain responses and the MTS model fit (symbols) to an annealed DU plate showing the uncertainty.

Description of the PTW model:

The PTW model was developed by **P**reston (X-DO), **T**onks (XN-H), and **W**allace (T-1) [*Model of plastic deformation for extreme loading conditions, Dean L. Preston, Davis L, Tonks, and Duane C. Wallace, Journal of Applied Physics, Vol. 93, 2003, pp. 211-220*] to describe thermo-plastic flow for arbitrary plastic strains, strain rates, and temperatures. The model was formulated to describe the mechanical responses at low strain rates ($<10^4$/s) based on physics of thermally activated dislocation-obstacle interactions, and was extended to describe the high strain-rate behavior based on the theory of overdriven shocks in metals ($\gg 10^5$/s).

Nomenclature:

$\hat{\tau}$: normalized stress ($\equiv \tau / G$)
ψ: true plastic strain
$\dot{\psi}$: true plastic strain rate
σ: flow stress ($\equiv 2 \cdot \hat{\tau} \cdot G$)
p: a constant that modifies Voce hardening law
θ_0: initial normalized strain hardening rate $(\mathrm{d}\hat{\tau} / \mathrm{d}\Psi)_{\psi=0}$

$\hat{\tau}_y$: normalized yield stress
$\hat{\tau}_s$: normalized saturation stress

$\dot{\xi}$: a constant relates to the shear wave velocity in a given material
κ: a constant relates to the temperature dependence in thermally activated regime
γ: a constant relates to the strain-rate dependence in thermally activated regime
ρ: material density
M: atomic weight

S_0: the maximum normalized saturation stress (at 0K)
S_∞: the minimum normalized saturation stress (approaching melting temperature)
y_0: the maximum normalized yield stress (at 0K)
y_∞: the minimum normalized yield stress (approaching melting temperature)
y_1: a normalized yield stress used in describing the high-rate sensitivity in drag regime
y_2: an exponent in the power law in describing the high-rate sensitivity in drag regime
β: an exponent in the power law in describing the high-rate sensitivity in drag regime

G: shear modulus
G_0: shear modulus at 0K
T: temperature in Kelvin

T_m : absolute melting temperature in Kelvin

$\hat{T}$: normalized temperature ($\equiv T/T_m$)

α : a constant describing temperature-dependent of shear modulus

C_v : heat capacity

The work hardening function used in the PTW model was a modified Voce work hardening law in the following form:

$$\frac{d\hat{\tau}}{d\psi} = \theta_0 \frac{\exp\left[p\frac{\hat{\tau}_s - \hat{\tau}}{S_0 - \hat{\tau}_y}\right] - 1}{\exp\left[p\frac{\hat{\tau}_s - \hat{\tau}_y}{S_0 - \hat{\tau}_y}\right] - 1} \qquad (11)$$

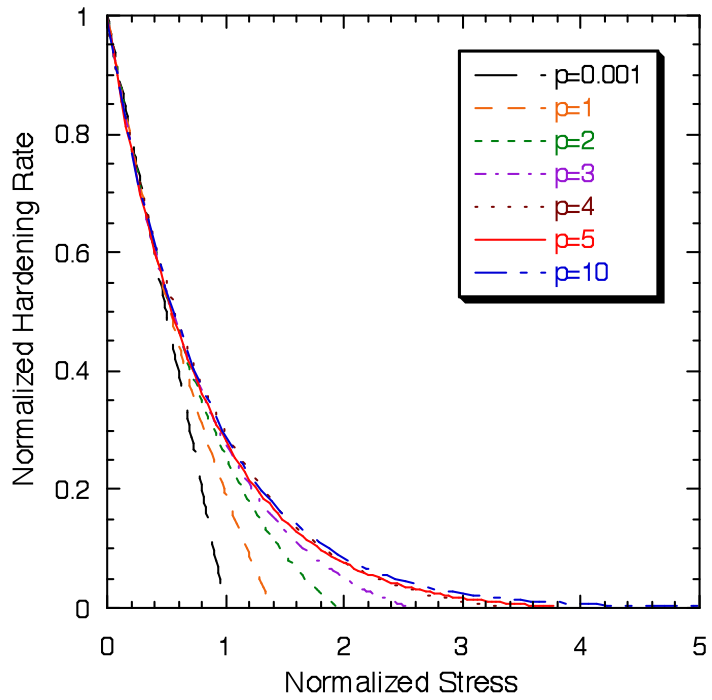

(Note: There is no practical difference when p>4. An integer of p=2, 3, or 4 captures the hardening behavior for most materials satisfactorily. p<2 (indicating material reaches saturation stress early) is not recommended since it introduces large error at strain >0.3)

By integrating the above equation, it yields the following equation relating the normalized flow stress ($\hat{\tau}$) to strain (ψ):

$$\hat{\tau} = \hat{\tau}_s + \frac{1}{p}\left(S_0 - \hat{\tau}_y\right)\cdot \ln\left[1 - \left[1 - \exp\left(-p\frac{\hat{\tau}_s - \hat{\tau}_y}{s_0 - \hat{\tau}_y}\right)\right]\cdot \exp\left\{-\frac{p\cdot\theta_0\cdot\psi}{\left(S_0 - \hat{\tau}_y\right)\left[\exp\left(p\frac{\hat{\tau}_s - \hat{\tau}_y}{s_0 - \hat{\tau}_y}\right) - 1\right]}\right\}\right] \quad (12).$$

The flow stress under a defined deformation path such as compression is defined as:

$$\sigma \equiv 2\cdot\hat{\tau}\cdot G \quad (13)$$

Shear modulus as a function of temperature is represented by the following equation:

$$G = G_0\cdot(1 - \alpha\cdot\hat{T}) \quad (14)$$

where

$$\hat{T} = T/T_m. \quad (15)$$

There are two major quantities in equation (12), namely the normalized yield stress ($\hat{\tau}_y$) and the normalized saturation stress ($\hat{\tau}_s$). In the PTW model the normalized yield stress as a function of temperature and strain rate in the dislocation glide regime was described by the following equation:

$$\hat{\tau}_y = y_0 - \left(y_0 - y_\infty\right)\cdot erf\left[\kappa\hat{T}\cdot\ln\left(\frac{\gamma\dot{\xi}}{\dot{\psi}}\right)\right] \quad (16).$$

In the above equation, a constant $\dot{\xi}$ which related to the shear wave velocity in a given material is defined as:

$$\dot{\xi} = \frac{1}{2}\left(\frac{4\pi\rho}{3M}\right)^{1/3}\left(\frac{G}{\rho}\right)^{1/2} \quad (17)$$

In the dislocation drag regime, the yield stress is described by a power-law relation which is strain-rate dependent by the following two terms:

$$y_1\left(\frac{\dot{\psi}}{\gamma\dot{\xi}}\right)^{y_2} \qquad (18)$$

and

$$S_0\left(\frac{\dot{\psi}}{\gamma\dot{\xi}}\right)^{\beta} \qquad (19).$$

Depending on the values used in Eq. (16), (18) and (19), the next figure shows one of the possible relations among the yield stresses calculated from these equations. The yield stress as a function of strain rate in the thermally activated regime represented by Eq. (16) is shown in this figure by a solid line (labeled as yield_disl.glide). As indicated in this curve it has weaker rate-sensitivity. The high-rate sensitivities as suggested from shock data where the deformation is controlled by dislocation drag, empirical relations (Eq. (18)-(19)) are used to capture the yield stress increase as a function of strain rate. They are labeled as yield_drag.1 (Eq. (18)) and yield_drag.2 (Eq. (19)) in this figure.

The PTW model combines Eq. (16), (18) and (19) into one equation to describe the material yield stress as a function of temperature and strain rate for both dislocation-glide and dislocation-drag regimes:

$$\hat{\tau}_y = \max\left\{ y_0 - (y_0 - y_\infty)\cdot erf\left[\kappa\hat{T}\cdot\ln\left(\frac{\gamma\dot{\xi}}{\dot{\psi}}\right)\right], \min\left[y_1\left(\frac{\dot{\psi}}{\gamma\dot{\xi}}\right)^{y_2}, S_0\left(\frac{\dot{\psi}}{\gamma\dot{\xi}}\right)^{\beta}\right]\right\} \qquad (20),$$

the resulting yield stress ($\hat{\tau}_y$) is shown as solid symbols in this figure.

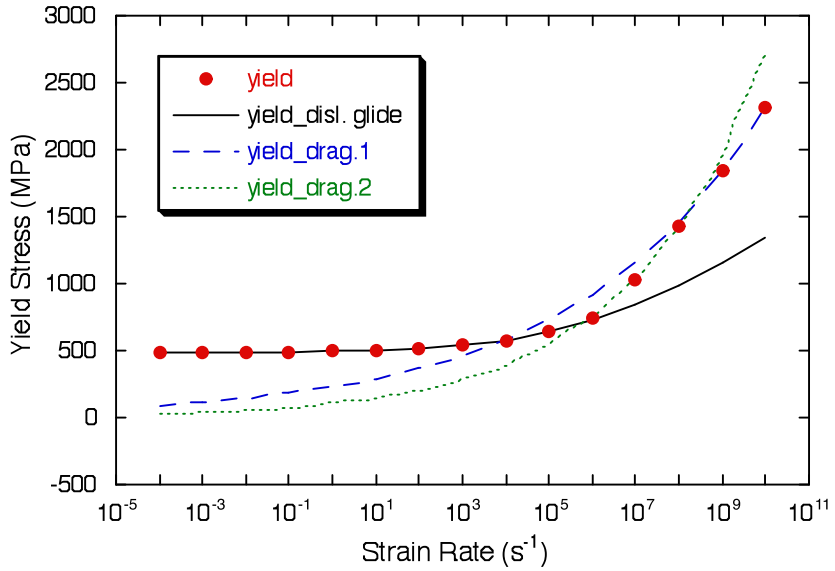

(Note: The strain rate where the PTW model dictates a transition from thermally-activated dislocation glide mechanism to dislocation motion governed by phono drag mechanism depends on the value of y_2 and β in equations 20 and 21. Those values were derived by analyzing the strong shock data according to P.T.W. From mathematical point of view, the transition can occur as early as at 10^3/s or as late as at 10^9/s using the values of y_2 and β listed in the PTW paper. Based on extensive validations of materials parameters of constitutive model(s) using the Taylor cylinder impact test (10^4/s-10^5/s), the thermally activated dislocation glide remains as the controlling deformation mechanism for strain rates $<10^5$/s).

Using the same approach, the normalized total saturation stress is represented by:

$$\hat{\tau}_s = \max\left\{S_0 - (S_0 - S_\infty)\cdot erf\left[\kappa\hat{T}\cdot\ln\left(\frac{\gamma\dot{\xi}}{\dot{\psi}}\right)\right], S_0\left(\frac{\dot{\psi}}{\gamma\dot{\xi}}\right)^{\beta}\right\} \qquad (21).$$

Mechanical properties of many materials have been measured under compression at various temperature and strain rates. In general the PTW model seems to capture the strain-rate and temperature sensitivities reasonably well within the experimental conditions where the deformation mechanism is controlled y thermally activated dislocation-obstacle interactions. In the extremely high strain rate regime, stress-strain data from shock experiments are necessary to derive the constants more accurately.

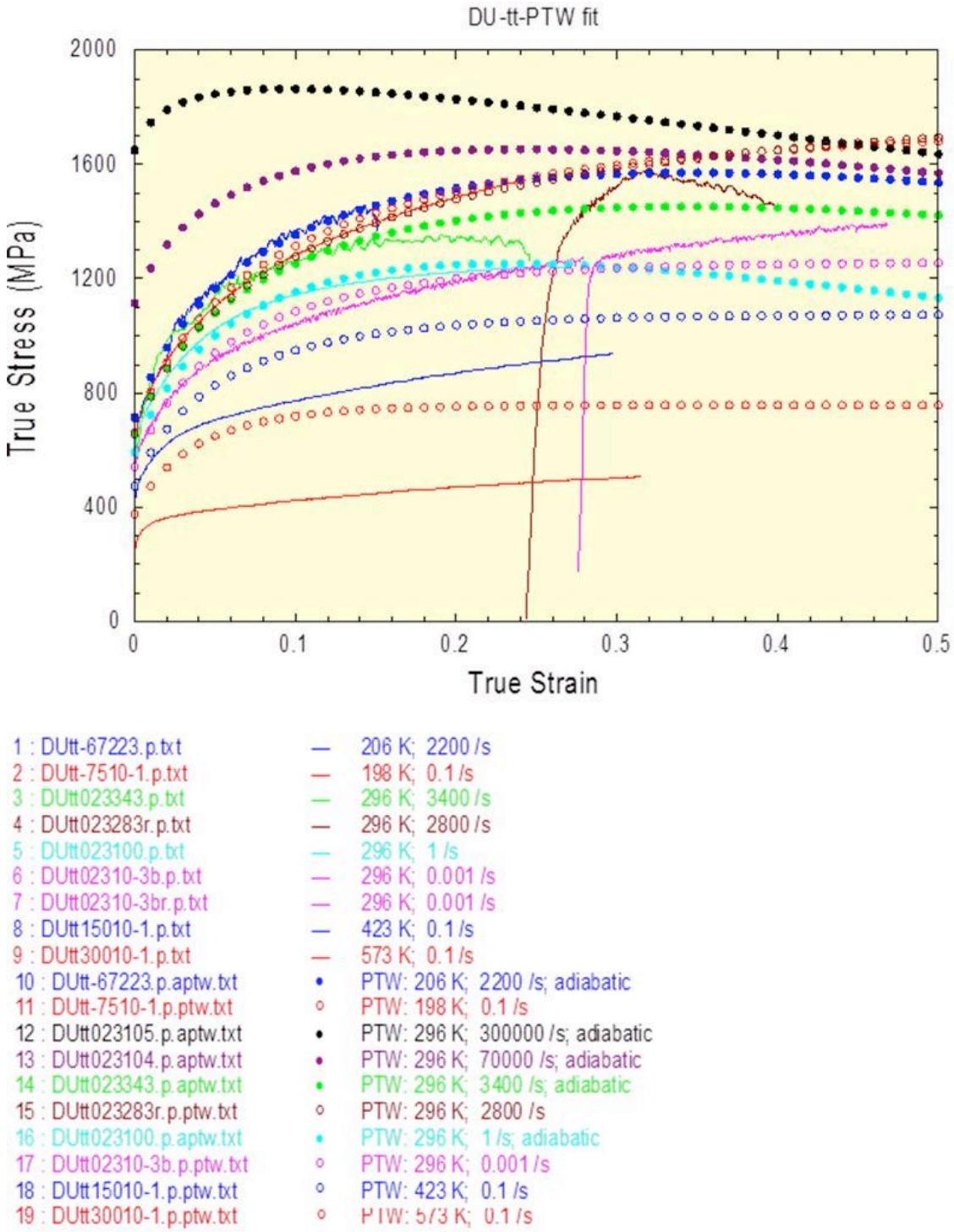

Fig. 4 Stress/strain responses and the PTW model fit (symbols) to DU.

Note: The top two PTW calculations (no data associated with them) show that the stress level can increase quickly at higher strain rates. It also means that if the parameters (y_2 and beta) for the drag regime are not correct, the error in calculations can be significant.

Table 3 NOMINAL SET OF PTW MODEL PARAMETERS FOR Depleted Uranium

Parameter	Parameter Description	Nominal Value
θ_0	Initial strain hardening rate $(d\hat{\tau}/d\Psi)_{\psi=0}$	0.088
p	Constant modifying Voce hardening law	3
S_0	Maximum saturation stress (at 0K)	0.0115
S_∞	Minimum saturation stress (~ melting)	0.0020
κ	Constant in thermal activation energy term- relates to the temperature dependence	0.1
γ	Constant in thermal activation energy term- relates to the strain rate dependence	1.0×10^{-7}
y_0	Maximum yield stress (at 0K)	0.004
y_∞	Minimum yield stress (~melting)	0.002
y_1	Material constant used in describing the high rate sensitivity in 2nd regime	0.0115
y_2	Material constant used in describing the high rate sensitivity in 2nd regime	0.27 (?)
β	Material constant used in describing the high rate sensitivity in 2nd regime	0.27 (?)
T_m	Melting temperature	1405 K
G_0	Shear modulus (at 0K)	107.8×10^9 N/m^2
α	Constant in G(T) Equation	0.89
C_v	Heat Capacity	200 J/Kg/K
A	Atomic weight	3.954×10^{-25} Kg/atom
ρ	Density	19050 Kg/m^3

Validation

Uranium - depleted

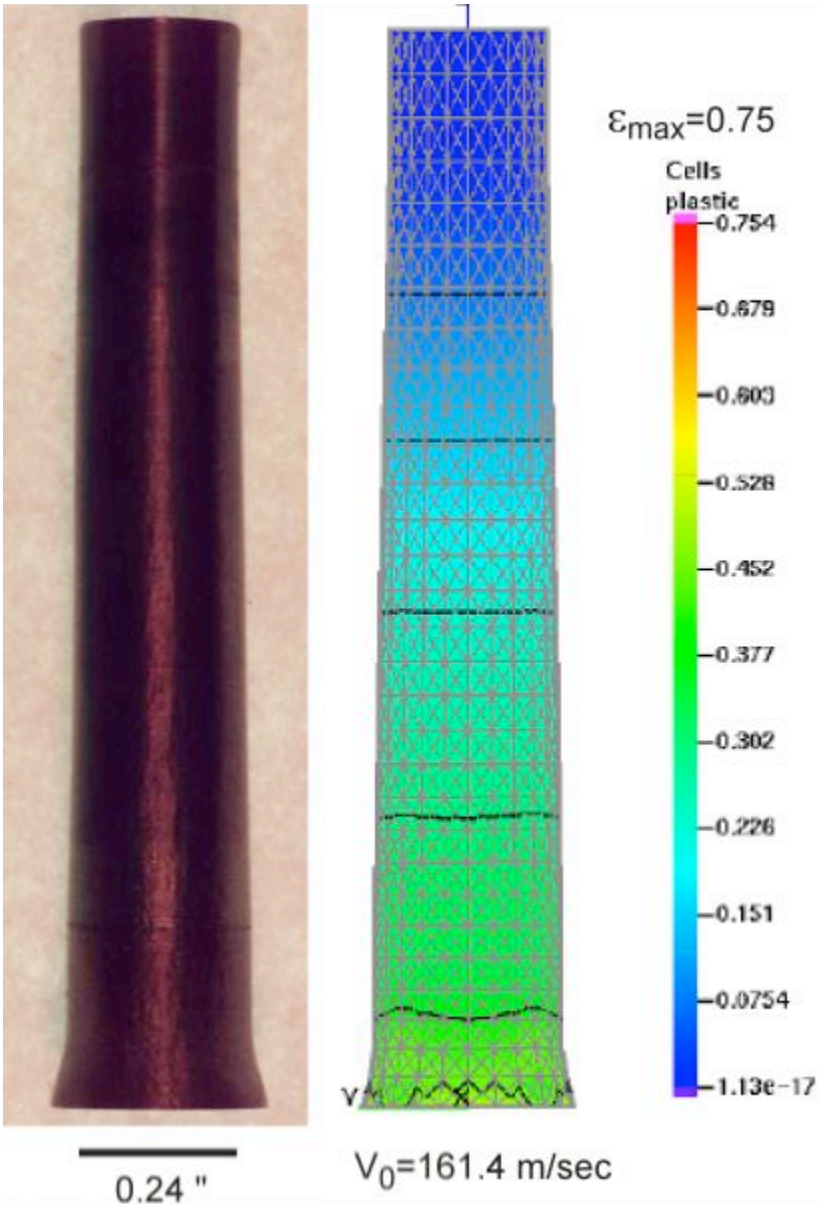

Fig. 5 Taylor cylinder impact test of an annealed DU; Experiment (left) and FEM calculation with the MTS model.

Mechanical Property, Constitutive Modeling and Validation of Shock Prestraining Effect on Depleted Uranium Constitutive Behavior

Mechanical Property and Constitutive Modeling:

Based on the experimental data available it is suggested that DU exhibits shock softening. The current constitutive models do not include structural softening built in other than thermal softening due to adiabatic heating. As such, it is necessary to model the shock effect based on a complete data set like the one shown in Fig. 1. Both the PTW (Fig. 6 and Table 4) and the MTS (Fig. 7 and Table 5) models are capable of describing the data set very well such that each can be readily used for post shock analysis and calculations that include the effect of shock prestraining on the post-shock mechanical response of DU. In large-code calculations for some applications, the plastic strains are tracked through the simulation that may be higher than the effective strains due to the shock and also at higher flow stress levels. This may in part be due to a strong Baushcinger effect as discussed in the shock=prestraining chapter of this report. It may be necessary therefore to reset the material strength following shock release and follow a new set of parameters to accurately capture the shock softening effect observed in shock prestrained DU.

Validation of Preshocked Constitutive Modeling

Three sub-scale cylindrical samples machined from a DU disk preshocked to 45 GPa with the dimensions of 0.2" diameter and 1" length for Taylor impact test were tested at initial velocity of 130.5, 135.7, and 138.5 m/s (Note: the nominal standard size of a typical Taylor cylinder is 0.3" in diameter and 1.5-2.0" in length). The post-mortem sample at the highest velocity of 138.5 m/s was digitized to facilitate direct comparison with FEM calculations using various sets of parameters for the MTS constitutive model. The MTS parameters of the depleted uranium in an annealed condition are shown in Table 3 and the fitting results are presented in Fig. 8.

First, the MTS parameters for an HE-shocked depleted uranium reported previously (Table 5 and Fig. 7) were used in an FEM simulation for comparison. The simulation results (color shades) are shown in Fig. 8 with the experimental postmortem profiles (red dashed lines) at half-plane of the cylinder and at the footprint. The agreement between experiment and simulation is excellent. The anisotropy of this rolled plate after shock is reproduced nicely using a Hill yield criterion (R. Hill, Proc. R. Soc. London, ser. B, vol. 193, pp. 281-297, 1948) that has been implanted in the FEM code.

As outlined in the first part of this report, depleted uranium after shock prestraining displayed significant deformation twin formation as part of the deformation accomodation processes. The post-shocked analysis indicating that shock softening might be occurring suggested a different approach apart from conventional metals possessing an fcc or bcc crystal structure should be explored. Accordingly, variations in the constitutive modeling parameters were input in the simulations to examine the best methodology to describe and to thereafter capture the shock prestraining effect on DU mechanical behavior using a

Taylor cylinder impact test. Four cases were studied and the results are shown in Fig. 10. Case labeled as (a) in this figure uses the mechanical properties measured from the preshocked sample with a new set of MTS parameters with most of the variables kept the same as the annealed starting condition. This treatment provides the best agreement between the experimental results and the simulation. Case labeled as (b) in Fig. 10 corresponds to the use of parameters for annealed DU (with (b) in superscript in Table 6). It is not surprising to see that the calculated profile is significantly softer (shorter in final length and wider in the waist zone with plastic deformation observed farther from impact surface) than the experimental profile.

When a metal or alloy is shock prestrained, the amount of deformation retained and the effect of the shock on the subsequent post-shock mechanical response strongly depends on the crustal structure of the material. For typical fcc metals such as copper and nickel, it is known they generally display enhanced hardening, that is, the flow stress of a shocked prestrained metal after shifting the amount of retained equivalent strains from EOS volume-pressure relation is higher than the flow stress level if that metal had received no shock but was deformed to the same plastic strain. For typical bcc metals such as tantalum and some steels, it is generally reported that no enhanced hardening is observed. Case labeled as (c) in Fig. 10 is the result of shifting about 0.28 true strain (the initial structure was initialized with a value of 800 MPa to represent a shocked structure in the MTS model, with (c) in superscript in Table 3). In this case, it is seen that the simulation is much stronger (less deformation with longer final length and bigger footprint due to lower work hardening rate at higher strains) than the measured experimental Taylor profile. From Fig. 5 that shows the difference of the measured flow stresses under the annealed condition and following shock prestraining and then the strain-shifted treatment, it is understandable that this approach (no enhanced hardening but retaining strain hardening as a function of the shocked strain path) is incorrect. In the case of the PTW model implementation, the shock hardening will be represented by strain accumulation in an FEM simulation following the equivalent strains calculated from the EOS. Therefore a standard treatment in an FEM simulation which performs a continuous strain increment in the event will yield a much harder material as depicted in case (c) in Fig. 10 and therefore inaccurately model the effect of shock prestraining on DU.

A fourth and final case investigated was in line with the approach as shown in Fig. 4 previously to address the mixture of strain hardening due to the shock and softening due to the extensive twinning propensity observed in shocked DU. The net result is a reduced effective shock hardening which indicates a smaller strain shift is sufficient to represent the shock prestraining effect in DU. The shocked structure was initialized with a mechanical threshold strength at 450 MPa in the MTS model (with (d) in superscript in Table 3). The FEM calculation and experiment is shown in Fig. 10 as case (d). The agreement between them is very good and is very close to what one gets from case (a). In the PTW model, this treatment corresponds to a smaller strain shift required in the calculations than would result if the strain path is calculated from the EOS.

Recommendation:

During a shock-loading event, the EOS volume-pressure relation in an FEM code calculation keeps track of how much plastic strain a material receives. For different shock peak stresses (pressure) there is a different amount of retained shock strain. Complicating the complexity of the modeling is the fact that it is very difficult to perform HE shock experiments and thereafter recover the test samples at its exact shock prestrained state due to retained adiabatic heating and possible annealing effect even when the sample iswater quenched during a "soft" recovery test. Based on last phase of our study (mechanical property measurement and constitutive modeling) and current phase of investigation (validation using a Taylor cylinder impact test), it is recommended that the parameters of an annealed material be used initially (case *(b)* in Table 6 for the MTS model and Table 3 for the PTW model) for DU subjected to shock prestraining events or loading paths. During a shock and upon the release of that shock, the parameters should be ***reset*** to half of the calculated strains calculated from the EOS in the case of the PTW model or at 1% of the peak shock pressure as the mechanical threshold strength initialized in the MTS model before the next time increment of the calculation. In another words, the treatment shown in Fig. 4 and the simulation result shown in case (d) in Fig. 10 is thought to be the most accurate for simulating DU subjected to a shock event. Further study under other shock pressure(s) will be useful to check the validity of this simple approximation. The approach of characterizing the preshocked mechanical properties of DU and determination of a separate set of MTS or PTW model parameters with many variables unchanged is always more accurate (Table 4, Table 5, Figs. 9 and 10 (a)) and therefore it is encouraged that further shock prestraining experiments on DU be conducted. In addition to the 1-D planewave lens HE loading discussed in this report, quantification of the effect of sweeping wave shock prestraining on the post-shock mechanical behavior of DU is strongly recommended.

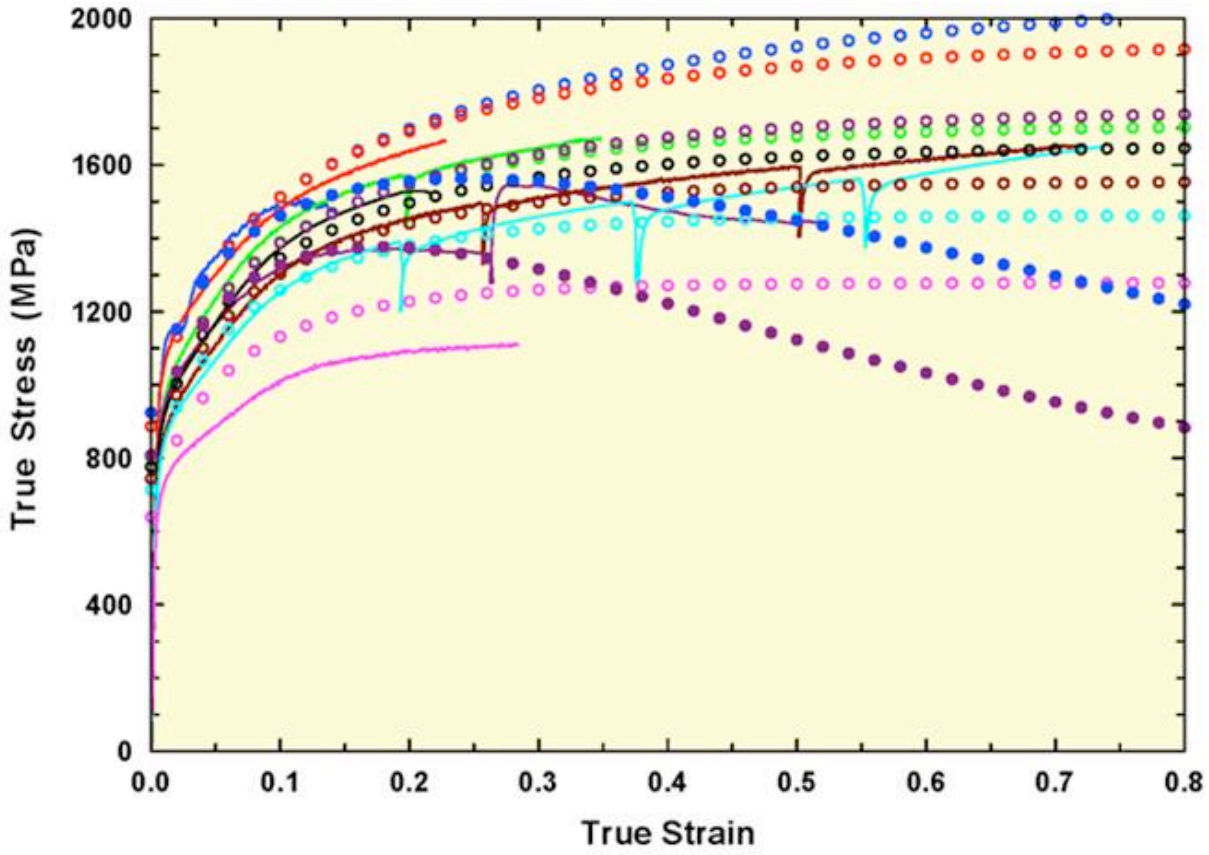

Fig. 6 Stress/strain responses and the PTW model fit (symbols) to DU shocked at 45 GPa.

Table 4 Nominal set of PTW model parameters for DU HE-shocked at 45 GPa

Parameter	Parameter Description	Nominal Value
θ_0	Initial strain hardening rate $(d\hat{\tau}/d\Psi)_{\psi=0}$	0.092
p	Constant modifying Voce hardening law	4
S_0	Maximum saturation stress (at 0K)	0.0135
S_∞	Minimum saturation stress (~ melting)	0.0020
κ	Constant in thermal activation energy term- relates to the temperature dependence	0.1
γ	Constant in thermal activation energy term- relates to the strain rate dependence	1.0×10^{-7}
y_0	Maximum yield stress (at 0K)	0.00575
y_∞	Minimum yield stress (~melting)	0.002
y_1	Material constant used in describing the high rate sensitivity in 2nd regime	0.0135
y_2	Material constant used in describing the high rate sensitivity in 2nd regime	0.27 (?)
β	Material constant used in describing the high rate sensitivity in 2nd regime	0.27 (?)
T_m	Melting temperature	1405 K
G_0	Shear modulus (at 0K)	107.8×10^9 N/m^2
α	Constant in G(T) Equation	0.89
C_v	Heat Capacity	140 J/Kg/K
A	Atomic weight	3.954×10^{-25} Kg/atom
ρ	Density	19050 Kg/m^3

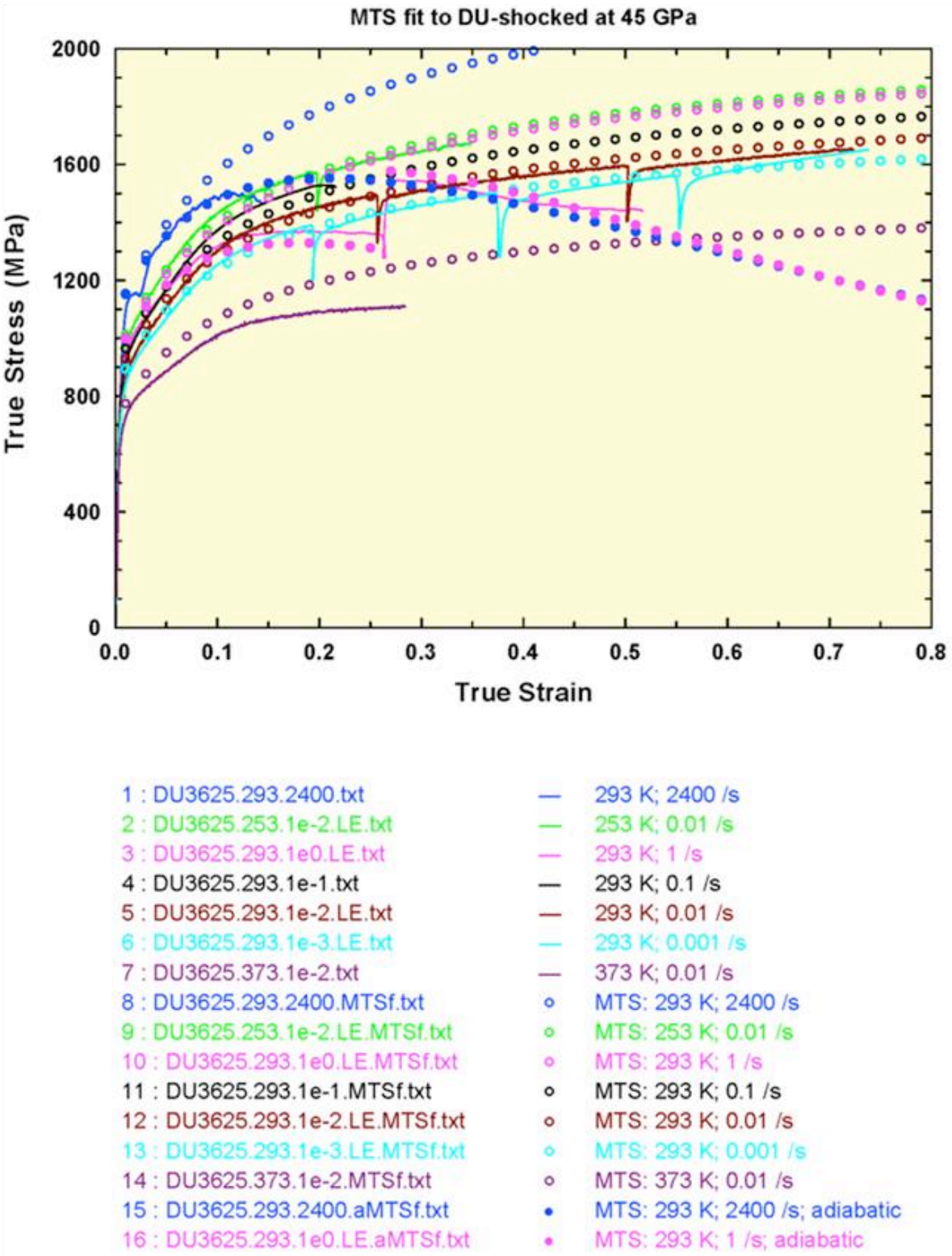

Fig. 7 Stress/strain responses and the MTS model fit (symbols) to DU shocked at 45 GPa.

Table 5 Equations and Parameters of a Depleted Uranium (thru-thickness compression) shocked at 45 GPa for the MTS Model

- $\frac{\sigma}{\mu} = \frac{\sigma_a}{\mu} + S_i(\dot{\varepsilon},T)\frac{\hat{\sigma}_i}{\mu_0} + S_\varepsilon(\dot{\varepsilon},T)\frac{\hat{\sigma}_\varepsilon}{\mu_0}$

  Where: σ_a = 40 MPa

- $\mu = \mu_0 - \frac{D_0}{\exp\left(\frac{T_0}{T}\right) - 1}$

  Where: μ_0 = 1.0672×10^5 MPa
  D_0 = 742.7 MPa
  T_0 = 10.93 K

- $S_i(\dot{\varepsilon},T) = \left\{1 - \left[\frac{kT}{\mu b^3 g_{0i}}\ln\left(\frac{\dot{\varepsilon}_{0i}}{\dot{\varepsilon}}\right)\right]^{1/q_i}\right\}^{1/p_i}$

  Where: k= 1.38×10^{-23} Joule/K
  b = 3×10^{-10} m
  $\dot{\varepsilon}_{0i}$ = 1×10^{7}s^{-1} q_i = 3/2
  p_i = 1/2 g_{0i} = 0.325
  $\hat{\sigma}_i$ = 1575 MPa

- $S_\varepsilon(\dot{\varepsilon},T) = \left\{1 - \left[\frac{kT}{\mu b^3 g_{0\varepsilon}}\ln\left(\frac{\dot{\varepsilon}_{0\varepsilon}}{\dot{\varepsilon}}\right)\right]^{1/q_\varepsilon}\right\}^{1/p_\varepsilon}$

  Where: $\dot{\varepsilon}_{0\varepsilon}$ = 1×10^7 s^{-1}
  g_0 = 1.6
  q = 1 p = 2/3

- $\frac{d\hat{\sigma}_\varepsilon}{d\varepsilon} = \hat{\theta}_0 \cdot \left[1 - \frac{\hat{\sigma}_\varepsilon}{\kappa \cdot \hat{\sigma}_{\varepsilon v}}\right]^{\kappa} = \hat{\theta}_0 \cdot \left[1 - \frac{\hat{\sigma}_\varepsilon}{\hat{\sigma}_{\varepsilon s}}\right]^{\kappa}$

  $\hat{\theta}_0 = A_0 + A_1 \cdot \ln\dot{\varepsilon} + A_2 \cdot \sqrt{\dot{\varepsilon}} - A_3 \cdot T$

  Where: κ = 2.5 (α = 2.27)
  A_0 = 12500 MPa
  A_1 = 0 MPa
  A_2 = 0 MPa
  A_3 = 3.5 MPa/K

- $\ln\left(\frac{\hat{\sigma}_{\varepsilon s}}{\hat{\sigma}_{\varepsilon s0}}\right) = \frac{kT}{\mu b^3 g_{0\varepsilon s}}\ln\left(\frac{\dot{\varepsilon}}{\dot{\varepsilon}_{0\varepsilon s}}\right)$

  Where: g_{0s} 0.082
  $\hat{\sigma}_{s0}$ 2175 MPa
  $\dot{\varepsilon}_{0\varepsilon s}$ = 1×10^7 s^{-1}

- $\Delta T = \frac{\Psi}{\rho C_p}\int\sigma(\varepsilon)d\varepsilon \quad when \quad \dot{\varepsilon} \geq 1s^{-1}$

  $C_p = C_{p0} + C_{p1}\cdot T + \frac{C_{p2}}{T^2}$

  Where: Ψ = 0.95
  ρ = 19.05 Mg/m^3
  C_{p0} = 0.14 J/g/K
  C_{p1} = 0 J/g/K^2
  C_{p2} = 0 J·K/g

Table 6 Equations and Parameters of a Depleted Uranium (thru-thickness compression) in several conditions for the MTS Model

- $\frac{\sigma}{\mu} = \frac{\sigma_a}{\mu} + S_i(\dot{\varepsilon},T)\frac{\hat{\sigma}_i}{\mu_0} + S_\varepsilon(\dot{\varepsilon},T)\frac{\hat{\sigma}_\varepsilon}{\mu_0}$

  Where: σ_a = 40 MPa

  $\hat{\sigma}_\varepsilon$ = 0 MPa [(b)]; = 800 MPa [(c)] ;

  = 450 MPa [(d)]

- $\mu = \mu_0 - \frac{D_0}{\exp\left(\frac{T_0}{T}\right) - 1}$

  Where: μ_0 = 1.0672×10^5 MPa

  D_0 = 742.7 MPa

  T_0 = 10.93 K

- $S_i(\dot{\varepsilon},T) = \left\{1 - \left[\frac{kT}{\mu b^3 g_{0i}}\ln\left(\frac{\dot{\varepsilon}_{0i}}{\dot{\varepsilon}}\right)\right]^{1/q_i}\right\}^{1/p_i}$

  Where: k= 1.38×10^{-23} Joule/K

  b = 3×10^{-10} m

  $\dot{\varepsilon}_{0i}$ = 1×10^{7}s^{-1}

  q_i = 3/2 p_i = 1/2

  g_{0i} = 0.625 $\hat{\sigma}_i$ = 925 MPa

- $S_\varepsilon(\dot{\varepsilon},T) = \left\{1 - \left[\frac{kT}{\mu b^3 g_{0\varepsilon}}\ln\left(\frac{\dot{\varepsilon}_{0\varepsilon}}{\dot{\varepsilon}}\right)\right]^{1/q_\varepsilon}\right\}^{1/p_\varepsilon}$

  Where: $\dot{\varepsilon}_{0\varepsilon}$ = 1×10^7 s^{-1}

  g_0 = 1.6

  q = 1 p = 2/3

- $\frac{d\hat{\sigma}_\varepsilon}{d\varepsilon} = \hat{\theta}_0 \cdot \left[1 - \frac{\hat{\sigma}_\varepsilon}{\kappa \cdot \hat{\sigma}_{\varepsilon v}}\right]^\kappa = \hat{\theta}_0 \cdot \left[1 - \frac{\hat{\sigma}_\varepsilon}{\hat{\sigma}_{\varepsilon s}}\right]^\kappa$

  $\hat{\theta}_0 = A_0 + A_1 \cdot \ln\dot{\varepsilon} + A_2 \cdot \sqrt{\dot{\varepsilon}} - A_3 \cdot T$

  Where: κ = 2.5 (α = 2.27)

  A_0 = 12500 MPa

  A_1 = 0 MPa

  A_2 = 0 MPa

  A_3 = 3.5 MPa/K

- $\ln\left(\frac{\hat{\sigma}_{\varepsilon s}}{\hat{\sigma}_{\varepsilon s0}}\right) = \frac{kT}{\mu b^3 g_{0\varepsilon s}}\ln\left(\frac{\dot{\varepsilon}}{\dot{\varepsilon}_{0\varepsilon s}}\right)$

  Where: g_{0s} 0.082

  $\hat{\sigma}_{s0}$ 2275 MPa

  $\dot{\varepsilon}_{0\varepsilon s}$ = 1×10^7 s^{-1}

- $\Delta T = \frac{\Psi}{\rho C_p}\int\sigma(\varepsilon)d\varepsilon \quad when \quad \dot{\varepsilon} \geq 1s^{-1}$

  $C_p = C_{p0} + C_{p1} \cdot T + \frac{C_{p2}}{T^2}$

  Where: Ψ = 0.95

  ρ = 19.05 Mg/m^3

  C_{p0} = 0.14 J/g/K

  C_{p1} = 0 J/g/K^2

  C_{p2} = 0 J·K/g

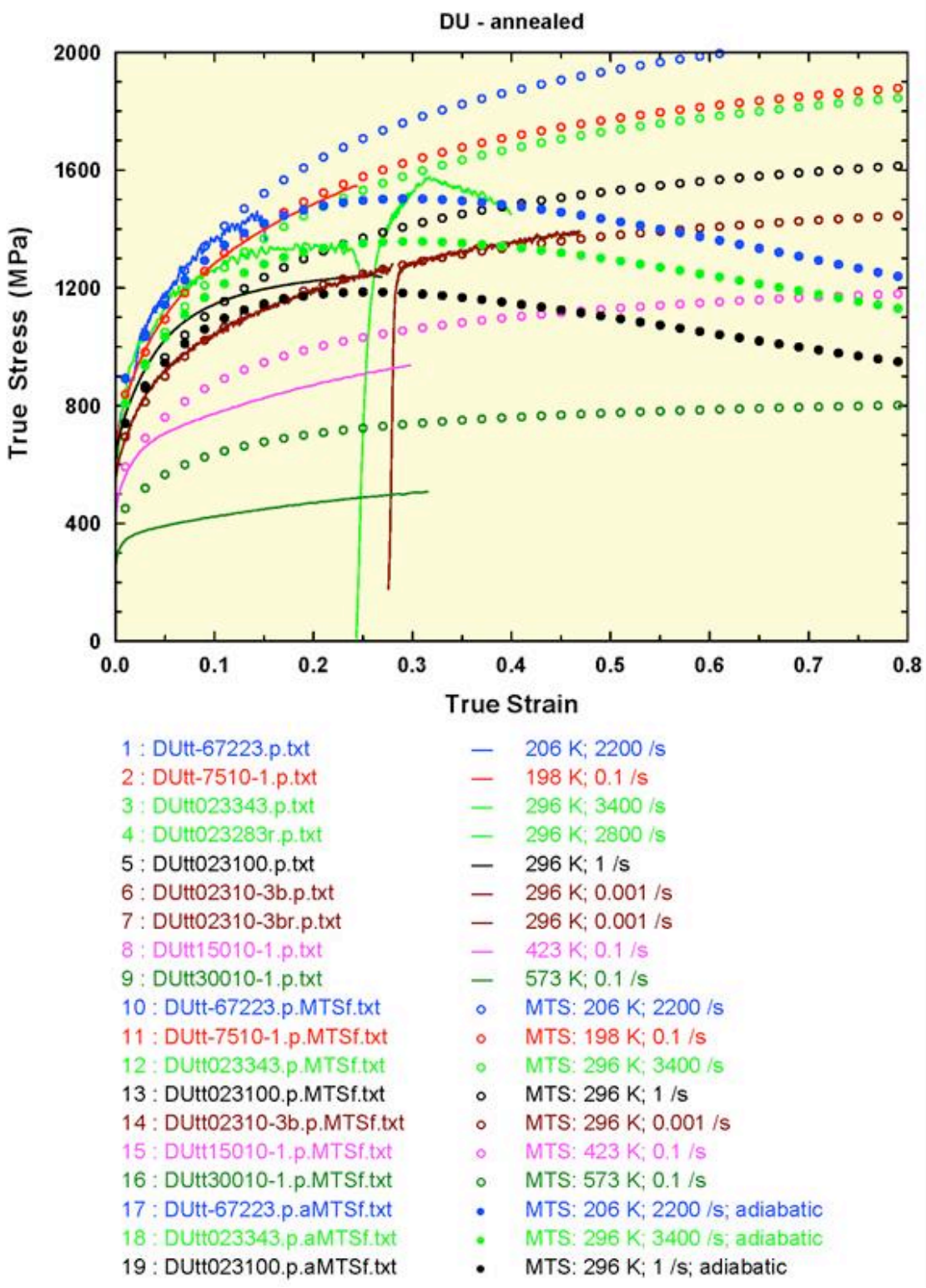

Fig. 8 Stress/strain responses and the MTS model fit (symbols) to DU.

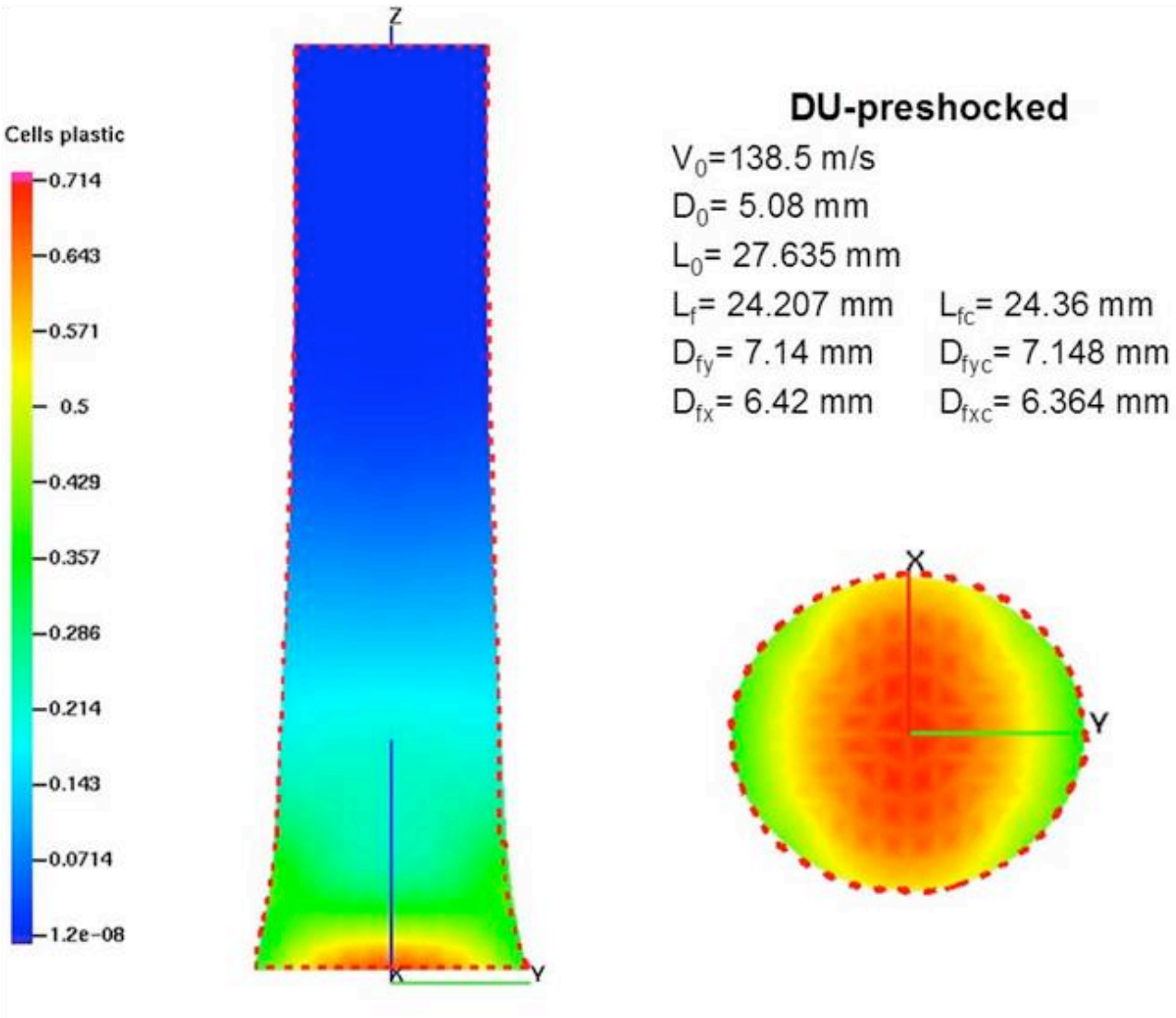

Fig. 9 Taylor cylinder impact test, experiment (dashed lines) and calculations (color shades).

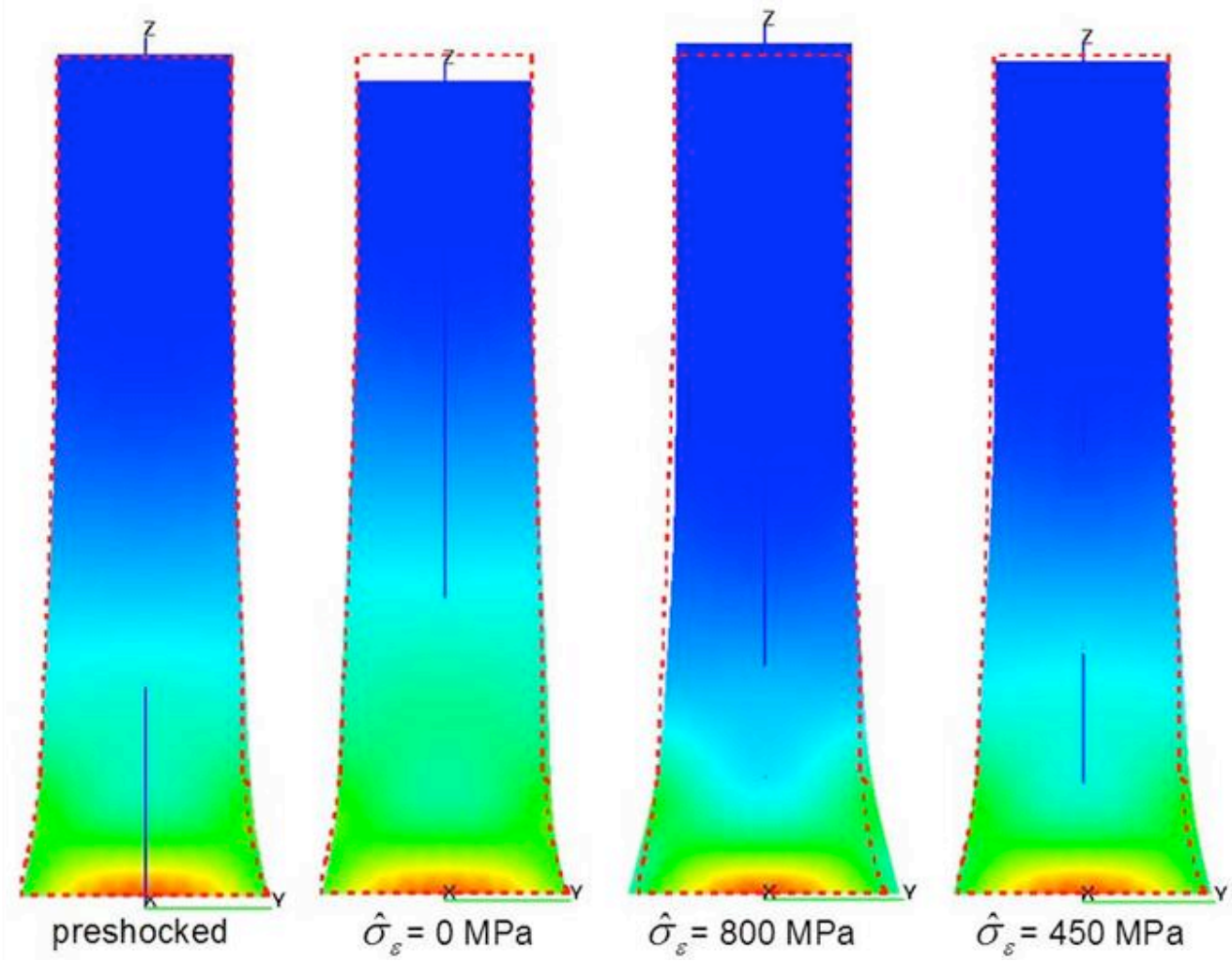

Fig. 10 Taylor cylinder impact test, experiment (dashed lines) and calculations (color shades).

Section 9: Mechanical Behavior of DU Screws/Bolts

Material:

The starting material used in DU screws / bolts is high purity DU metal that was cast into a large rolling billet (< 100 ppm C). The billet was hot rolled into ~1 inch plate, sawed into 1 inch square strips, machine turned to ~0.8125 inch dia. round rod. The rods were then vacuum annealed for 17 hours. Thereafter the rods were swaged into ~3/8 inch diameter rod stock. Typically, the swaging passes utilized ~10% area reduction per pass with one intermediate anneal after about the first 50% cold work. The intent was to leave ~55% cold work in the final bar product. The rod stock was then radiographed and tensile (not compression) tested, and last of all, the stock was machined into screws / bolts. Even very old DU screws / bolts were made using the same processing processes, however the % cold work may have been more variable and less controlled in the earlier screws/bolts.

Figures 1-4 present the tensile stress-strain behavior the DU bolt material as a function of temperature from -54, -21, 0, and 75°C for tensile testing at strain rates of 0.001/sec and 1/sec. Figure 5 presents compression data for a specific lot of DU bolt material as a function of temperature and strain rate. The difference in shape in the stress-strain curves evident between compression and tensile loading is consistent with differences in the activation of dislocation slip and deformation twinning. The concave-down shape to the tensile curves is consistent with plasticity principally dominated by dislocation glide in contrast to the initially concave-upward stress-strain curves that are classically an indication of the early activation of deformation twinning in addition to dislocation slip. Crystallographic texture effects are well known to be the cause of such pronounced alterations in the flow-stress response of DU as a function of loading stress-state and textural loading orientation.[Reference 1].

References:

[1] G.T. Gray III: Annual Review of Materials Research, (2012), vol. 42, pp. 285-303. [Invited Review]; "High-Strain-Rate Deformation: Mechanical Behavior and Deformation Substructures Induced"

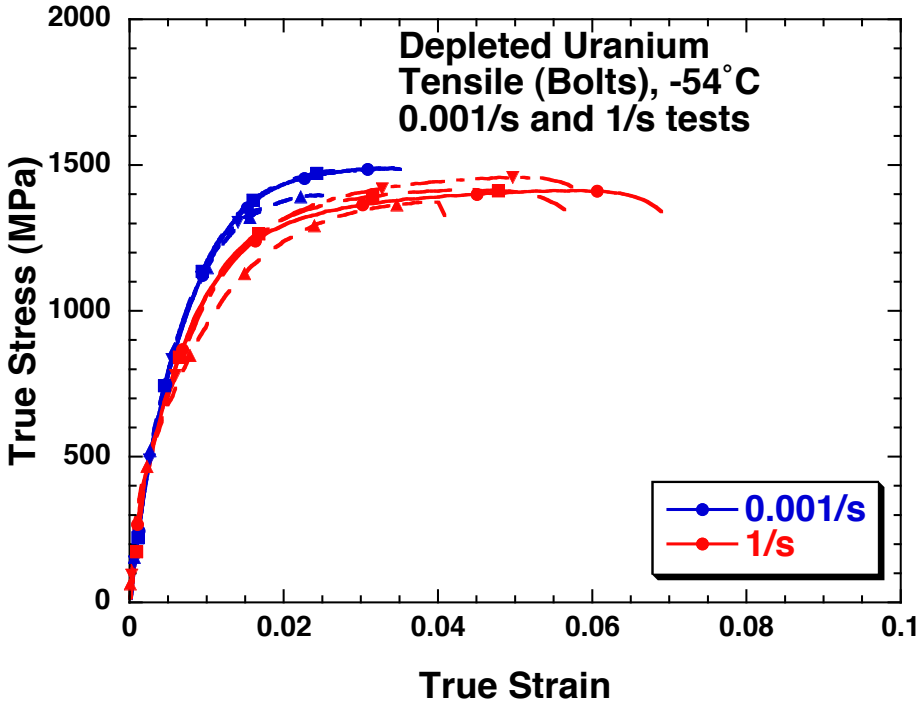

Figure 1: Tensile Stress-Strain Response of DU bolts tested at -54°C at 0.001/sec and 1/sec

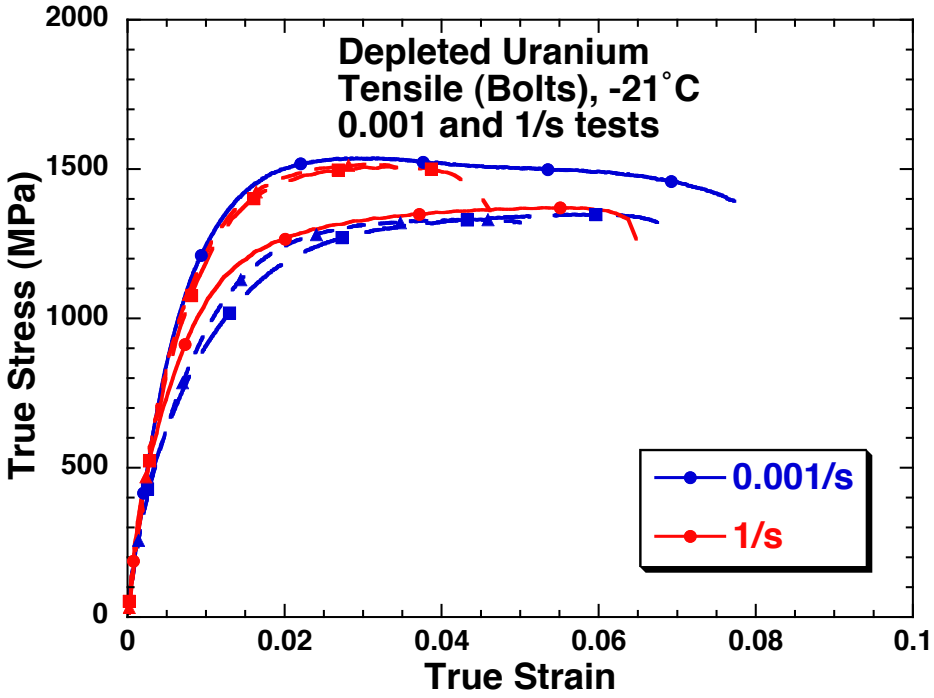

Figure 2: Tensile Stress-Strain Response of DU bolts tested at -21°C at 0.001/sec and 1/sec

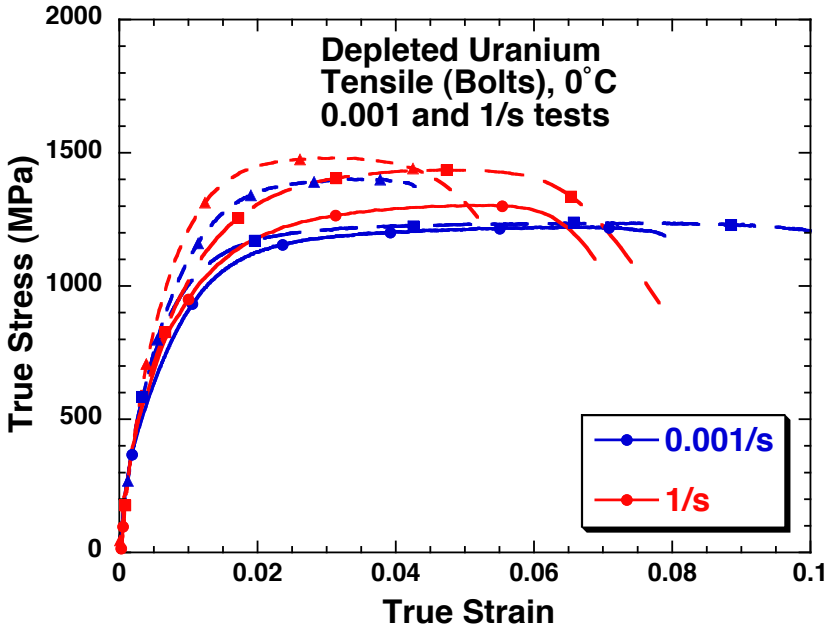

Figure 3: Tensile Stress-Strain Response of DU bolts tested at -0°C at 0.001/sec and 1/sec

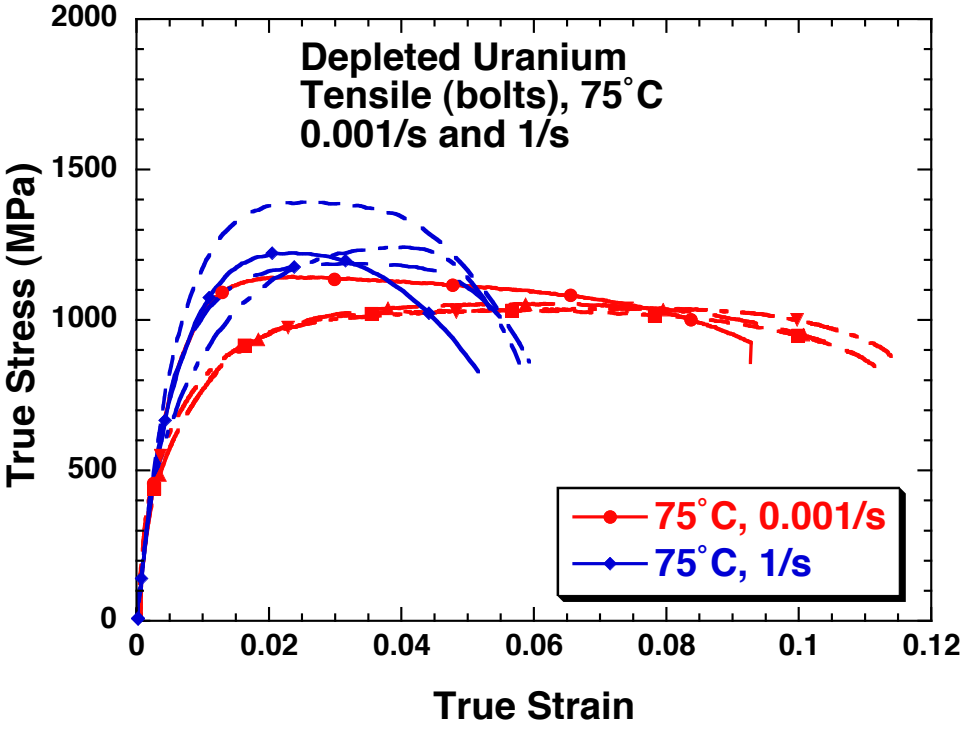

Figure 4: Tensile Stress-Strain Response of DU bolts tested at -75°C at 0.001/sec and 1/sec

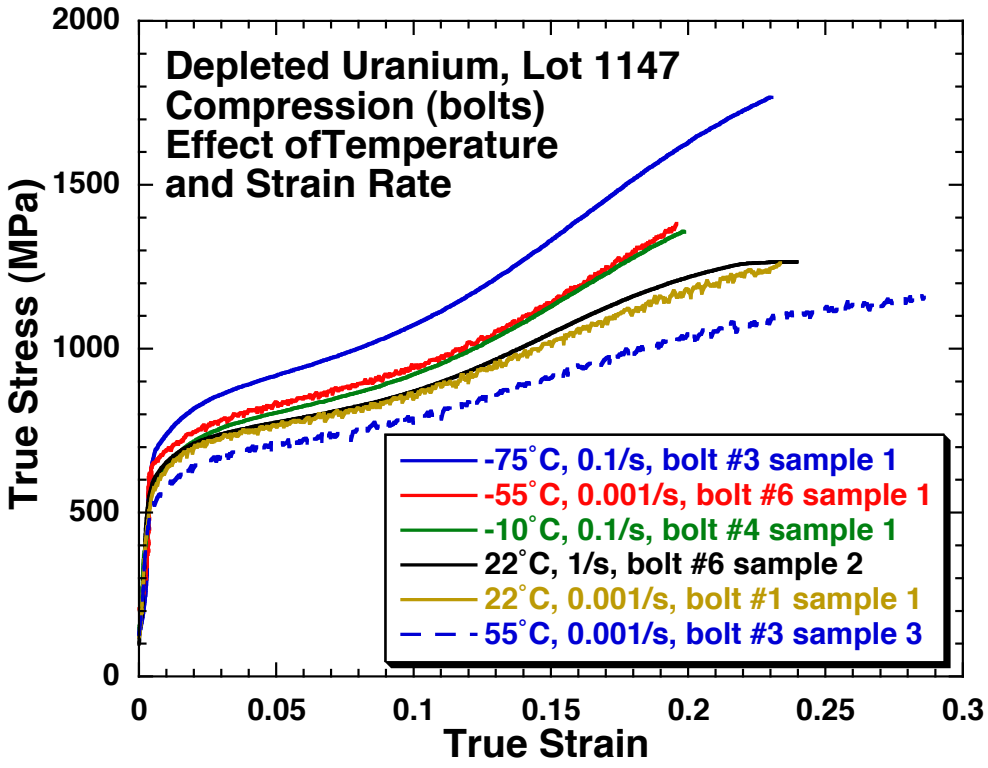

Figure 5: Compressive Stress-Strain Response of DU bolts (lot # 1147) as a function of temperature and strain rate.

Section 10: Modeling of Damage and Failure in Depleted Uranium

Progress in Modelling of Damage and Failure in Dynamically Loaded Depleted Uranium (DU-238)

C. A. Bronkhorst, G. T. Gray III, S.-R. Chen, D. Dennis-Koller,
C. Cady, E. K. Cerreta, D. J. Luscher, F. L. Addessio, M. W. Schraad

Introduction

The large deformation, damage and failure process for many polycrystalline metallic materials is inherently ductile in nature. In general this means that the material will choose four specific physics mechanisms for accommodation of the imposed deformation – solid-solid phase transformation, large deformation plasticity, shear localization or adiabatic shear banding, and cavitation. This discussion at present restricts itself to the materials and physics in this class of behavior. At present, materials models to represent this damage process contain the elements of pore initiation or nucleation, pore growth, pore coalescence, and ultimate failure. The nucleation process is believed to depend heavily on microstructural based heterogeneities and the spatial distribution of defects. These include grain boundaries, impurity inclusions, intersection of twin planes, and dislocation sub-cells. The statistical spatial distribution of inherent (grain boundaries, inclusions, initial dislocations) or deformation induced heterogeneities (twinning, dislocation subcell) are believed to act in combination with the spatial and temporal intensity of loading to determine which of the weakest or most strongly loaded defect sites will initiate a pore. A nucleated field of pores will then competitively grow in size until they become large enough such that the deformation field surrounding individual pores begins to overlap with neighboring pores – at which time the process of damage coalescence begins. The coalescence phase is when the established pore field begins to join and when localization or adiabatic shear banding facilitates this process. Of course, ultimate failure will occur when the coalescence process brings about a percolated region of damage. For dynamic and shock loading conditions, these events occur within very small length and time spans and so velocities and accelerations are very large. Therefore, in addition to spatial effects, local inertial effects must also be accounted for in materials of moderate to high density. This process is extremely complex, statistical and inherently loading path/rate dependent and so we need new tools to be able to understand the three-dimensional link between the defect structure / microstructure and detailed loading characteristics. This work reports on the TEPLA model parameterization for annealed depleted uranium and comments on several needed improvements.

Experimental

Three experiments were performed on annealed depleted uranium using configurations to allow for soft capture of the specimen (experiments 56-11-33 (285 m/s), 56-11-34 (287 m/s), 56-11-38 (439 m/s); Dennis-Koller, 2009, 2011; Gray et al., 2006). Hopkinson pressure bar testing for uniaxial compression experiments to evaluate plastic flow resistance model parameters and notched tensile testing was also performed in order

to evaluate the relationship between stress triaxiality and failure strain (Gray, 2007; Chen and Gray, 2009). Results from this work will be used here and will be presented in the context of parameter evaluation for the existing TEPLA model. Fig. 1 is a schematic of the experimental configuration and numerical model used to represent the three shots used to evaluate parameters here. The flyer plate material for the three plate impact experiments was chosen as Z-cut quartz. Geometric details of the three experiments are given in Table 1.

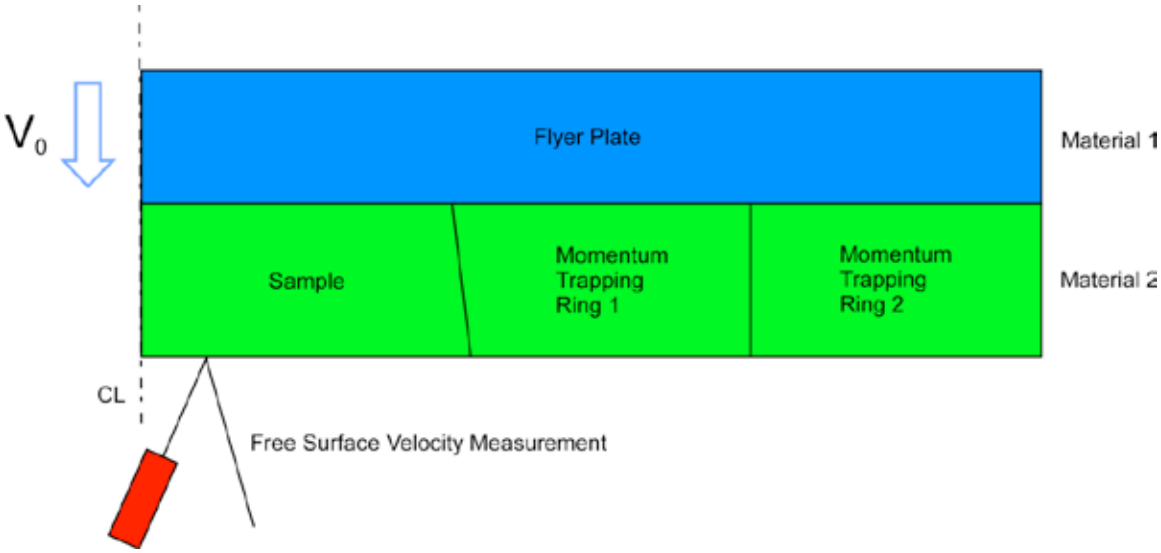

Fig. 1. Schematic representation of the axi-symmetric flyer plate experiment and model. Material 1 is the z-cut quartz flyer while material 2 is depleted uranium. The sample is contained within two momentum trapping rings – also depleted uranium.

Experiment	Impactor Thickness, mm	Impactor Velocity, m/s	Target Thickness, mm	Peak Pressure, GPa
56-11-33	3.065	285	2.487	3.699
56-11-34	3.062	287	2.494	3.726
56-11-38	3.062	439	2.515	5.831

Table 1. Three plate impact experiments performed on annealed depleted uranium samples used for material parameter evaluation in this report (Dennis-Koller, 2009, 2011).

The free surface velocity traces for the three experiments listed in Table 1 are given together in Fig. 2. Clearly the repeatability between the two lower velocity experiments are very good and may be considered to be the same experiment and therefore we will restrict ourselves to the use of results from experiments 56-11-34 and 56-11-38. These are classic velocimetry traces with both the high and low velocity profiles suggesting the same Hugoniot elastic limit based upon the load-up inflection in the traces.

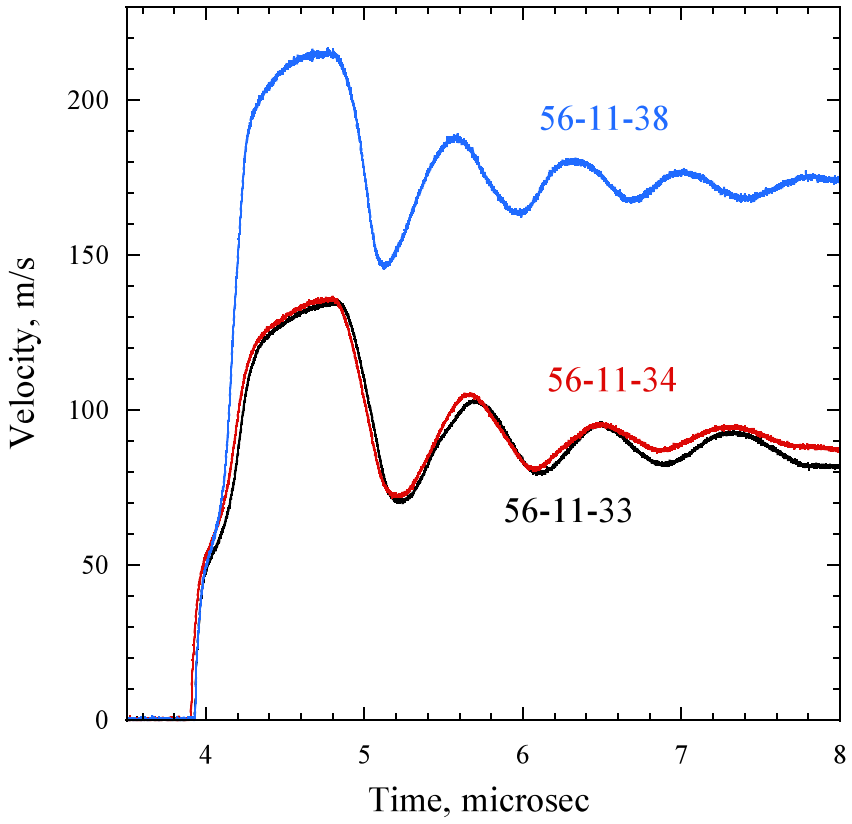

Fig. 2. Free surface velocity traces for the three annealed depleted uranium experiments considered in this report.

Metallographic images of the cross-section of the recovered samples from tests 56-11-34 and 56-11-38 were produced (Cerreta, 2012) and are given in Figs. 2 and 3 respectively. The notable difference between the two experiments were that sample 56-11-34 did not achieve complete failure and clear evidence of damage due to grain boundary failure was evident. Sample 56-11-38 did completely fail since the impact velocity was much greater. We will re-visit these points later in this document as this has important physical implications on the theory.

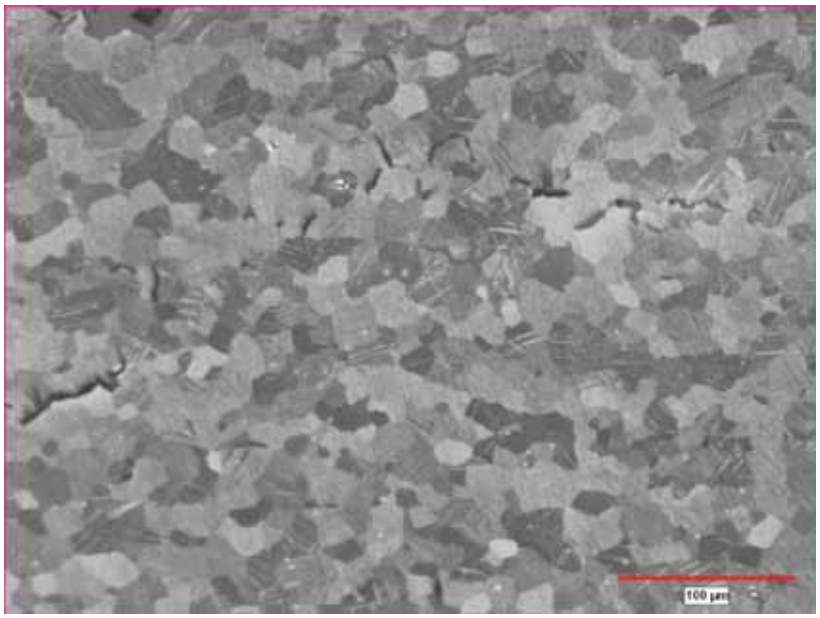

Fig. 3. Metallographic image of a region of the cross-section of sample 56-11-34 showing incipient damage.

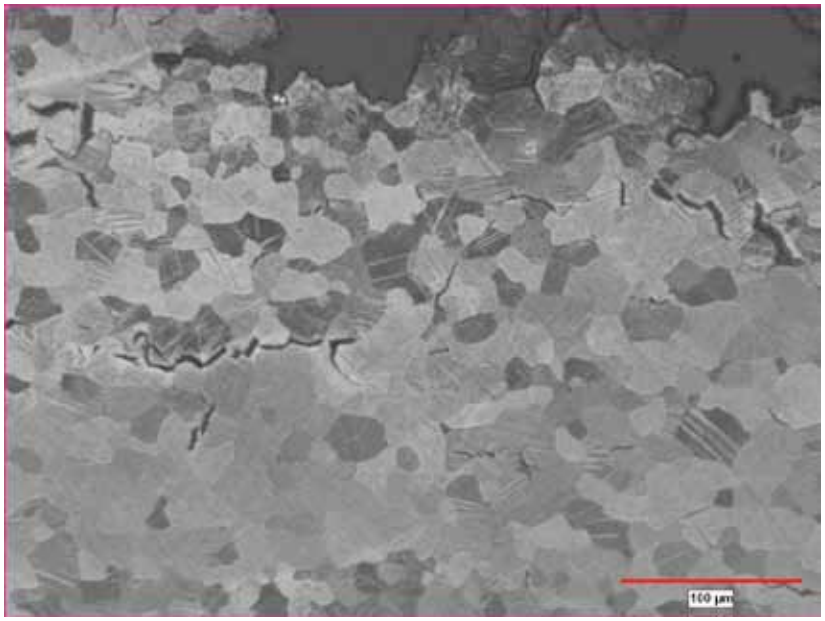

Fig. 4. Metallographic image near the failure surface in the cross-section of sample 56-11-38.

Numerical Models

The numerical simulations reported upon here were performed with EPIC06. All simulations are two-dimensional axi-symmetric and the element size within the sample is targeted to be 25 μm. The element size within the flyer plate and momentum trapping

rings is something on the order of a factor of 2-3 larger. A sample element size of 25 μm was chosen based upon prior work on the modeling of damage in supported shock wave configurations. All elements in the models are the crossed triangular configuration. Frictionless slide lines are at the interface between the flyer plate and the sample and two momentum trapping rings as well as between the sample and the two momentum trapping rings. A contour plot of the pressure within the assembly at a time of 1.5 μs after first contact is given in Fig. 2. The contour plot clearly shows the isolation between the sample and momentum trapping rings as well as the unloading in the center of the sample layer caused by the damage of the material.

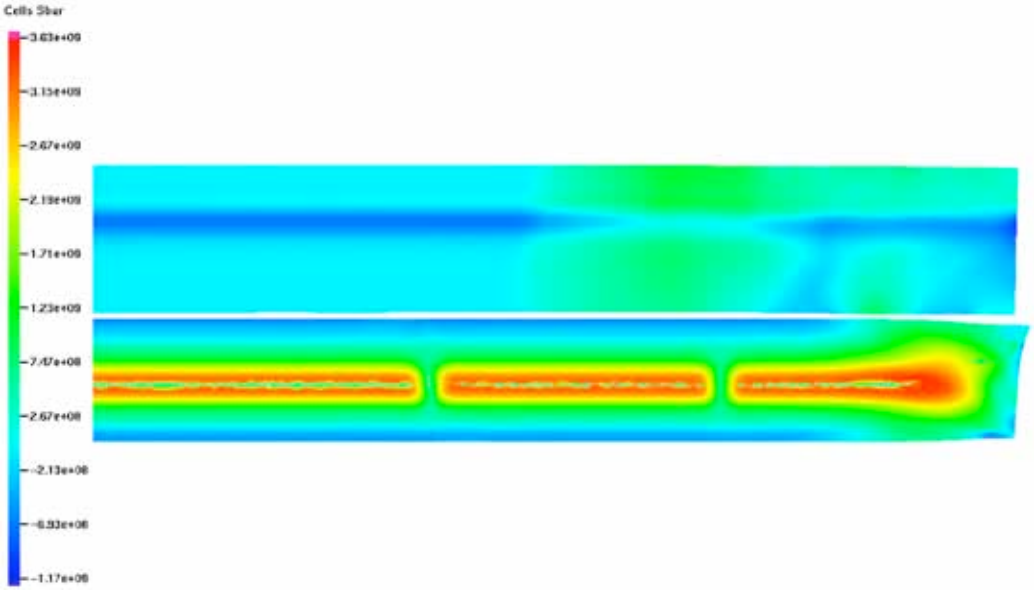

Fig. 5. Pressure in the sample assembly at a time of 1.5 μs after flyer contact with the sample. The sample and two momentum trapping rings are seen isolated as well as unloading near the center of the sample layer due to damage. The unit of pressure is Pa.

Constitutive Model

The constitutive model used is from the work of Addessio and Johnson (1993), Maudlin et al. (1999a,b) and Maudlin et al. (2003). The model is summarized here.

The Cauchy stress in the damaged state is given by

$$\mathbf{T} = \underline{\mathbf{M}}\tilde{\mathbf{T}}, \qquad (1)$$

where the stress in the undamaged material is $\tilde{\mathbf{T}}$ and the fourth rank isotropic damage tensor defined in relationship to porosity ϕ is given by

$$\underline{\mathbf{M}} = (1-\phi)\underline{\mathbf{I}}. \qquad (2)$$

Time integration is performed in the material frame relative to the laboratory frame defined by the rotation $\mathbf{R}$ given by the polar decomposition

$$\mathbf{F} = \mathbf{RU} = \mathbf{VR}\,. \qquad (3)$$

The material time rate for the Cauchy stress is given by

$$\dot{\mathbf{T}} = \underline{\mathbf{M}}\underline{\tilde{\mathbf{L}}}'(\mathbf{D}' - \mathbf{D}^{p'}) + \underline{\mathbf{M}}\left(\frac{\rho_0}{\tilde{\rho}}\tilde{K}_s \mathrm{tr}\mathbf{D}^e - \frac{\tilde{\rho}}{\rho}\Gamma\mathbf{T}\cdot\mathbf{D}^p\right)\underline{\mathbf{I}} + \dot{\underline{\mathbf{M}}}\underline{\mathbf{M}}^{-1}\mathbf{T} \qquad (4)$$

where $\tilde{\mathbf{L}}$ is the fourth order elasticity tensor, $\tilde{K}_s$ is the isentropic bulk modulus, Γ is the Gruneisen coefficient and

$$\mathbf{L} = \mathbf{M}\tilde{\mathbf{L}}\mathbf{M} \qquad (5)$$

The rate of deformation is additively decomposed as

$$\mathbf{D} = \mathbf{D}^e + \mathbf{D}^p = \mathbf{D}^e + (\mathbf{D}^d + \mathbf{D}^{p'})\,, \qquad (6)$$

where the plastic contribution to deformation is separated into spherical and deviatoric components. The contribution due to damage is given by

$$\mathbf{D}^d = \frac{\dot{\varphi}}{3(1-\varphi)}\mathbf{1}\,, \qquad (7)$$

where the scalar quantity ϕ represents damage as porosity (Addessio and Johnson, 1993).

The flow rule is given by

$$\mathbf{D}^p = \frac{1}{\tau_r}(\mathbf{T} - \mathbf{T}^{proj})\,. \qquad (8)$$

In general we allow the stress state to reside off the yield surface during plastic deformation. The over-stress model of Eq. (8) uses a relaxation coefficient τ_r with the tensorial quantity $\mathbf{T}^{proj}$ being the stress state on the yield surface corresponding to the current Cauchy stress projected back onto the plastic flow surface by radial return. The relationship used to define the relaxation coefficient is

$$\tau_r = \eta\left(\frac{1-\phi_0}{\phi_0}\right)^{\frac{2}{3}}\left(\frac{1-\phi}{\phi}\right)^{\frac{1}{3}}\,, \qquad (9)$$

where $\eta = 10^{-6}\ \ 1/\mathrm{Pa}\cdot\mathrm{s}$.

The plastic flow surface utilized here is that developed by Gurson (1977) and later modified by Tvergaard (1981, 1982), Tvergaard and Needleman (1984), and Maudlin et al. (2003) is given by

$$\tau - \sigma_f(\dot{\bar{\varepsilon}}_p, \theta)^2 \left[1 + q_3\varphi^2 - 2q_1\varphi\cosh\delta\right] = 0 \qquad (10)$$

where

$$\tau = \frac{1}{2}\mathbf{T}'\boldsymbol{\alpha}\underline{\mathbf{T}}\ \ ', \qquad (11)$$

is a quadratic relationship allowing for plastic anisotropy, $\sigma_f(\dot{\bar{\varepsilon}}_p, \theta)$ is the rate and temperature sensitive flow stress and

$$\delta = -\frac{3q_2\tilde{P}}{2\sigma_s}, \qquad (12)$$

where

$$\tilde{P} = -\tfrac{1}{3}\mathrm{tr}\tilde{\mathbf{T}}\ . \qquad (13)$$

The quantities q_1, q_2, and q_3 are material parameters and the saturation flow stress σ_s is defined below (described below Eq. (26)).

A polynomial Mie-Gruneisen equation of state is used

$$\widetilde{P} = (K_1\widetilde{\beta} + K_2\widetilde{\beta}^2 + K_3\widetilde{\beta}^3)(1 - \Gamma\widetilde{\beta}/2) + \Gamma\widetilde{E}_s(1 + \widetilde{\beta}) \qquad (14)$$

where

$$\tilde{\beta} = \frac{\tilde{\rho}}{\tilde{\rho}_0} - 1\ , \qquad (15)$$

$$\rho = \left(1 - \phi\right)\tilde{\rho}\,, \qquad (16)$$

$$\dot{\tilde{E}}_s \equiv (\bar{\sigma}\dot{\bar{\varepsilon}}_p - P\mathrm{tr}\mathbf{D})\frac{\rho_0}{\tilde{\rho}}, \qquad (17)$$

$$\bar{\sigma} = \sqrt{\tfrac{3}{2}\mathbf{T}'\cdot\mathbf{T}'}\ , \qquad \dot{\bar{\varepsilon}}_p = \sqrt{\tfrac{2}{3}\mathbf{D}^{p'}\cdot\mathbf{D}^{p'}}\ . \qquad (18)$$

K_1, K_2, and K_3 are polynomial coefficients; Γ is the Gruneisen coefficient and $\tilde{E}_s$ is the internal energy. The quantity $\tilde{\rho}$ is the current density of the undamaged material.

A model of the failure of the material is defined by

$$F = \left(\frac{\phi}{\phi_f}\right)^2 + \left(\frac{\bar{\varepsilon}_p}{\gamma_f}\right)^2 \geq 1 \qquad (19)$$

where ϕ_f is the failure porosity and

$$\gamma_f = \gamma_0 + \gamma_1 e^{\gamma_2 \frac{p}{\tau}}, \qquad (20)$$

is the relationship defining the failure value of the equivalent strain.

The strain rate and temperature sensitivity of the plastic deformation response is represented through the flow stress. We employ here the isotropic mechanical threshold strength (MTS) model, which has been well established for many materials and is due to the work of Follansbee and Kocks (1988), Chen and Gray (1996). The MTS model is based on the concept of a superposition of resistances to the glide of dislocations. Generally they are grouped as athermal barriers (e.g. grain boundaries) and thermally influenced barriers (e.g. Peierls stress – intrinsic lattice resistance, forest dislocations, dislocation structure, solute atoms). The mechanical threshold strength is the deformation resistance at 0 K. The flow stress used here is that stress adjusted to current temperature and strain rate. The reader is referred to Follansbee and Kocks (1988) and Chen and Gray (1996) for more details.

The relationship for flow stress is given by

$$\sigma_f(\dot{\bar{\varepsilon}}_p, \theta) = \sigma_a + \frac{\mu}{\mu_0}(S_i(\dot{\bar{\varepsilon}}_p, \theta)\hat{\sigma}_i + S_\varepsilon(\dot{\bar{\varepsilon}}_p, \theta)\hat{\sigma}_s), \qquad (21)$$

where σ_a is the constant athermal resistance, $\hat{\sigma}_i$ is the constant intrinsic lattice resistance at 0 K and $\hat{\sigma}_\varepsilon$ is the resistance due to dislocation structure at 0 K which evolves with deformation. The relationship for shear modulus as a function of temperature is given as

$$\mu = \mu_0 - \frac{D_0}{\exp\left(\frac{\theta_0}{\theta}\right) - 1}, \qquad (22)$$

which was first proposed by Varshni (1970). The rate and temperature kinetics are represented by the two pre-multiplying terms

$$S_i(\dot{\bar{\varepsilon}}_p,\theta)=\left(1-\left[\frac{k\theta}{\mu b^3 g_{0i}}\ln\left(\frac{\dot{\varepsilon}_{0i}}{\dot{\bar{\varepsilon}}_p}\right)\right]^{1/q_i}\right)^{1/p_i}, \qquad (23)$$

and

$$S_\varepsilon(\dot{\bar{\varepsilon}}_p,\theta)=\left(1-\left[\frac{k\theta}{\mu b^3 g_{0\varepsilon}}\ln\left(\frac{\dot{\varepsilon}_{0\varepsilon}}{\dot{\bar{\varepsilon}}_p}\right)\right]^{1/q_\varepsilon}\right)^{1/p_\varepsilon}, \qquad (23)$$

where $\dot{\bar{\varepsilon}}_p$ is the equivalent plastic strain rate, *k* is Boltzmann's constant, *b* is the magnitude of the Burgers vector, g_0 are normalized activation energies, $\dot{\varepsilon}_0$ are reference strain rates and *p* and *q* are exponents, which determine the shape of the energy barrier profile. Kocks et al. (1975) suggest that $p\in[0,1]$ and $q\in[1,2]$.

The resistance due to the evolution of the dislocation structure changes with strain as

$$\frac{d\hat{\sigma}_\varepsilon}{d\varepsilon_p}=h_0\left(1-\frac{\hat{\sigma}_\varepsilon}{\hat{\sigma}_{\varepsilon s}}\right)^\kappa, \qquad (25)$$

where the saturation stress as a function of rate and temperature is given by (Kocks, 1976)

$$\hat{\sigma}_{\varepsilon s}=\hat{\sigma}_{\varepsilon s_0}\left(\frac{\dot{\bar{\varepsilon}}_p}{\dot{\varepsilon}_{0_{\varepsilon s}}}\right)^{\frac{k\theta}{\mu b^3 g_{0_{\varepsilon s}}}}. \qquad (26)$$

The saturation stress σ_s used in Eq. (12) is taken as the current value of the flow stress given by Eq. (21) with the quantity $\hat{\sigma}_\varepsilon$ replaced by its saturation value $\hat{\sigma}_{\varepsilon s}$ given by Eq. (26).

The local mechanical work done to the material changes the local temperature by the following relationship

$$\dot{\theta}=\frac{1}{\rho C_p}\dot{\tilde{E}}_s. \qquad (27)$$

where $\tilde{E}_s$ is the internal energy in the undamaged material and is given by Eq. (17).

Equation of State and Failure Surface Representation

In this work the stresses achieved are believed to be low enough to assume that no plastic deformation has occurred in the Z-cut quartz material. We have also assumed that the quartz can be taken as an isotropic material which can be represented simply by an isotropic equation of state of the form

$$P = \frac{\rho_0 C S^2 \eta}{(1 - S\eta)^2}\left(1 - \frac{\Gamma\eta}{2}\right) + \Gamma E_s \qquad (28)$$

Where C is the bulk sound velocity, S is the $U_s - U_p$ slope, Γ is the Gruneisen parameter, ρ_0 is the initial density, and $\eta = 1 - \rho_0 / \rho$. The values for z-cut quartz used were $\rho_0 = 2649$ kg/m^3, C = 6360 m/s, S = 1.36, and Γ = 1.35 (Hicks et al., 2005; Jaglinski et al., 2009; Luo et al., 2002a,b; Duvall et al., 1967; Thurston et al., 1966; Wackerle, 1962; McSkimin et al., 1965). In practice the calculations indicated using C values which were lower than indicated above which was arrived at experimentally. This issue is attributed to the need to model the single crystal quartz (trigonal crystal symmetry) as an anisotropic single crystal as Johnson et al. have found in their previous work with Y-cut quartz (Johnson, 1968, 1971; Johnson et al., 1999). The isotropic representation of single crystal quartz used here is believed to be inadequate to represent the shock response of the material – even in the regime of loading which avoids plastic deformation of quartz.

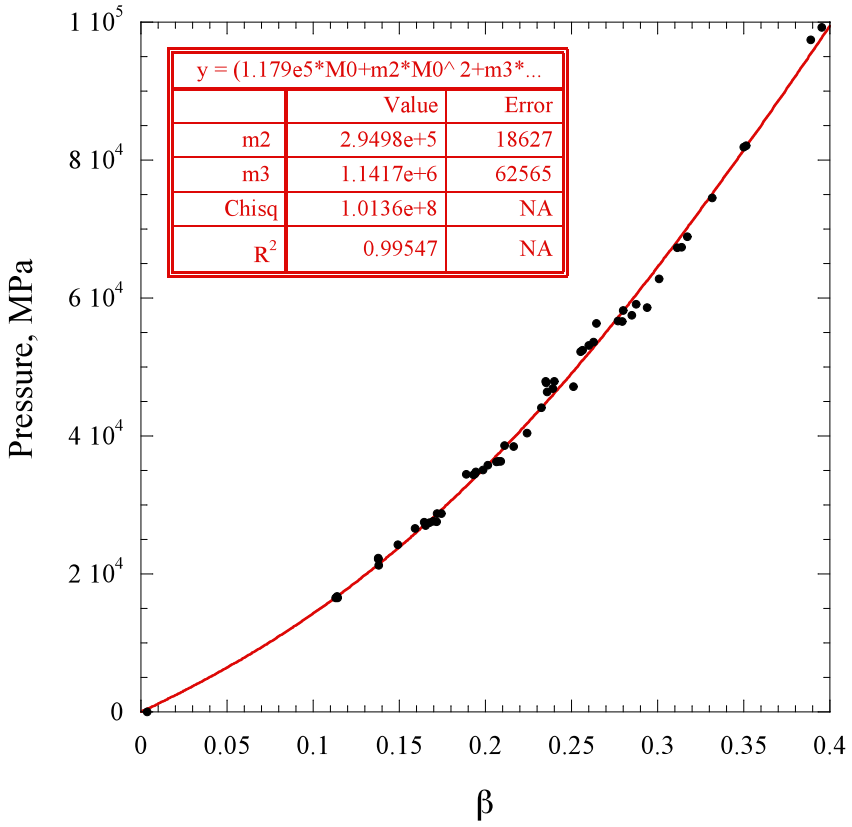

Fig. 6. Hugoniot data of Marsh (1980) representation by the polynomial equation of state for depleted uranium (Eqs. 14 and 15).

For depleted uranium, the material parameters for the equation of state given in Eqs. (14) and (15) are $K_1 = 117.9$ GPa , $K_2 = 294.98$ GPa (= 0 for hydrostatic tensile loading), $K_3 = 1141.7$ GPa (= 0 for hydrostatic tensile loading), $\Gamma = 2.03$, and $\tilde{\rho}_0 = 18{,}930$ kg/m^3 . This gives a representation of the Marsh data as demonstrated in Fig. 6.

The MTS model annealed depleted uranium parameters for Eqs. (21) – (27), the rate and temperature sensitive flow stress are given in Table 2.

Parameter	**DU**
μ_0	106.72 GPa
D_0	742.7 MPa
θ_0	10.93 K
σ_a	40 MPa
$\hat{\sigma}_i$	925 MPa
initial $\hat{\sigma}_\varepsilon$	0 MPa
b	3.00 Å
g_{0i}	0.625
$g_{0\varepsilon}$	1.6
$\dot{\varepsilon}_{0i} = \dot{\varepsilon}_{0\varepsilon} = \dot{\varepsilon}_{0_{es}}$	10^7 s^{-1}
p_i	½
q_i	3/2
p_ε	2/3
q_ε	1
h_0	12.5 GPa
κ	2.5
$\hat{\sigma}_{\varepsilon s_0}$	2275 MPa
$g_{0_{es}}$	0.082
C_p	113 J/kg-K
ρ_0	19050 kg/m^3

Table 2. Depleted uranium material parameter values for the MTS model given in Eqs. (21) – (27).

The failure surface parameters for Eqs. (19) and (20) evaluated for annealed depleted uranium are given by , $\gamma_0 = 0.08$, $\gamma_1 = 0.665$, $\gamma_2 = 1.929$, and $\phi_f = 0.3$. These parameters were evaluated from notched bar tension and plate impact experiments and this relationship is given relative to that data in Fig. 7 below.

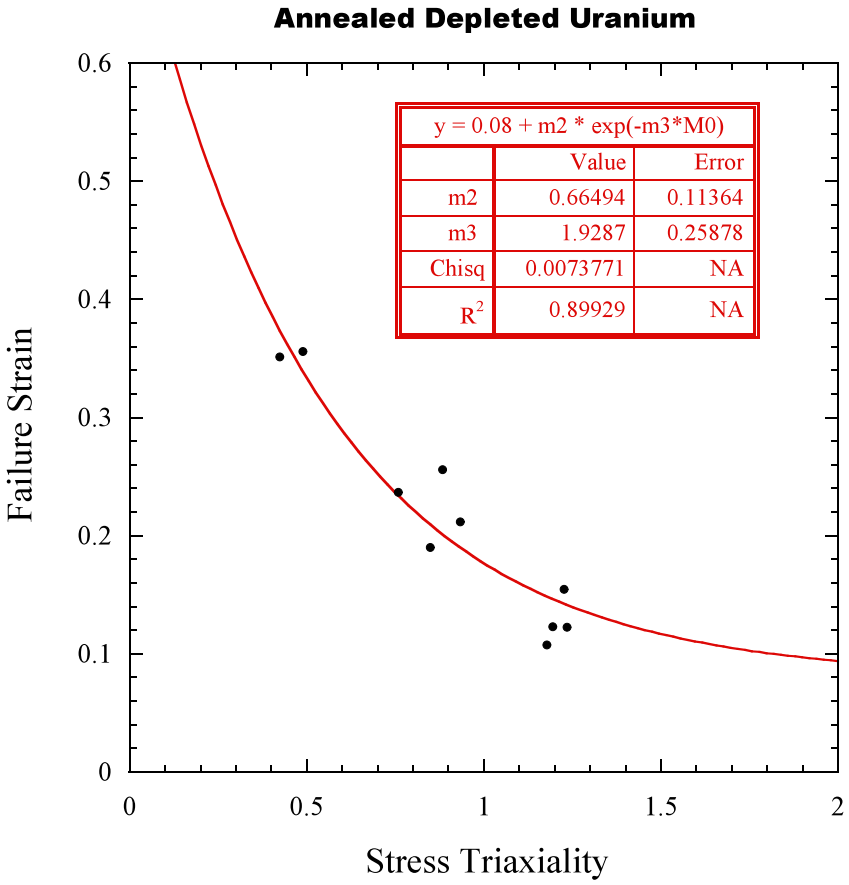

Fig. 7. Annealed depleted uranium failure surface parameter evaluation against notched tension data.

Gurson Surface Parameter Evaluation and Simulation Results

As mentioned above, the isotropic model used to represent the shock response of Z-cut quartz is not adequate and the work by Johnson et al. mentioned above suggests that a single crystal model is necessary. Since this was not possible in the short term (we are presently working on a finite elasticity single crystal model), we elected to match the peak experimental velocity of each experiment by reducing the bulk wave speed used in the equation of state (Eq. 28) for quartz. Using a bulk wave speed of 6360 m/s produced results which significantly over-predicted the peak velocity and under-predicted the width of the first velocity pulse. By reducing the bulk wave speed both were matched simultaneously. A bulk wave speed of 5000 m/s was used for experiment 56-11-38 and 4600 for experiment 56-11-34.

The three parameters for the Gurson flow surface given in Eq. (10) plus the initial value of porosity were evaluated here against the single plate impact experiment as listed above and were found to be $\phi_0 = 0.01$, $q_1 = 1.5$, $q_2 = 1.7$, and $q_3 = 2.25$. The resulting fit to the experimental data is given in Fig. 8 and the numerical damage and failure field given in Fig. 9. Note that the micrograph images for this experiment, one of which is given in Fig. 4, show that complete failure was achieved. As Fig. 8 demonstrates, the model does a poor job of matching the experimental Hugoniot elastic limit. We don't have an explanation for this at the present time but is certainly a required improvement to our representation of this material.

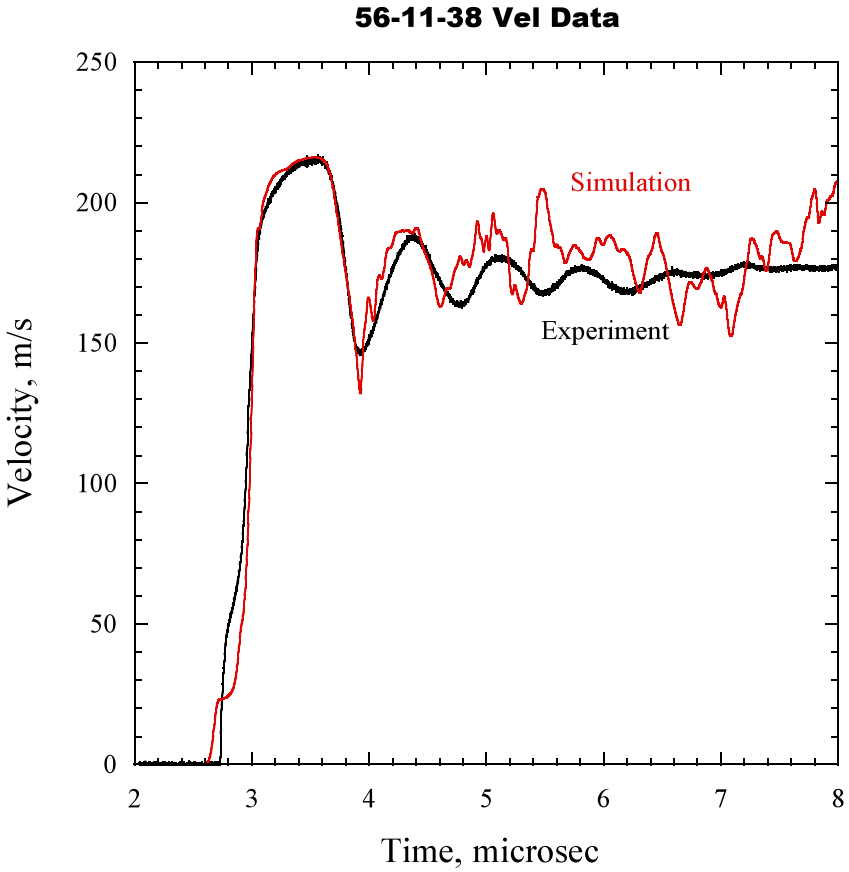

Fig. 8. Comparison between the experimental and simulated velocity profile for the DU plate impact experiment used to evaluate the material parameters $\phi_0 = 0.01$, $q_1 = 1.5$, $q_2 = 1.7$, and $q_3 = 2.25$.

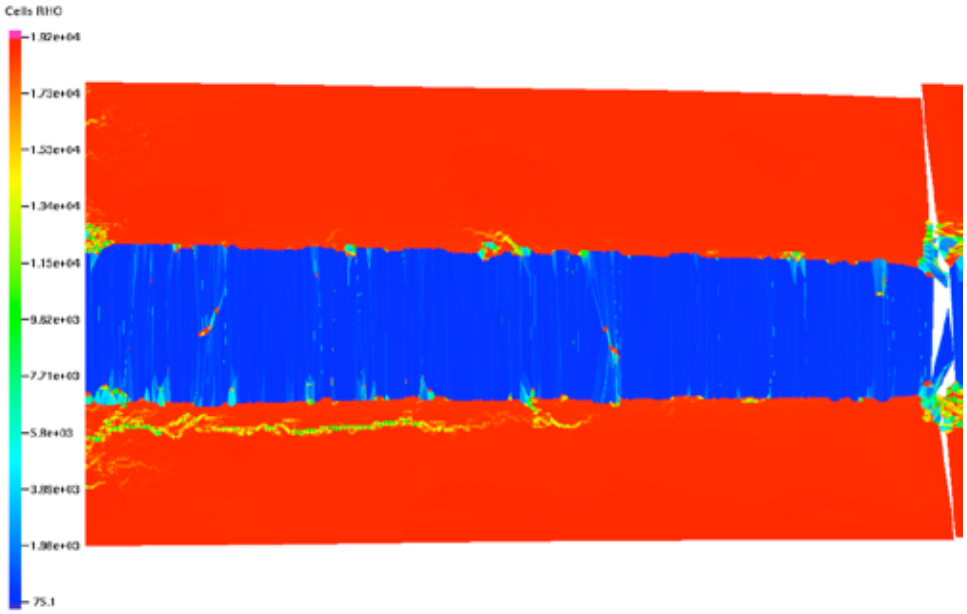

Fig. 9. Damage field predicted by the numerical simulation for the fitting process against the experimental results given in Fig. 4. Density is plotted here. The blue region indicates complete failure. The parameters used for this calculation were $\phi_0 = 0.01$, $q_1 = 1.5$, $q_2 = 1.7$, and $q_3 = 2.25$

This parameter set was used to perform a calculation of lower pressure experiment 56-11-34. The results produced a velocimetry trace that severely over-predicted the pull-back magnitude and did not produce porosity generation in the sample. This suggests that the model that presently does not represent damage nucleation physics does not adequately capture the lower pressure experiment. This is something that must be added and we will do so. It is also expected that the heterogeneous nature of the microstructure contributes to this nucleation behavior and must also be accounted for in some way if we are to satisfactorily predict the responses observed experimentally and demonstrated in Fig. 3 over a range of different loading conditions. The acceleration of mass due to the growth of voids is believed to also be a significant restraint to their growth for material densities of Cu or so and above. The density of depleted uranium is certainly higher than Cu and therefore a model for its damage behavior should account for it.

Conclusion

This document reports on preliminary work to evaluate the full damage model parameter set for annealed depleted uranium. There are some questions about the behavior of z-cut quartz and so the parameter set presented here should be considered as preliminary. This work suggests that a full anisotropic single crystal model should be used for quartz. The calculations suggest that a nucleation model is necessary to fully represent the low to high pressure regime of response. The metallography performed on the recovered annealed samples shows that even at high pressure, grain boundary failure is the predominant damage mechanism, not explicit porosity nucleation and growth. The physics of this

behavior must be accounted for and further work will consider grain boundary dominant damage and failure in the formulation and addition of nucleation to the presented model. Micro-inertial effects are also believed to be important and will be considered in the future. More work will be required to adequately represent depleted uranium and its general mechanical response to dynamic loading conditions.

References

Addessio, F. L., Johnson, J. N., 1993. Rate-dependent ductile failure model. J. Appl. Phys. 74, 1640-1648.

Cerreta, E. K., 2012. Unpublished data.

Chen, S. R., Gray III, G. T., 1996. Constitutive behavior of tantalum and tantalum-tungsten alloys. Met. Mat. Trans. A 27A, 2994-3006.

Dennis-Koller, D., 2009. Depleted uranium samples for J22T TPLA. Internal memo.

Dennis-Koller, D., 2011. Shock recovery of DU SPY007 (cold rolled vs. annealed). Internal memo.

Duvall, G. E., Fowles, G. R., Horie, Y., 1967. Equations of state in solids. Washington State University Report WSU SDL 67-01.

Follansbee, P. S., Kocks, U. F., 1988. A constitutive description of the deformation of copper based on the use of the mechanical threshold stress as an internal state variable. Acta metall. 36, 81-93.

Gray III, G. T., 2007. Quantification of the effect of HE driven shock prestraining on the strength and damage of depleted uranium. LA-CP-1094.

Gray III, G. T., Cady, C. M., McCabe, R. J., Hixson, R. S., Korzekwa, D. R., Lopez, M. F., 2006. Influence of energetic-driven "Taylor-wave" shock-wave prestraining on the structure/property response of depleted uranium. J. Phys. IV France 134, 909.

Gurson, A. L., 1977. Continuum theory of ductile rupture by void nucleation and growth: Part 1 – Yield criteria and flow rules for porous ductile media. J. Eng. Mat. Tech. 99, 2-15.

Hicks, D. G., Boehly, T. R., Celliers, P. M., Eggert, J. H., Vianello, E., Meyerhofer, D. D., Collins, G. W., 2005. Shock compression of quartz in the high-pressure fluid regime.

Jaglinski, T., LaLone, B. M., Bakeman, C. J., Gupta, Y. M., 2009. Shockless compression of z-cut quartz to 7 GPa. J. Appl. Phys. 105, 083528.

Johnson, J. N., 1968. Elastic precursor decay in quartzite for cylindrical and spherical flow. J. Appl. Phys. 39, 290.

Johnson, J. N., 1971. Shock propagation produced by planar impact in linearly elastic anisotropic media. J. Appl. Phys. 42, 5522.

Johnson, J. N., Gray III, G. T., Bourne, N. K., 1999. Effect of pulse duration and strain rate on incipient spall fracture in copper. J. Appl. Phys. 86, 4892.

Kocks, U. F., 1976, Laws for work-hardening and low-temperature creep. J. Eng. Mats. Tech. 98, 76-85.

Kocks, U. F., Argon, A. S., Ashby, M. F., 1975. Thermodynamics and kinetics of slip. Progress in materials science, Pergamon, Oxford.

Luo, S.-N., Mosenfelder, J. L., Asimow, P. D., Ahrens, T. J., 2002a. Direct shock wave loading of Stishovite to 235 GPa: Implications for perovskite stability relative to an oxide assemblage at lower mantle conditions. Geo. Res. Let. 29, 1691.

Luo, S.-N., Mosenfelder, J. L., Asimow, P. D., Ahrens, T. J., 2002b. Stishovite and its implications in geophysics: new results from shock-wave experiments and theoretical modeling. Phys.-Usp. 45, 435.

McSkimin, H. J., Andreath, P., Thurston, R. N., 1965. Elastic moduli of quartz versus hydrostatic pressure at 25^{o} and -195.8 ^{o}C. J. Appl. Phys. 36, 1624.

Marsh, S. P. (Ed.), 1980. LASL Shock Hugoniot Data, University of California Press, Berkeley.

Maudlin, P. J., Bingert, J. F., House, J. W., Chen, S. R., 1999a. On the modeling of the Taylor cylinder impact test for orthotropic textured materials: experiments and simulations. Int. J. Plasticity 15, 139-166.

Maudlin, P. J., Gray III, G. T., Cady, C. M., Kaschner, G. C., 1999b, High rate material modeling and validation using the Taylor cylinder impact test, Phil. Trans. R. Soc. Lond. A, 357, 1707-1729.

Maudlin, P. J., Mason, T. A., Zuo, Q. H., Addessio, F. L., 2003. TEPLA-a: Coupled anisotropic elastoplasticity and damage. The Joint DoD/DOE Munitions Technology Program progress report. Vol. 1. LA-UR-14015-PR.

Thurston, R. N., McSkimin, H. J., Andreatch, P., 1966. Third-order elastic coefficients of quartz. J. Appl. Phys. 37, 267.

Tvergaard, V., 1981, Influence of voids on shear band instabilities under plane strain conditions, Int. J. Fracture 17, 389-407.

Tvergaard, V., 1982, On localization in ductile materials containing spherical voids, Int. J. Fracture 18, 237-252.

Tvergaard, V., Needleman, A., 1984, Analysis of the cup-cone fracture in a round tensile bar, Acta Metall. 32, 157-169.

Varshni, Y. P., 1970. Temperature dependence of the elastic constants. Phys. Rev. B 2, 3952-3958.

Wackerle, J., 1962. Shock-wave compression of quartz. J. Appl. Phys. 33, 922.

Zhao, Y., Zhang, J., Brown, D. W., Korzekwa, D. R., Hixson, R. S., 2007. Equations of state and phase transformation of depleted uranium DU-238 by high pressure-temperature diffraction studies. Phys. Rev. B 75, 174104.

Section 11: Summary and Path Forward

Summary

The mechanical behavior of DU is shown to be a complex problem to accurately quantify due to the pronounced influence of purity, crystallographic texture, anisotropy, and the influence of shock prestraining on constitutive response. The mechanical behavior of DU for pedigreed SPY007 plate stock in both the annealed starting case and following 1-D shock prestraining has been quantified as a function of temperature and strain rate. The constitutive model fits with the MTS and PTW model for the DU plate studied were found to be excellent for the through-thickness and in-plane compression directions. The work hardening of this material is observed to be strongly dependent on strain rate and temperature. It was found to be even more significant for the material deformed in the in-plane direction where deformation twinning is the initially dominant deformation mechanism. For the applications of interest, the approach of characterizing the preshocked mechanical properties of DU and determination of a separate set of MTS or PTW model parameters with many variables unchanged is shown to be always more accurate and therefore it is encouraged that further shock prestraining experiments on DU be conducted, in particular, under additional peak shock 1-D Taylor-wave and HE-driven sweeping-wave loading.

The damage experiments, including tensile, sphere-extrusion, and spallation loading, illustrate several overarching conclusions that have pronounced ramifications for the development of predictive modeling of damage and failure in DU. The first is that while drive condition has a subtle affect on the continuum level response like spall strength (spall strength varies from 1.4 to 2.25GPa for a peak stress drive condition from 6.1 to 17.7 GPa), this spectrum of loading does affect the details of the damage evolution. In the plate impact experiments, the volume fraction of damage was highly sensitive to small changes in drive condition (no damage observed for a peak shock stress of 4.1GPa while obvious incipient damage is observed by 6.1GPa). Additionally, while the direct HE drive loading resulted in very similar failure characteristics, it seems to have undergone a very different adiabatic heating history. The second conclusion to be drawn is that the damage mechanisms in DU appears very insensitive to starting defect density; annealing versus testing this high purity material in the cold-worked state. This can be seen as both the as-annealed and the as-received (cold-worked) DU is observed to fail through a combination of void nucleation and coalescence at grain boundaries and adiabatic shear banding and display rather similar spall strengths. This suggests that the triaxiality of the stress state produced by the shock-loading condition may have more a more significant role in damage in failure than subtle microstructural changes in this material. The strong similarity in the intergranular damage and shear failure in the notched tensiles, sphere-extrusion samples, and spallation samples demonstrates the overall low level of plasticity with increased triaxiality. Future work should focus on characterization of the features of grain boundaries to understand why they promote failure and to understand if certain boundaries are more prone to failure than others.

The overall modeling of damage evolution and failure in DU demonstrates that a physically-based nucleation model is necessary to fully represent the low to high pressure regime of spallation response. The metallographic evidence on the recovered annealed samples displaying that even at high pressure, grain boundary failure is the predominant damage mechanism, not explicit porosity nucleation and growth. The physics of this damage evolution mode must be accounted for and future work must consider grain boundary dominant damage and failure in the formulation and addition of nucleation to the present damage DU modeling. Micro-inertial effects are also believed to be important in modeling the damage and failure in DU and need to be considered in the future. Additional experiments and modeling are required to adequately represent DU and overall constitutive response to quantify both dynamic loading and damage and failure loading paths.

2013-2015 Future DU Strategy for LANL's DU Program

Although LANL's need to model the response of Depleted Uranium(DU) remains clear, both the experimental and modeling communities have only very limited experience due to loss of staff and the focus on other materials for several years. This discussion of future plans in investigating DU behavior follows the goal of developing and validating predictive strength and damage models applicable to a broad range of loading conditions. Independent of drivers, the scientific understanding of this material is very much needed to support programmatic imperatives.

Shock-reshock experiments – Shock-deep release and then reshock experimental results are needed to quantify the constitutive behavior of DU during shock loading. Comparison of shock-reshock data with additional shock recovery experiments (detailed below) are needed to both validate shock recovery data and facilitate quantification of the Baushinger effect and its influence on post-shock constitutive response and damage evolution.

HE Spallation Experiments – Spallation testing of DU subjected to direct HE drive under both 1-D triangle-wave (plane-wave lens drive), and sweeping detonation wave loading are needed to quantify the effect of shockwave profile on spallation in DU and validate current DU damage models.

Sweeping-Detonation Wave Shock-Prestraining Experiments - Oblique HE driven shock wave experiments on DU to quantify the effect of shock obliquity on shock-induced hardening of DU as a function of several peak shock stresses. Thereafter, quantification of the post-shock mechanical and damage behavior will be used to validate the MTS and PTW constitutive models and TEPLA damage model:

- **a)** strength as a function of strain rate and temperature,
- **b)** shear response using "top-hat" and dynamic tensile extrusion on shock prestrained DU,
- **c)** damage behavior via tensile samples(smooth and notched)

Microstructure Surrogate Development – invest in a processing – structure – property investigation in the development of an HEU surrogate for use in constitutive and shock / damage studies as detailed above.

Microinertia --- New Physics Needed to Support TEPLA Modeling --- invest in parallel incipient spallation experiments on Aluminum and Tantalum to probe the effects of micro-inertia effects on damage nucleation and growth during spallation

ACKNOWLEDGMENTS

This document was prepared under the auspices of the U.S. Department of Energy by Los Alamos National Laboratory, operated by Los Alamos National Security, LLC, under Contract DE-AC52-06NA25396. Neither the United States Government nor any agency thereof, nor Los Alamos National Security, LLC, nor any of its employees, makes any warranty, express or implied, or assumes any legal liability or responsibility for the accuracy, completeness, or usefulness of any information, apparatus, product, or process disclosed, or represents that its use would not infringe privately owned rights.